DYNAMICS AND STATICS OF LIQUID-LIQUID AND GAS-LIQUID INTERFACES ON NON-UNIFORM SUBSTRATES AT THE MICRON AND SUB-MICRON SCALES

Michael M. Norton

A DISSERTATION

in

Mechanical Engineering and Applied Mechanics

Presented to the Faculties of the University of Pennsylvania

in

Partial Fulfillment of the Requirements for the

Degree of Doctor of Philosophy

2015

Supervisor of Dissertation

_____

Haim H. Bau

Professor, Mechanical Engineering and Applied Mechanics

Graduate Group Chairperson

_____

Prashant K. Purohit

Associate Professor, Mechanical Engineering and Applied Mechanics

Dissertation Committee

Haim H. Bau, Professor, Mechanical Engineering and Applied Mechanics

Howard H. Hu, Professor, Mechanical Engineering and Applied Mechanics

Kathleen J. Stebe, Professor, Chemical and Biomolecular Engineering

DYNAMICS AND STATICS OF LIQUID-LIQUID AND GAS-LIQUID INTERFACES ON NON-UNIFORM SUBSTRATES AT THE MICRON AND SUB-MICRON SCALES

Acknowledgements

To all my friends and family and those listed by name below, this accomplishment is yours as much as it is mine. First and foremost, I want to thank my parents Robert and Sharon Norton for their love and tremendous support throughout my studies.

I want to thank my advisor, Dr. Haim Bau, for offering his perspective and insights as I developed my ideas through the years and for creating the environment that made this work possible. Dr. Howard Hu, for generously offering his knowledge throughout my time as a student and for serving on my committee. Dr. Kathleen Stebe, for sharing her enthusiasm and passion for research with me, in addition to serving on my committee. I want to thank my academic parents, Dr. Risa Robinson and Dr. Steven Weinstein for their support and advice that surely brought me to where I am today. Special thanks to Dr. Frances Ross for welcoming me into the world of electron microscopy and creating a positive, nurturing environment in which to develop my ideas. Dr. Calvin Li, for offering an honest perspective on academia and for enthusiastic support of my research.

Thanks to the entire faculty and staff of the department of Mechanical Engineering and Applied Mechanics and throughout the School of Engineering and Applied Science. Special thanks to Maryeileen Griffith, Susan Waddington-Pilder, Olivia Brubaker, Peter Litt and Desirae Johnson in the MEAM office; Pete Szczesniak and Peter Rockett in the shop; and faculty Dr. Robert Carpick, Dr. Paulo Arratia and Dr. Michael Carchidi in particular for all of their help throughout the years.

I owe many thanks to my academic cohorts in the Bau-Hu lab and Dr. Daeyeon Lee's lab for their conversations, and willingness to share their resources and technical expertise. In particular, I'm gracious for my friendships with Steven Henry, Nicholas Schneider, and Joe Grogan. Their day-to-day conversation and support helped me grow intellectually and gain perspective on integrating academia, research, and life.

I feel deeply fortunate to have met many artists and craftspeople outside of academia during my time in Philadelphia. In particular, I want to thank Ann Klicka, Kimberly Shelton, Andy Upright, Leslie Grossman, Nathanial Ross, Matt Gilbert, Mike Rossi and Chris Winterstein for their friendship and for welcoming me to a whole new, inspiring world and offering their unique perspectives.

I am indebted to Laura Finch, Marta Mackiewicz, Eva Wô, and Katy Hardy. Through their dedicated friendship, love, and wisdom, I gained perspective on my studies and myself; I learned how to prioritize personal health in the face of daunting projects. I hope that I can love and champion them and others around me in the same way. Finally, I want to thank my lifelong friends Dan Boardman, Van Johnson, and Spencer Shultz for their loyalty and support all these years.

This work was supported, in part, by the National Science Foundation (NSF) NSEC DMR08-32802 through the University of Pennsylvania's Nano-Bio Interface Center (NBIC), and NSF CBET 1066573.

ABSTRACT

DYNAMICS AND STATICS OF LIQUID-LIQUID AND GAS-LIQUID INTERFACES ON NON-UNIFORM SUBSTRATES AT THE MICRON AND SUB-MICRON SCALES

Michael M. Norton

Haim H. Bau

Droplets and bubbles are ubiquitous motifs found in natural and industrial processes. In the absence of significant external forces, liquid-liquid and gas-liquid interfaces form constant mean curvature surfaces that locally minimize the free energy of a given system subject to constraints. However, even for sub-micron bubbles and droplets free of hydrodynamic and hydrostatic stresses (small Capillary, Weber, and Bond numbers), non-equilibrium at the contact line of sessile bubbles and droplets can influence geometries and dynamics. First, the wetting of micron-sized ellipsoidal particles was considered. In the space of axially symmetric interfaces, it is found that multiple constant mean curvature surfaces can satisfy volume and contact angle constraints. Partial encapsulation may be preferred even when the droplet's volume is sufficient to fully engulf the particle. The co-existence of multiple equilibrium states suggests possible hysteretic encapsulation behavior. Secondly, motivated by electron microscopy observations of sub-micron bubbles in a liquid cell, a small mobile and growing bubble confined between two weakly diverging plates is considered theoretically. Scaling analysis suggests that observed bubbles move by continuously wetting and de-wetting the substrates onto which they are adhered. 2D and 3D models are constructed incorporating the Blake-Haynes mechanism, which relates the dynamic contact angle to contact line velocity; partial pinning of the contact line is also

considered. In 2D, the system is fully described by a set of non-linear ordinary differential equations that can be readily solved. In 3D, the non-linear PDE system and constraints were solved using a pseudo-spectral method. Both 2D and 3D models predict that in order for a doubly confined bubble to grow in a super-saturated solution it must first increase its curvature; this is in contrast to a free-floating bubble whose curvature always decreases with the addition of mass/volume. Since the surface concentration is proportional to the internal pressure of the bubble, this geometric change temporarily regulates the growth of the bubble. The model predicts growth rates like those observed experimentally that are several orders of magnitude lower than predictions made by classical mass transfer driven growth theory developed by Epstein and Plesset.

Table of Contents

Acknowledgements iii

ABSTRACT v

Table of Contents vii

List of Tables ix

List of Figures x

Chapter 1. Background 1

Chapter 2. The Geometry of Droplets on Ellipsoids 4

2.1. Motivation 4
2.2. Materials and Methods 6
2.2.1. Fabrication of Elongated Polystyrene Particles 6
2.2.2. Encapsulation of Elongated Polystyrene Particles 8
2.3. Image Processing 10
2.4. Mathematical Model 12
2.5. Results and Discussion 15
2.6. Conclusion 26

Chapter 3. Liquid-Gas Interface Observations in SEM and TEM 28

3.1. Motivation 28
3.2. Experimental Methods 30
3.3. Initial Observations of Sub-Micron Bubbles in TEM 35
3.4. Bubble Transport Hypotheses 40
3.5. "Sliding" Sphere Model 46
3.6. Growth Anisotropy Revisited 50

Chapter 4. Bubble Growth in Hele-Shaw Devices 53

4.1. Motivation 53
4.2. Governing Equations and Scaling 57
4.3. Contact Line Dissipation 62
4.4. 2D Cylindrical Bubble Growing in a Wedge Model 63
4.4.1. Volume Driven Growth Results 69
4.4.2. Mass Transfer Driven Growth Results 72
4.5. Conclusion 79

Chapter 5. Quasi-3D Bubble in a Hele-Shaw 81

5.1. Motivation 81
5.2. Simplifying the Young-Laplace Equation 82
5.3. Contact Line Geometry 84
5.4. Bubble Center *X* Evolution 89
5.5. Volume 90
5.6. Surface Area 91

5.7. Spectral Representation 92
5.8. Initial Conditions 95
5.9. Model Results 96
5.9.1. Volume Controlled Case 96
5.9.2. Partially Pinned Bubble – Volume Controlled 104
5.9.3. Mass Transfer Driven Growth 107
5.10. Conclusions 112
Chapter 6. Growing Sessile Bubble with Contact Line Dissipation 114
6.1. Motivation 114
6.2. Insoluble 114
6.3. Compressible and Soluble 122
6.4. Conclusion 131
Chapter 7. Conclusions and Outlook 132
Chapter 8. Appendix 141
8.1. Drop Shape Calculation Using Numerical Energy Minimization 141
8.2. Contact Angle Measurement 147
8.3. Dimensionless Groups 147
8.4. How Ellipsoidal are the Particles? 149
References 151

List of Tables

Table 5.1: The magnitudes of the various properties used in the calculation of Table 5.3.The light mineral oil's manufacturer provides the kinematic viscosity at 40^{o}C while the specific gravity is given at 15.6^{o}C. Subscripts *CE* and *PS,* respectively, denote properties of the *C.elegans* and polystyrene 148
Table 5.2: Typical velocity and length scales. Subscripts D, CE, and PS denote properties belonging to a typical droplet, *C.elegans*, or polystyrene particle..... 149
Table 5.3: Estimated magnitudes of the non-dimensional parameters relevant to our system 149

List of Figures

Fig. 2.1: The ellipsoidal particles' formation process. (A) The creation of a polystyrene emulsion using a flow-focusing apparatus. (B) Evaporation of solvents from the emulsion in a warm water bath. (C) A micrograph of solidified mono-dispersed spheres. (D) Embedding PS particles in a PVA film. (E) Stretching of the heated PVA film to elongate the particles. (F) Dissolution of PVA film in water to release the ellipsoidal particles. (G) A micrograph of the ellipsoidal particles. 8

Fig. 2.2: A schematic (top) of the encapsulation process and (bottom) three typical encapsulation results. (A) a partially encapsulated particle, (B) a nearly fully engulfed particle in an ellipsoidal drop, and (C) a fully encapsulated particle in a spherical drop. 9

Fig. 2.3: (Left) A photograph of an elongated polystyrene particle (σ) partially encapsulated in a water drop (α) and suspended in a continuous phase (β) of oil. The interface is computed with the unduloid solution (dashed line) and energy minimization (hollow circles). The particle aspect ratio ε=8.0±0.9, the dimensionless volume V^*=0.027±0.007, and the contact angle $\theta = 10^\circ$. The ellipsoid's major (a) and minor (b) axes, the droplet's radius (r_2), and the axial position of the pinning line (z_1) are shown. (Right) The schematic details of the discretized domain used in the energy method. The radial position (ρ) originating from the spheroid's center, the inclination angle (ϕ), the arc length (l), and the node number (n) are shown. The discretization is used in the energy method. See supplement. 11

Fig. 2.4: The dimensionless maximum droplet radius $r_2^* / \varepsilon = r_2 / a$ (A) and the axial position of the contact line $z_1^* / \varepsilon = z_1 / a$ (B) as functions of the volume V^*. Experimental data points (circles) are color-coded according to their aspect ratio. Black indicates a stubby particle; the lighter the color, the more slender the particle. The theoretical predictions are depicted for two aspect ratios, ε=2.5 (gray line) and 7.5 (black line), and two contact angles, $\theta = 10^\circ$ (solid line) and $\theta = 20^\circ$ (dashed line). 17

Fig. 2.5: Contours of constant contact angle θ and constant volume V^* are depicted in the space of the unduloid coefficients (χr_1^*) and r_2^*; $\varepsilon = 3$. Regions I (white background) and II (gray background) correspond, respectively, to drop volumes $V^* < 1$ and $V^* > 1$. The hollow (red) circle denotes the smallest fully engulfing, spherical drop with $V^* = 1$. The solid dots indicate the maximum possible unduloidal drop volume at a given contact angle. 19

Fig. 2.6: The shapes of the two solution branches ($V^* = 1.20$, solid lines) and that of the limiting drop ($V^* = 1.34$, red line). $\theta = 60^\circ$ and $\varepsilon = 3$ 22

Fig. 2.7: The free energy relative to that of the expelled state as a function of normalized volume. The solid and dashed lines correspond, respectively, to pinned drops and engulfing drops. The shaded region corresponds to the parameter space where multiple equilibrium states coexist. The particle aspect ratio ε=3. 23

Fig. 2.8: A magnified image of the framed region in Fig. 7. ΔE^*(A) and z_1^* (B) are depicted as functions of V^*. $\theta = 60^\circ$ and $\varepsilon = 3$. The arrows describe a gedanken experiment..... 25
Fig. 2.9: Normalized curvature (A) and axial force (B) as functions of dimensionless volume; $\varepsilon = 3$. Hollow circle denotes a spherical, engulfing drop. 26
F 32
Fig. 3.2: (Left) Total cell thickness and (Right) slope as a function of dimensionless position where *a* is the half-width of the membrane $a = 50\mu m$ (the origin is at the center of the membrane) for $P/P_{atm} = 10^{-2}, 10^{-1}, 10^{0}$ and 10 33
Fig. 3.3: Intensity profiles from two STEM images (inset) before (bottom) and after (top) bubble creation converted to water thickness (asterisks and circles correspond, resptively, to before and after bubble creation) compared to the Maier-Schneider theory[79]. Estimated pressures were respectively ~1/7 and ~1/2 of an atmosphere. 33
Fig. 3.4: (Left) Light microscope images of the silicon nitride membrane at various stages of liquid cell filling and (Right) a schematic of the cross-section along the dashed line (not to scale, deformations are exageratted for clarity). Color variations are due to height variatons that result in constructive and destructive interference of different wavelengths. (A) Unfilled liquid cell. (B-C) Capillary action pulling the windows together, and trapping an air bubble. (D-F) After adding liquid to the ports, the membranes spontaneoulsly relax, note that the bubble's projected area increases. 35
Fig. 3.5: Composite image created from several TEM images observed at a magnification of 5,000X. All images are unaltered to illustrate the difference between vignetting and larger scale transmission gradients. Each still is $1.8[\mu m]$ across..... 38
Fig. 3.6: (Right) TEM image of an empty liquid cell and (Left) the same image with enhanced contrast, illustrating vignetting. 38
Fig. 3.7 : Trajectories of bubbles observed at three different nanoaquarium locations. (A – top) and (B - middle) are observations made at 5,000x, (C - bottom) is at 10,000x. 39
Fig. 3.8: A typical bubble and its intensity profile taken along the principal axes and the direction of motion. Markings on intensity profile illustrate the drop in background intensity that occurs across the length of the bubble. 43
Fig. 3.9: (A) Fraction of bubbles as a function of aspect ratio for bubbles observed at 5000x from 5 different nanoaquarium locations. (B) Angle between background intensity gradient $\propto \nabla h$ and velocity (light gray) and angle between bubble's principal axis $\mathbf{p}$ and velocity $\dot{\mathbf{x}}$ (dark gray). The inset shows a schematic of a bubble whose position, radius, and aspect ratio evolve in time with the vectors for velocity, background gradient, and principal axis labeled..... 44
Fig. 3.10: Three characteristic bubbles at different stages in growth: A) a sessile bubble touching one surface, B) bubble beginning to bridge between membranes and C) a bubble touching both membranes and growing anisotropically due to confinement gradient. The columns are, respectively, from left to right: schematics of the side

view, bright field TEM images, and intensity profiles taken along the principal axis. 46
Fig. 3.11: Translational velocity $\dot{x}$ as a function of growth rate of the hydraulic radius $\dot{R}$ for bubbles observed at 10,000x (gray "+") and 5,000x (gray dots) magnifications. A bubble at each magnification is hilighted (connected points) along with its moving average trajectory in $\{\dot{R},\dot{x}\}$ space. Solid and dashed lines are, respectively, eqn. [3.3] (Fig. 3.10.C) and eqn. [3.4] (Fig. 3.10.A). $\theta_0 = 45^\circ$. $\varphi = 10^{-1}, 10^{-1.25}, 10^{-1.5} \cdots$. 49
Fig. 3.12: Contact-line and centroid evolution of a bubble that nucleated in the field view. At early times the bubble grows while the position of the rear portion of the contact line changes very little; the last several frames show a sudden change in behavior. To show the passage of time, early profiles are plotted with more transparency. $\Delta t = 1/15$ s. 52
Fig. 3.13: Measured translational velocity (symbols) as a function of (A) bubble's hydraulic radius and (B) as a function of aspect ratio. N=23. Data symbol's size is proportional to the hydraulic radius. The solid lines in (A) correspond to $\dot{x} \sim R_H$ and $\dot{x} \sim 10R_H$. Solid arrow in (B) indicates the passage of time. 52
Fig. 4.1: Schematic of 2D bubble slug showing contact line positions $x_\pm$, contact angles $\theta_\pm$, local channel half-height $h_\pm$, radius of curvature *R*, half-length *L*, and center position *X* with exaggerated taper φ. 64
Fig. 4.2: θ_- (red) and θ_+ (black) contact angle evolution (A) when the wedge angle $\varphi = \{0.1, 0.3, 0.5, 0.7\}$ ($V_0^* = 0.004$ and $\theta_0 = 45^\circ$) and (B) when the area flux $V_0^* = \{0.001, 0.002, 0.01, 0.02\}$ ($\varphi = 0.25$ and $\theta_0 = 45^\circ$). 71
Fig. 4.3: Bubble radius of curvature normalized by starting radius as a function of time. $V_0^* = \{0.001, 0.002, 0.01, 0.02\}$. $\varphi = 0.25$ and $\theta_0 = 45^\circ$. 72
Fig. 4.4: Bubble half-length and radius (A), velocity (B), and ratio *R/L* (C) as functions of time. The blue "+" and red dots represent experimental data from, respectively, 10,000x and 5,000x observations. We plot four combinations of η_{CL} and φ: $\eta_{CL} = \eta_0\{10^1, 10^3\}$ are respectively, triangles and circles; and $\varphi = 10^{-6}, 10^{-6.25}$ are respectively solid and hollow symbols. Dashed lines correspond to $\eta_{CL,-} \to \infty$. Solid and dashed lines are Epstein-Plesset theory using eqn. [3.3] for the velocity with $\varphi = 10^{-6}$ and $10^{-6.25}$ (note that the growth rates are nearly identical while the velocities differ). In (B), black trends are the half-length *L* and gray trends are t he corresponding radius of curvature *R*. $\eta_0 = 8.9 \times 10^{-4}$ Pa s, $h_0 = 15$ nm, $\alpha = -4$, $\theta_0 = 30^\circ$, and $\gamma = 40$ mN/m 74

Fig. 4.5: R/R_0-1 (A) and $\theta_\pm-\theta_0$ ($\pm$ are, respectively, black and red) (B) as functions of time. $\alpha=\{-2,-3,-4\}$. $\eta_{CL}=\eta_0 10^3$ and $\varphi=10^{-6}$. All other parameters are the same as in Fig. 4.4..... 76
Fig. 4.6: Bubble half-length and radius of curvature (A), velocity (B), and ratio *R/L* (C) as functions of time. Blake-Haynes model $\eta_{CL}=\eta_0 10^3$ (dashed), pinned rear contact line $\eta_{CL,-}\to\infty$ (dotted), and hysteresis with $\beta_A=\{1.10,1.15,1.20\}$ and $\beta_R=1$ (black, from left to right) results. For all trends, $\alpha=-4$ $\varphi=10^{-6}$ 78
Fig. 5.1: Problem schematic, top view. Solid curve is the contact line, dashed curve is the bubble geometry at the mid-plane of the wedge. 85
Fig. 5.2: Coefficient evolution (*n*=1,2…*N*) normalized by the 0th order mode for three different truncations (*N*=3,4,5). In the long time limit, the contact line assumes a perfectly circular geometry regardless of where the series was truncated. Different line styles correspond to the three different *N* used (see key); coefficents (*n*) are labeled. 98
Fig. 5.3: Relative Error R, X and ρ_0 (1st, 2nd, and 3rd rows, respectively) for N=0,1,2,3,4 compared to N=5 ($\text{Error}=\left|\left(f_N-f_5\right)/f_5\right|$). Left column shows temporal evolution of the error and in the right column, gray scale indicate time (from light to dark, $t=10^{-1},10^1,10^3,10^5$). 99
Fig. 5.4: (Left Column) Temporal evolution of bubble center X, average contact line radius ρ_0, and radius of curvature R and (Right Column) their time derivatives for $V_0=\{1\times10^{-3},5\times10^{-3},1\times10^{-2}\}$; values correspond to curves from bottom to top in all plots. 101
Fig. 5.5: Temporal evolution of the ratio between the radius of curvature R and the 0th mode ρ_0 that governs the average radius of the droplet. The droplet begins as a sphere (the initial ratio being dictated by the contact angle and wedge angle eqn. [5.37]) but becomes more "squashed" as time goes on. Under volume controlled cases $V^*\propto V_0^* t^3$, a geometric steady state of self-similar growth is reached. From top to bottom $V_0^*=\{1\times10^{-3},5\times10^{-3},1\times10^{-2}\}$. As noted when describing the initial conditions, the model is initiated as a sphere in order to satisfy an initially uniform contact angle, even though the assumption $R/\rho_0=\varepsilon\ll1$ is initially violated. 101
Fig. 5.6: Contact angle evolution for $V_0^*=\{10^{-3},5\times10^{-3},10^{-2}\}$; amplitude in contact angle variation increases with V_0^* . N=3. 102
Fig. 5.7 : Comparison between N=3 system and asymptotic values found from $\Phi=0.15,U_0=1,\theta_0=\pi/4,V_0=10^{-3}$ 103
Fig. 5.8: (Top Row) Contact line evolution of a partially pinned bubble for $V_0^*=10^{-4}$, $t=0,15,30\cdots90$ for two different slopes $\Phi=0.01$ and 0.1; (Bottom Row) the same

contact line normalized by the average radius ρ_0 and centered around X, note that a larger time range is used ($t = 0,100,200\cdots500$) for the $\Phi = 0.01$ case to illustrate that the same elongated geometry of $\Phi = 0.1$ is approached. $\theta_0 = 45^\circ$ 107

Fig. 5.9: Comparison between 2D model (dotted line) presented in Chapter 4 and 3D model (solid line) of (A) Bubble size (half length L for 2D model or ρ_0 for 3D model), (B) velocity, and (C) radius of curvature *R* for a few different wedge angles, $\Phi = \left\{10^{-4}, 10^{-5}, 10^{-7}\right\}$. Growth is driven by mass transfer. $\eta = \eta_0 10^3, \alpha = -3, h_0 = 15[nm]$ 109

Fig. 5.10: Contact line evolution comparison between experiment (data points) and mass transfer driven model (lines) with partial contact line pinning (A) and without it (B), darker lines and points correspond to later times. Values that provided the best fit to the experimental data are $\Phi = 10^{-6.3}, \eta = \eta_0 10^2, \alpha = -2.73, h_0 = 15[nm]$, time between frames $\Delta t = 0.2[s]$ 110

Fig. 5.11: Comparison between 2D model with (gray, dotted line) and without (black, dotted line) a pinned rear contact line, 3D model with and without contact line pinning (respectively, gray and black solid lines), and the experimental data of 7 bubbles that nucleated at the same location. (A) Bubble size (half length L for 2D model or ρ_0 for 3D model), (B) velocity, and (C) radius of curvature *R* for mass transfer driven growth $\Phi = 10^{-6.3}, \eta = \eta_0 10^2, \alpha = -2.73, h_0 = 15[nm]$, these are the same values that provided the best fit in Fig. 5.10. An open, gray circle marks the end of the predictions made by the pinned, 3D model. 111

Fig. 6.1: Schematic of a spherical sessile bubble (white) of radius R with a contact angle θ (as measured from the liquid side, gray). 116

Fig. 6.2: (A) radius of curvature, (B) contact angle and (C) contact line radius of an incompressible droplet growing according to $V^* = V_0^* t^{*3}$, $V_0^* = \left\{10^{-2}, 10^{-1}, 1, 10, 10^2, 10^3\right\}$. At $t \gg 1$, $R \propto t$ (dotted line) and $\dot{\theta} \to 0$ (larger growth rates are associated with steady state values *further* from equilbrium). $\theta_0 = 45^\circ$ 117

Fig. 6.3: (A) radius of curvature, (B) contact angle and (C) contact line radius of an incompressible droplet initiated at a non-equilibrium contact angle and relaxing toward its equilbrium state while conserving volume, $V_0^* = 0$. All droplets are given the same initial volume such that the final radius of curvature of the equiliberated droplet $R^* = 1$. $\theta_0 = 45^\circ$ 120

Fig. 6.4: (A) Contact angle evolution of a droplet beginning at a non-equilibrium contact angle while conserving volume $V_0^* = 0$. Trends compare full model (black line) and linearized model (eqn. [6.7]) (gray dashed line) for $\theta_i = \left\{30^\circ, 60^\circ\right\}$ with $\theta_0 = 45^\circ$.

(B) Relaxation time constant λ_1 (eqn. [6.8]) as a function of initial contact angle for $\theta_0 = \{45^\circ, 90^\circ, 135^\circ\}$ 121

Fig. 6.5: A sample of the mesh (with $\theta_0 = 45^\circ$) used for the finite element calculation of the total mass flux into the bubble plotted in Fig. 6.6. The bubble has unit radius, the actual domain size used was 50 times the size of the bubble. 123

Fig. 6.6: Comparison of the (dimensionless) mass flow into a sessile bubble as a function of contact angle between a spherically symmetric solute field (black line) and a more realistic calculated using the finite element method (black points). Note that when the bubble is a perfect hemisphere ($\theta = 90^\circ$) the two methods agree due to symmetry..... 124

Fig. 6.7: (A) radius of curvature, (B) contact angle and (C) contact line radius of a shrinking bubble $\Omega_2 = \{10^{-4}, 10^{-3}, 10^{-2}, 10^{-1}, 1, 10\}$. $\alpha = 1.1$, $P_\infty^* = 0.01$ and $\Omega_1 = 0.019$ 126

Fig. 6.8: (A) radius of curvature, (B) contact angle and (C) contact line radius of a bubble whose surface concentration matches the concentration in the solute initially $\alpha = 1$, but begins with a non-equilibrium contact angle, $\theta(0) = \{1^\circ, 15^\circ, 30^\circ\}$. The bubbles grow; however, the contact angle evolution is non-monotonic., $\theta_0 = 45^\circ$, $P_\infty = 0.01$, $\Omega_1 = 0.019$ and $\Omega_2 = 10^{-3}$. 127

Fig. 6.9: (A) radius of curvature, (B) contact angle and (C) contact line radius of a shrinking bubble $\alpha = \{0.999, 0.99, 0.9\}$. Solid, dotted, and dashed lines are, respectively $\Omega_2 \to 0$, $\Omega_2 = 10^{-5}$ and $\Omega_2 = 10^{-4}$. $P_\infty^* = 0.01$ and $\Omega_1 = 0.019$. 128

Fig. 6.10: (A) radius of curvature, (B) contact angle comparison between theory mass transfer driven theory and the experimental work of Li *et al.*[106] $\Omega_2 = \{1, 10^{-1}, 10^{-2}, 10^{-3}, 0\}$, $\theta_0 = 160^\circ$ 130

Fig. 7.1: An SEM micrograph of a large bubble oscillating in the nanoaquarium liquid cell. The bubble is oscillating at approximatley 100 Hz. Because of the slow scan speed of the microscope, the bubble oscillates several times while the image is captured. 138

Fig. 7.2: A series of SEM images depicting how temporarily increases the magnification on an ostensibly dry region of the nanoaquarium can promote local film thickening. The liquid does not build up uniformly and undergoes some form of instability with a characteristic wavelength. 140

Fig. 8.1 (A) The shape of a drop wetting a cylindrical fiber as obtained with the unduloid method (solid line) and the energy minimization method (hollow circles, N=100, not all nodes are plotted). $\theta = 45^\circ$. (B) The relative discrepancy between the energy minimization and the unduloid predictions of the droplet apex (squares) and the axial position of the pinning point (circles) as a function of the number of nodes (N) used in the discretization of the drop surface; for large *N,* the error decreases as N^{-1} 145

Fig. 8.2: The axial position of the pinning line (A) and the drop radius $r_2^* / \varepsilon = r_2 / a$ (B) as functions of the dimensionless volume V^*. The solid lines and the symbols denote, respectively, the unduloid solution and the energy minimization solution. ε=5 and $\theta = 90^\circ$. 146
Fig. 8.3: The penalty function [8.1] as a function of the pinning line position ϕ_1 for various contact angles. e=3. The energy minima, when present, are denoted with solid circles. 146

Chapter 1. Background

Droplets and bubbles are ubiquitous motifs found in natural and industrial processes; as such, interest spans multiple fields within engineering, physics, and mathematics. At the micro- and nano- scale multi-phase systems are of interest to developers of droplet-based high-throughput lab-on-chip devices and meta-materials built up from emulsions and colloids[1]-[3]. In these applications, the immiscibility of two phases is utilized to either transport a disperse phase (typically water) of a well-controlled size containing reactants or specimens of interest within a carrier fluid (typically mineral or silicon oil), or to provide an interface for colloidal assembly.

In all these cases, the geometry of the solid, the volume of the disperse phase, and the contact angle determine the shape of the liquid-liquid interface or gas-liquid interface and ultimately the behavior of the system. Clever conduit design in drop-based devices can induce the merging of bubbles and droplets, or incite instabilities forcing them to dispense from a fluid stream or divide. Colloids can be made to jam on a confined interface and create non-spherical, stabilized emulsions[4], or the curvature of the interface can be controlled to direct assembly of particles in specific ways [5], [6].

In microfluidic applications, a substrate/continuous phase combination is often sought such that the latter completely wets the former. Additionally, the transport of disperse phases is often rapid enough that a dynamic film of the continuous phase always exists between the disperse phase and the substrate [7], [8]. However, when this is not the case, the disperse phase makes direct contact with the substrate and (de)wetting dynamics

at the contact line can critically alter the behavior of the system[9]-[12]. Contact line physics also impact colloidal adsorption to interfaces [13] and are important for deposition of Langmuir-Blodgett films [14].

In this thesis, interface geometry, interface-substrate interactions, and contact line dynamics will be explored in two different systems where capillary forces dominate over viscous, inertial, and body forces. In Chapter 2, the geometry of sub-millimeter droplets of water adhered to ellipsoidal polystyrene particles of comparable size will be examined. It will be shown that when a substrate is finite and curved, that multiple interface geometries can exist for a given volume of the disperse phase. However, it is found that because these configurations are geometrically disparate, the system can exhibit conformational hysteresis. Theory shows that if one begins with a small droplet bound to the particle and increases its volume the system will evolve through one set of geometries while if one begins with a droplet that fully engulfs the ellipsoid and shrinks it, a different set of geometries will be accessed. Chapter 3 focuses on novel electron microscopy observations of growing and moving sub-micron bubbles created by electron-beam-induced radiolysis [15], [16] and confined within a Hele-Shaw-like apparatus comprised of a micro-fabricated pressure vessel designed to enable imaging with electrons [17]. Chapter 4 will illustrate how classical theories describing bubble growth[18]-[21] are not applicable under the conditions encountered in Chapter 3 and need to be modified to explicitly account for the interplay between contact line dynamics [9]-[12], confinement, and mass transfer. It will be demonstrated by developing a 2D model based on the Blake-Haynes model for contact line movement [12] that the restricted movement of the contact line (be it partial or full) encumbers the rate of mass flux into the bubble by requiring that

curvature increase with volume at short time scales. Chapter 5 will expand on the intuition gained from the 2D model to develop a 3D model valid for highly confined high aspect ratio bubbles (bubbles whose height is much less than their projected radius). The model is able to predict the contact line shapes observed experimentally and confirms the important role of pinning at early times. Chapter 6 examines a theoretically simpler but still important scenario of a bubble on a single substrate growing and shrinking due to diffusion with the same contact line resistance model used in the previous chapters. Model predictions show that, unlike the doubly-confined cases considered in Chapters 4 and 5, growth is relatively unaffected. However, for a dissolving bubble, it is shown that as contact line resistance is increased, dissolution can be inhibited and the bubble temporarily stabilized; the model can be thought of as a generalization to the completely pinned nanobubbles modeled by Lohse and Zhang [22]. This work closes in Chapter 7 with suggestions for further theoretical work on bubbles that move by contact line wetting and de-wetting and hi-lights two ostensibly beam-induced interfacial fluid dynamical phenomena relevant to liquid cell electron microscopy: interface oscillations and spontaneous film thickening.

Chapter 2. The Geometry of Droplets on Ellipsoids

2.1. Motivation

Rapid and controllable encapsulation of colloidal objects in aqueous drops is useful for high throughput studies of bacteria [23], [24], cells [25], embryos [26], [27], and larger multi-cellular organisms such as nematodes [28]. High throughput devices confer the opportunity to efficiently explore the effects of genetic and environmental factors on phenotype. The same encapsulation method can also be used to form anisotropic colloidal materials with customized properties. This work is motivated by our work on encapsulating *Caenorhabditis elegans (C. elegans)* in water drops dispersed in oil, using a flow-focusing platform similar to the one described in Utada et al. [29].

It was observed that, under certain conditions, the animals were partially encapsulated and under others, fully encapsulated. *C. elegans* are compliant and deform under the action of surface tension forces. To gain insights into the encapsulation process, it is desirable to examine separately the effect of particle's size and elasticity. Hence, it was advantageous to study a simpler system of rigid particles. To estimate the importance of elasticity in the particle-droplet system, we compare the capillary force resulting from the pinned contact line to the critical load required for Euler-buckling [30]. The ratio of these two forces is given by the dimensionless group $\Gamma = \left(8\gamma a^2 \cos\theta\right) / \left(\pi^2 E b^3\right)$, where E, γ, a, b, and θ are, respectively, the elastic modulus, surface tension, minor particle radius, major particle radius (if ellipsoidal), and contact angle at the contact line. In this

study, we focus on polystyrene particles with $\Gamma \sim O(10^{-7})$. In contrast, $\Gamma \sim O(10^{6})$ for live *C. elegans*. By focusing on rigid particles, we are able to examine geometric effects in the absence of elastic ones.

In the absence of gravitational forces, the oil-water interfaces belong to a special class of axisymmetric, constant curvature solutions of the Young-Laplace equation known as unduloids or Delaunay surfaces [31]. Princen[32], Roe [33] and Carroll[34] were the first to apply the unduloidal solutions of the Young-Laplace equation to the cylindrical fiber-wetting problem. The pinning of droplets and bubbles on patterned substrates have attracted ongoing interest from both experimentalists and theorists [35]-[40]. In particular, Hanumanthu and Stebe determined the equilibrium positions and stability of droplets pierced by a cone[41] and Michielsen[42] experimentally confirmed that droplet equilibrium positions coincided with the free-energy minima. None of the above studies has considered finite length particles that can be either partially or fully encapsulated by the drop.

In this chapter, the shape of axisymmetric drops encapsulating ellipsoidal particles as a function of drop volume, contact angle, and particle dimensions is determined. I discuss experimental results and extend Carroll's classical fiber wetting problem to address finite length particles with non-uniform cross-sections. The droplet shapes are determined by searching for unduloids that satisfy specified boundary conditions at the contact lines. The same droplet shapes are also obtained with an energy minimization method. When the droplet's volume is smaller than a critical value, only one axisymmetric, pinned state is possible. Once the droplet has exceeded a critical volume, three axisymmetric droplet configurations that correspond to energy minima co-

exist: a spherical engulfed state and two pinned, unduloidal states. For one pinned solution branch, the distance of the contact line from the particle's center increases as the droplet volume increases. For the other pinned solution branch, counter to intuition, the opposite is true; the axial pinning position *retracts* upon droplet volume increase. While not energetically favorable, this second barrel configuration possesses a lower mean curvature and lower internal pressure than the first. As the droplet volume is increased, the two solution branches eventually coalesce at a limit point that signifies the end of the existence of axially symmetric pinned solutions. Further volume increases result in either the breaking of axial symmetry (which we do not consider in this work) or a fully engulfed state. We gain further insights into the problem by calculating the system's free energy as a function of state, which reveals the existence of hysteretic behavior.

2.2. Materials and Methods

2.2.1. Fabrication of Elongated Polystyrene Particles

Polystyrene spheres were formed (Fig. 2.1) with a flow-focusing device constructed from glass capillaries in the same manner as Utada et al. [29]. A solution of polystyrene (Scientific Polymer Products, Inc., Mw 190,000, CAS: 9003-53-6, CAT: 845) 15% w/w dissolved in a solvent, comprised of chloroform 75% v/v (Fisher Science, CAT: C606) and toluene 25% v/v (Fisher Science, CAT: T290), was flowed into the device at a flow rate of $Q_{inner} = 300 \mu l / hr$ to form the dispersed phase (Fig. 2.1.A). The outer phase consisted of water with 2% w/w Poly(vinyl alcohol) (PVA) 87-89% hydrolyzed Mw

13000-23000 (Sigma Aldrich, CAT: 363170) that helped stabilize the polystyrene emulsion and was pumped in at a rate $Q_{outer} = 10{,}00 \mu l / hr$. The emulsion was discharged into a 40°C water bath. The solvents evaporated, and the drops solidified to form $\sim 100 \mu m$ diameter spheres (Fig. 2.1.C).

To form elongated particles, we followed a process previously described in [43]-[48]. Briefly, the particles were embedded in a liquid film of PVA (87-89% hydrolyzed Mw 85,000-124,000, Sigma Aldrich CAT 363081) dissolved in water. Evaporation of the water yielded a solid, free-standing film of PVA (Fig. 2.1.D) embedded with the PS particles. The film was subsequently clamped into a pulling apparatus, heated to above the glass transition temperature of polystyrene (~100°C), using a handheld heat gun, and pulled (Fig. 2.1.E). The applied tension caused the particles to elongate and assume nearly ellipsoidal shapes. While under tension, the film and particles were cooled to room temperature, rendering the particles' deformations permanent. The PVA film was then dissolved in water to release the now ellipsoidal particles. The particles were washed multiple times by exchanging the water suspending them to remove excess PVA. The so-formed ellipsoidal particles varied significantly in their sizes, which required us to individually measure the dimensions of the particles with which we experimented. Fig. 2.1.G is a micrograph of the precipitated ellipsoid particles, whose minor diameter varied from 50 to 100 μ*m* and whose length varied from 400 to 700 μ*m*.

Although polystyrene particles are natively hydrophobic, the PVA, which we used to stabilize the emulsion during the particles' formation and to form the film for the particles' stretching, adsorbed to the ellipsoidal particles' surface, rendering them hydrophilic with a three phase contact angle of 14.2±5.2°. The surface tension, contact

angle, and droplet morphology also depend strongly on the surfactant concentration. The contact angle measurement is described in supplemental information.

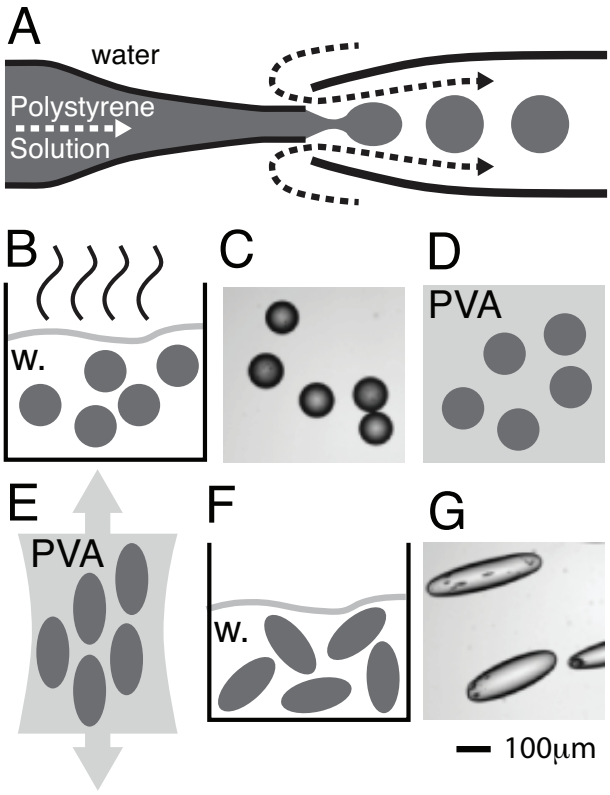

Fig. 2.1: The ellipsoidal particles' formation process. (A) The creation of a polystyrene emulsion using a flow-focusing apparatus. (B) Evaporation of solvents from the emulsion in a warm water bath. (C) A micrograph of solidified mono-dispersed spheres. (D) Embedding PS particles in a PVA film. (E) Stretching of the heated PVA film to elongate the particles. (F) Dissolution of PVA film in water to release the ellipsoidal particles. (G) A micrograph of the ellipsoidal particles.

2.2.2. Encapsulation of Elongated Polystyrene Particles

The encapsulation of the polystyrene ellipsoids took place in a flow-focusing device similar to the one used to create the polystyrene spheres. Fig. 2.2 (top) depicts a

schematic of the encapsulation process. Polystyrene ellipsoids were first imbibed into a length of vinyl tubing from a dish containing rinsed particles. The tube was subsequently connected to a syringe pump at one end and to the flow-focusing device at its other end. The suspension was then discharged through the device. The jet (central stream) laden with the particles was sheathed with a co-stream of immiscible oil. Observations were carried out using an inverted optical microscope (Nikon Diaphot 300) at 4× magnification; encapsulation events were captured at 10,000-15,000 frames per second with a high-speed SR-CMOS camera (Phantom V7.1). Fig. 2.2 (bottom) shows three typical encapsulation results: (A) a partially encapsulated particle, (B) a nearly fully engulfed particle in an ellipsoidal drop, and (C) a fully encapsulated particle in a spherical drop.

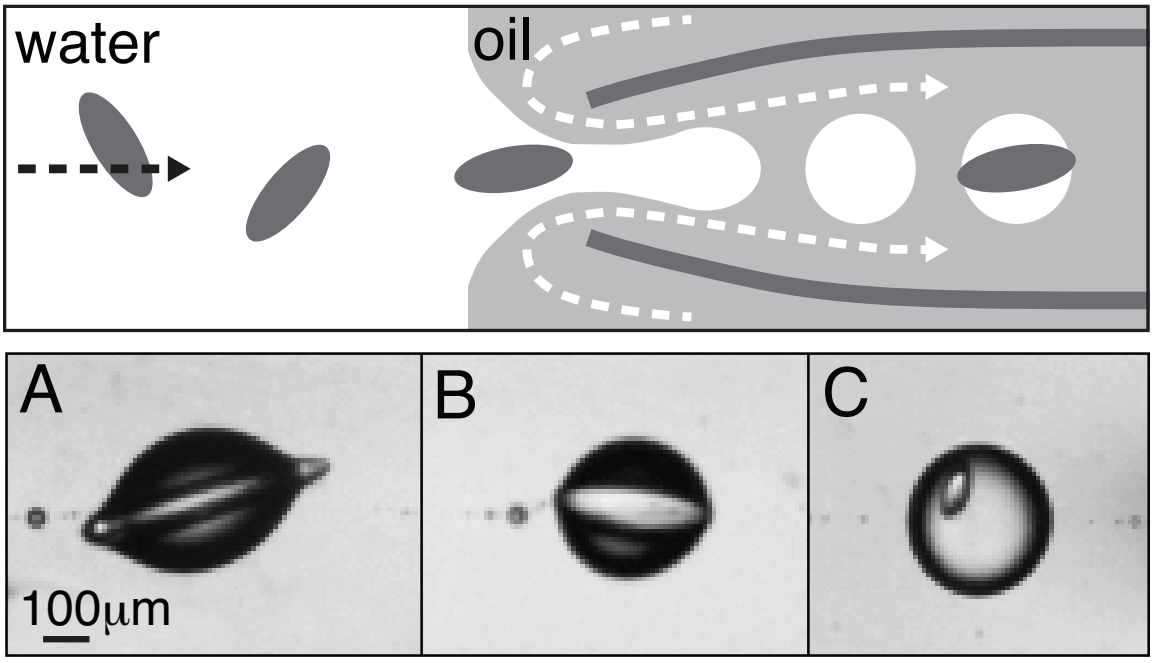

Fig. 2.2: A schematic (top) of the encapsulation process and (bottom) three typical encapsulation results. (A) a partially encapsulated particle, (B) a nearly fully engulfed particle in an ellipsoidal drop, and (C) a fully encapsulated particle in a spherical drop.

2.3. Image Processing

The encapsulated particles were imaged while in the flow focusing device (Fig. 2.2). The images of the encapsulated particles were processed with ImageJ and Matlab to deduce the droplet volume, the position of the pinning line, the maximum radius of the droplet, and the particle dimensions.

In ImageJ, the oil-water interfaces were traced using the multi-point tool as schematically depicted on the right hand side of Fig. 2.3. The top and bottom profiles of each projection of an encapsulated particle were traced out in five consecutive frames and the center, inclination, major axis (a), and minor axis (b) were determined. We found that the particles can be approximated reasonably well as prolate ellipsoids with the averages of a and b serving, respectively, as the major and minor axes. See the Appendix for a discussion of the accuracy of this approximation. The ellipsoid's aspect ratio $\varepsilon = a/b > 1$. The volume of the drop V was estimated using trapezoidal integration of the discretized droplet surface.

We present our experimental data and theoretical predictions with dimensionless quantities. The minor radius b is the length scale. The droplet's dimensionless equatorial radius and contact line position are, respectively, $r_2^* = r_2/b$ and $z_1^* = z_1/b$. The volume of the drop (V) is normalized with the volume V_0 of the smallest spherical drop that encapsulates the particle. In other words, $V_0 = \frac{4}{3}\pi\left(a^3 - ab^2\right)$ is the difference between the volume of a sphere of radius a and the ellipsoid's volume. The dimensionless volume $V^* = V/V_0$.

The measurements of the interface geometry were adversely affected by optical aberrations resulting from the difference in the indices of refraction of the glass, water, and mineral oil and the device's circular geometry. Specifically, the encapsulated particles appeared smaller in width than their true size. To minimize errors from this distortion, we used the exposed ends of the polystyrene particle for the ellipsoid fitting. This method worked well for the partially encapsulated particles, but posed a challenge when the particles were nearly fully encapsulated since there was little polystyrene-oil interface available for curve fitting.

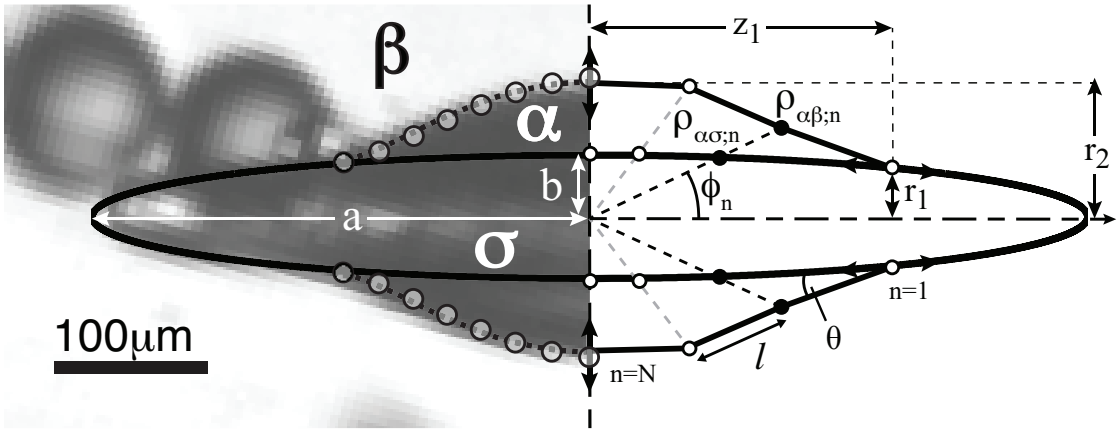

Fig. 2.3: (Left) A photograph of an elongated polystyrene particle (σ) partially encapsulated in a water drop (α) and suspended in a continuous phase (β) of oil. The interface is computed with the unduloid solution (dashed line) and energy minimization (hollow circles). The particle aspect ratio ε=8.0±0.9, the dimensionless volume V^*=0.027±0.007, and the contact angle $\theta = 10^\circ$. The ellipsoid's major (a) and minor (b) axes, the droplet's radius (r_2), and the axial position of the pinning line (z_1) are shown. (Right) The schematic details of the discretized domain used in the energy method. The radial position (ρ) originating from the spheroid's center, the inclination angle (ϕ), the arc length (l), and the node number (n) are shown. The discretization is used in the energy method. See supplement.

2.4. Mathematical Model

In this section, we describe the calculation of the axisymmetric encapsulating drop's shape. We consider three incompressible domains: a rigid elongated particle σ, a droplet α, and continuous phase β (Fig. 2.3). Since the Bond number $Bo = |\rho_\beta - \rho_\alpha| g r_2^2 / \gamma_{\alpha\beta}$, the capillary number $Ca = \mu_\beta U / \gamma_{\alpha\beta}$, and the Weber number $We = \rho_\beta U^2 D / \gamma_{\alpha\beta}$ are all on the order of 0.1 or less (see Appendix I), we assume the droplet to be at a uniform pressure. In the above, $\rho \sim O\left(10^3 kg/m^3\right)$ is the fluid density; g is the gravitational acceleration; $r_2 \sim O(100\mu m)$ is the maximum droplet radius; $\gamma_{\alpha\beta} \sim O(1mN/m)$ is the interfacial surface tension between phases α and β; $\mu_\beta \sim O\left(10^{-3} Pa \cdot s\right)$ is the viscosity; $D \sim O(1mm)$ is the diameter of the glass capillary, and $U \sim O(1mm/s)$ is the average fluid velocity. Clean oil/water interfaces have an interfacial tension $\sim O(10mN/m)$ [49], but the addition of surfactant may lower this number by an order of magnitude [29], [50].

To determine the interface between the drop (α) and continuous phase (β) we employ two different methods. The first method takes advantage of the pressure uniformity inside the drop under equilibrium conditions and in the absence of external fields (Bo<<1). The Young-Laplace equation implies that the interface αβ must have a constant mean curvature. The corresponding axisymmetric surfaces are, therefore, unduloids or Delaunay surfaces [31]. The interface can be specified by a general transcendental expression. We center the Cartesian position vector[34]

$$\mathbf{r}(u,v)=\begin{Bmatrix} r_2\sqrt{1-k^2\sin^2 u}\ \cos v \\ r_2\sqrt{1-k^2\sin^2 u}\ \sin v \\ ar_1F\left(k^2,u\right)+r_2E\left(k^2,u\right) \end{Bmatrix} \qquad [2.1]$$

at the particle's center. The position vector is parameterized by the unduloid's surface parameter *u* and the azimuthal angle *v*. **Bold** and *italic* print letters denote, respectively, vectors and scalars. The functions *F* and *E* are, respectively, the incomplete elliptic integrals of the first kind and second kind. The modulus

$$k^2=1-\left(\frac{\chi r_2}{r_1}\right)^2,$$

where

$$\chi=\frac{r_2\cos\varphi_u-r_1}{r_2-r_1\cos\varphi_u}.$$

In the above, r_1 is the radius of the ellipsoid at the contact line; r_2 is the major radius of the unduloid; and φ_u is the angle that the unduloid's surface makes with the *z*-axis. The contact angle $\theta=\varphi_u-\varphi_e$, where

$$\varphi_e=\arctan\left[-\left.\frac{\partial r}{\partial z}\right|_{z_1}\right] \qquad [2.2]$$

is the angle that the ellipsoid's surface makes with the *z*-axis at $z=z_1$. z_1 is the distance along the *z*-axis from the particle's center to the pinning line.

The ellipsoidal particle, axial pinning position z_1, and the contact angle θ define a unique unduloid. The ellipsoid's radius at the pinning line

$$r_1 = b\sqrt{1-\left(\frac{z_1}{a}\right)^2}\,. \qquad [2.3]$$

The unduloid parameter at the pinning line

$$u_1 = \begin{cases} \arcsin\left[\frac{1}{k}\sqrt{\left(1-\left(\frac{r_1}{r_2}\right)^2\right)}\right] & \text{when } 0 \le \varphi_u \le \pi \\ \pi - \arcsin\left[\frac{1}{k}\sqrt{\left(1-\left(\frac{r_1}{r_2}\right)^2\right)}\right] & \text{when } \pi \le \varphi_u \le 2\pi \end{cases}. \qquad [2.4]$$

Equation [2.4] together with the equation

$$\chi r_1 F\left(k^2, u_1\right) + r_2 E\left(k^2, u_1\right) = z_1 \qquad [2.5]$$

enable us to determine u_1 and r_2.

Our second solution strategy minimizes the system's free energy subject to a volume constraint by discretizing the drop's surface and finding the stationary state. The energy minimization technique can handle more general circumstances than addressed here. In the interest of space, the description of the energy method is deferred to Appendix I. The energy method yielded identical results to the ones obtained when assuming unduloidal surfaces.

2.5. Results and Discussion

We start by comparing the predicted shape of the drop-oil interface with the experimentally observed one. Fig. 2.3 (LHS) overlays the theoretical predictions (dashed line - unduloid surface, and hollow circles - energy minimization) on top of the experimentally observed drop, partially encapsulating an ellipsoidal particle with aspect ratio $\varepsilon = 8.0 \pm 0.9$. The droplet's dimensionless volume is $V^* = 0.027 \pm 0.007$ and the contact angle $\theta = 10^\circ$. Although a couple of small droplets are visible in the background, they do not appear to distort the shape of the interface. Both theoretical predictions are in excellent agreement with each other (<3% root mean square difference) and in good agreement with the experimental data (<13% root mean square discrepancy).

Fig. 2.4.A and B depict, respectively, the drop's dimensionless radius r_2^* (at the symmetry plane z=0) and the dimensionless axial position of the pinning line z_1^* as functions of the dimensionless volume V^*. The lines and circles denote, respectively, theoretical predictions and experimental data. The four curves featured in Fig. 2.4 correspond to permutations of two aspect ratios, ε=2.5 (black line) and 7.5 (gray line), and two contact angles, $\theta = 10^\circ$ (solid line) and 20° (dashed line). Error bars represent one standard deviation. The experimental data (circles) is gray scale-coded (see inset) to indicate the aspect ratio of the particle. The lighter the color is, the larger the particle's aspect ratio. As the color darkens, the particle approaches a spherical shape ($\varepsilon \to 1$). We present theoretical predictions for two different contact angles due to the uncertainty in the actual value of the contact angle, which may have varied from one particle to another and along the surface of a particle. In the range $\theta = 10 - 20^\circ$, the r_2^* predictions were

insensitive to the precise value of the contact angle. The predictions for z_1^* exhibited a greater dependence on the contact angle θ. As V^* increased, so did r_2^* and z_1^*. For a fixed volume, the greater the hydrophilicity (the smaller the contact angle) is, the smaller the droplet radius r_2^* and the greater the distance to the pinning line (z_1^*) are. Generally, the theoretical predictions are in reasonable agreement with experimental observations. The average root mean square discrepancies between the predicted and experimentally observed r_2^* and z_1^* values are, respectively, 3% and 9%. A significant source of error is due to the volume estimate that is calculated as the product of three measured linear dimensions. Additionally, when the particles are long ($\varepsilon >>1$) and the drops small ($V^* <<1$), the free-energy varies slowly with the pinning position (z_1^*), causing a lengthy relaxation time [42]. An experimental error would result when the approach to equilibrium occurs over a time interval that exceeds the observation time in our dynamic experiments [13]. Yet another complication is potential wettability gradients along the particles' surfaces, resulting from non-uniform surfactant absorption and particle stretching during the particle formation process [46].

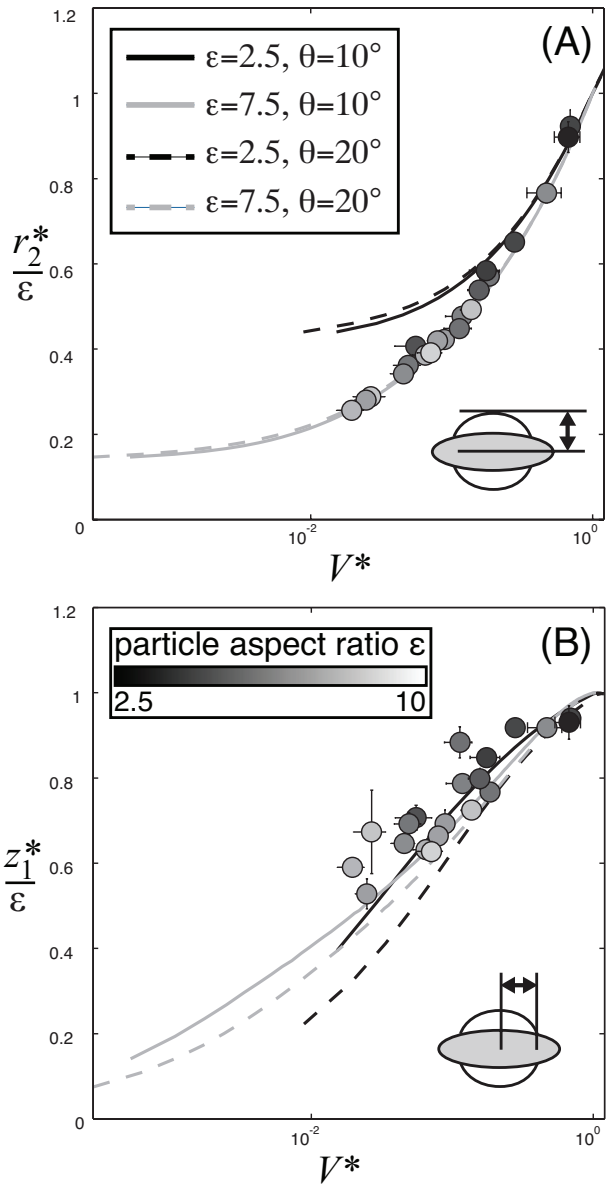

Fig. 2.4: The dimensionless maximum droplet radius $r_2^* / \varepsilon = r_2 / a$ (A) and the axial position of the contact line $z_1^* / \varepsilon = z_1 / a$ (B) as functions of the volume V^*. Experimental data points (circles) are color-coded according to their aspect ratio. Black indicates a stubby particle; the lighter the color, the more slender the particle. The theoretical predictions are depicted for two aspect ratios, ε=2.5 (gray line) and 7.5 (black line), and two contact angles, $\theta = 10^\circ$ (solid line) and $\theta = 20^\circ$ (dashed line).

Next, we predict behaviors that are not readily accessible experimentally. Fig. 2.5 depicts the relationship among various parameters that characterize the unduloid. All variables are dimensionless, and the particle's aspect ratio $\varepsilon = 3$. The abscissa and ordinate are spanned, respectively, by $\left(\chi r_1^*\right)$ and r_2^*. The various solid curves correspond to the specified contact angles. The dashed lines correspond to the drop's volume. For example, when the drop has volume $V^* = 0.05$ and contact angle $\theta = 60^\circ$, $x_2^* = 1.51$ and $\chi x_1^* = -0.29$. Regions I (white) and II (gray) correspond, respectively, to drop volumes $V^* < 1$ and $V^* > 1$. In the latter case, the volume is sufficiently large to allow a spherical drop to fully engulf the particle. The hollow (red) circle represents the state when the drop has a spherical shape, $V^* = 1$, $r_1^* = 0$, $r_2^* = \varepsilon$, and the particle is fully engulfed. See the inset next to the hollow circle. All constant contact angle curves emanate from the hollow circle since as $z_1^* \to \varepsilon$, $V^* \to 1$, indicating that all unduloids approach a spherical configuration in this limit. The region $\chi r_1^* < 0$ corresponds to situations when $\chi < 0$ ($\cos\varphi_u < r_1^* / r_2^*$).

Fig. 2.5 shows that, for each contact angle, there is a maximum volume V_{max}^* that can be supported by an unduloidal drop. The unduloids corresponding to V_{max}^* are denoted with solid (red) dots and can be found explicitly by determining $\left(\chi r_1^*\right)$ and r_2^* when the matrix in

$$\begin{Bmatrix} dV \\ \mathrm{d}\theta \end{Bmatrix} = \begin{bmatrix} \dfrac{\partial V}{\partial (r_1\chi)} & \dfrac{\partial V}{\partial r_2} \\ \dfrac{\partial \theta}{\partial (r_1\chi)} & \dfrac{\partial \theta}{\partial r_2} \end{bmatrix} \begin{Bmatrix} \mathrm{d}(r_1\chi) \\ \mathrm{d}r_2 \end{Bmatrix} \qquad [2.6]$$

becomes singular for a given contact angle. When $V^* > V^*_{max}$, the drops are spherical and completely engulf the particle (i.e., Fig. 2.2.C).

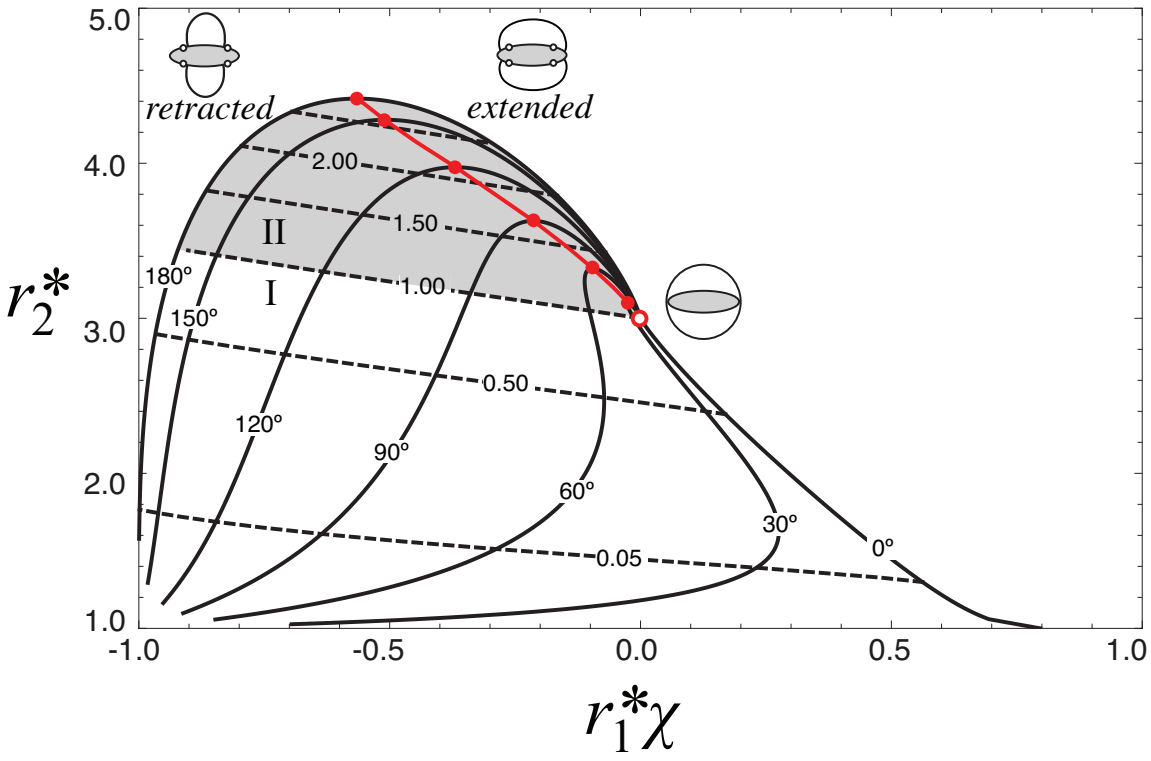

Fig. 2.5: Contours of constant contact angle θ and constant volume V^* are depicted in the space of the unduloid coefficients (χr_1^*) and r_2^*; $\varepsilon = 3$. Regions I (white background) and II (gray background) correspond, respectively, to drop volumes $V^* < 1$ and $V^* > 1$. The hollow (red) circle denotes the smallest fully engulfing, spherical drop with $V^* = 1$. The solid dots indicate the maximum possible unduloidal drop volume at a given contact angle.

When $V^* < 1$, Fig. 2.5 illustrates that there is only one possible unduloidal drop configuration for any given drop volume and contact angle. When $V^* > 1$, multiple unduloidal drop configurations are possible, however. Witness that, when $V^* > 1$ and $\theta > 0$, constant volume curves intersect constant contact angle curves twice. In other words, there are *three* possible axisymmetric drop configurations: two consisting of partial engulfment (the right and left insets at the top of Fig. 2.5) and one of complete engulfment (Fig. 2.2.C). To obtain further insight into the two possible partially engulfed configurations, Fig. 2.6 depicts the two unduloids when $\theta = 60^\circ$ and $V^* = 1.2$ (solid lines). We include in the figure also a third unduloid having the limiting volume $V_{max}^* = 1.34$ ($\theta = 60^\circ$, dashed line). We refer to this unduloid as the limiting drop. This third unduloid corresponds to the red solid dot in Fig. 2.5. For better visibility, we enlarge the region next to the contact line in the inset. We refer to the drop configurations to the left and right of the limiting drop as the *retracted* and *extended* branches, respectively. Let's consider a gedanken experiment in which one gradually increases the drop's volume. As the drop volume increases, both the contact lines associated with the retracted and extended branches approach the position of the drop with the limiting volume. The contact line of the retracted branch migrates away from the particle's center, increasing the particle's wetted area, as we observed in the experiments. Counter to intuition, the extended drop contracts as its volume increases. The extended configuration always has a lower curvature than the extended branch. To determine which branch is preferred, we will consider the surface energy of each configuration.

In addition to the two axisymmetric pinned, barrel states (**B**) and the fully engulfed (**FE**) state that we already discussed heretofore, other stationary states are possible, such

as an axially-asymmetric clam-shell (**C-S**) [36] and an expelled (**EX**) state in which the particle resides entirely in the continuous phase, outside the drop. In this paper, we have restricted ourselves to axisymmetric configurations, and we cannot comment on possible transitions to the **C-S** state. We will compare, however, the free energies of the various axisymmetric states. We use the expelled state as the reference state (state of zero energy). Fig. 2.7 depicts the dimensionless free-energies $\left(\Delta E^*\right)$ of the pinned states (solid lines) and, when admissible, of the engulfed states (dotted lines) as functions of the volume V^* for various contact angles θ. The particle's aspect ratio $\varepsilon = 3$. We use γb^2 as the energy scale. We identify three regions. In region I ($V^* < 1$), only one pinned axisymmetric conformation is possible. In region II ($1 < V^* < V^*_{max}$, shaded area), full encapsulation (dashed line) and two pinned solutions (solid lines) are possible. The two pinned solution branches meet at $V^* = 1$. The lower and upper, pinned branches correspond, respectively, to the retracted and extended states. The retracted state is a state of lower energy than the extended state. In region III ($V^* > V^*_{max}$), no pinned solutions are possible. When $\theta < 70^\circ$, the pinned, retracted state is the lower energy state while the engulfed and expelled states are metastable. When $\theta > 70^\circ$, expulsion is the preferred state. In the neighborhood of $\theta = 70^\circ$, the energy is non-monotonic and high volumes prefer a pinned state while lower volumes prefer expulsion.

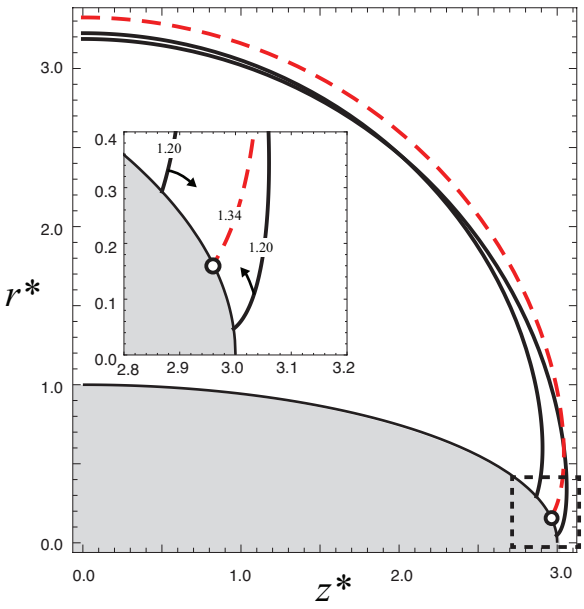

Fig. 2.6: The shapes of the two solution branches ($V^* = 1.20$, solid lines) and that of the limiting drop ($V^* = 1.34$, red line). $\theta = 60^\circ$ and $\varepsilon = 3$.

To better clarify the energy landscape in region II, Fig. 2.8.A magnifies the region enclosed in the dotted rectangular frame of Fig. 2.7 ($\theta = 60^\circ$). Fig. 2.8.B depicts the position of the pinning line when the drop is pinned ($z_1^* < \varepsilon$, $V^* < V_{max}^*$, solid lines) and the radius of the engulfing spherical drop (when $V^* > 1$, dashed line). Let's consider a hypothetical experiment in which one gradually increases the volume of the drop from state A. When $V^* < 1$, only the pinned, retracted state (solid line) is possible (see inset next to A). Once V^* exceeds one, an additional pinned state, an extended state (solid red), and an engulfed state (dashed line) becomes possible. In the gray region ($1 < V^* < V_C^* = V_{max}^*$), three states coexist. When $1 < V^* < V_B^*$, the pinned, retracted state is the state of lowest energy. When $V^* = V_B^*$ (state B), the engulfed and pinned states have the same energy. When $V_B^* < V^* < V_C^*$, the engulfed state is energetically most favorable.

Point C is a limit point at which the retracted and extended pinned branches meet. When $V^* > V_C^*$, only the fully engulfed state exists. In the hypothetical experiment, one would anticipate that when the drop volume is gradually increased, the pinned, retracted state would persist until $V^* = V_D^*$. Further increase in volume will induce a discontinuous transition to the engulfed state (D). If one were to gradually decrease the drop volume from state (D), the system would likely follow a different path, a path of engulfed states, up to state (E) before jumping discontinuously to the pinned state (F). The "extended" pinned branch, which provides an alternative route between (C) and (E), is likely inaccessible. In the above, we described a potential hysteretic behavior in which the system follows different paths in the directions of increasing and decreasing volumes when $1 < V^* < V_{max}^*$.

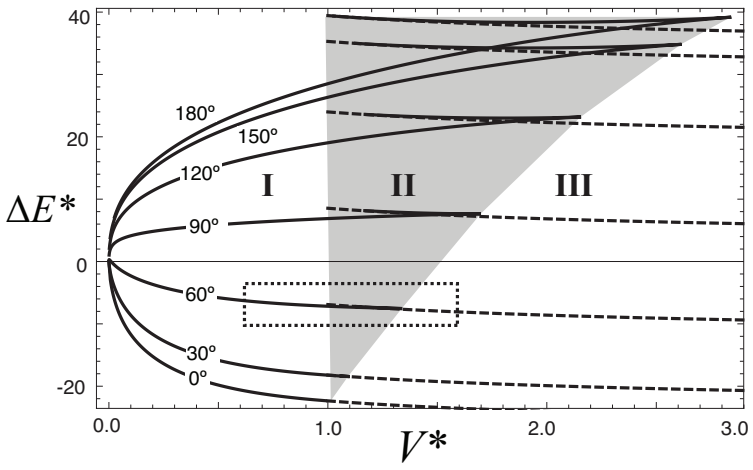

Fig. 2.7: The free energy relative to that of the expelled state as a function of normalized volume. The solid and dashed lines correspond, respectively, to pinned drops and engulfing drops. The shaded region corresponds to the parameter space where multiple equilibrium states coexist. The particle aspect ratio ε=3.

Next, we examine the axial force that the drop applies on the particle

$$F^*_z = -\pi\left\{2r^*_1\cos(\varphi_u) + \left(1-r^*_1\right)\kappa^*\right\}. \qquad [2.7]$$

In the above, $\kappa^* = b\kappa$ is the dimensionless uniform curvature (twice the mean curvature) of the drop. Fig. 2.9.A depicts the normalized curvature as a function of the normalized volume V* for various contact angles. The force is normalized with $b\gamma_{\alpha\beta}$. The first term in eq. 8 is the force exerted by the contact line on the particle. This force can be either compressive or tensile depending on the magnitude of the angle of the tangent to the drop's surface φ_u. The second term in [2.7] results from the Laplace pressure acting on the particle's surface. This force is always compressive in the case of a prolate ellipsoid. Fig. 2.9.B depicts the axial force F^*_z as a function of the droplet volume V^* for several contact angles. Positive and negative F^*_z represent, respectively, tension and compression. When the drop is wetting ($\theta < 90^\circ$), the contact line exerts a compressive force. When $\theta > 90^\circ$, tensile force is possible. The transition from compression to tension occurs when the pinning line force balances the compressive force due to the pressure in the drop.

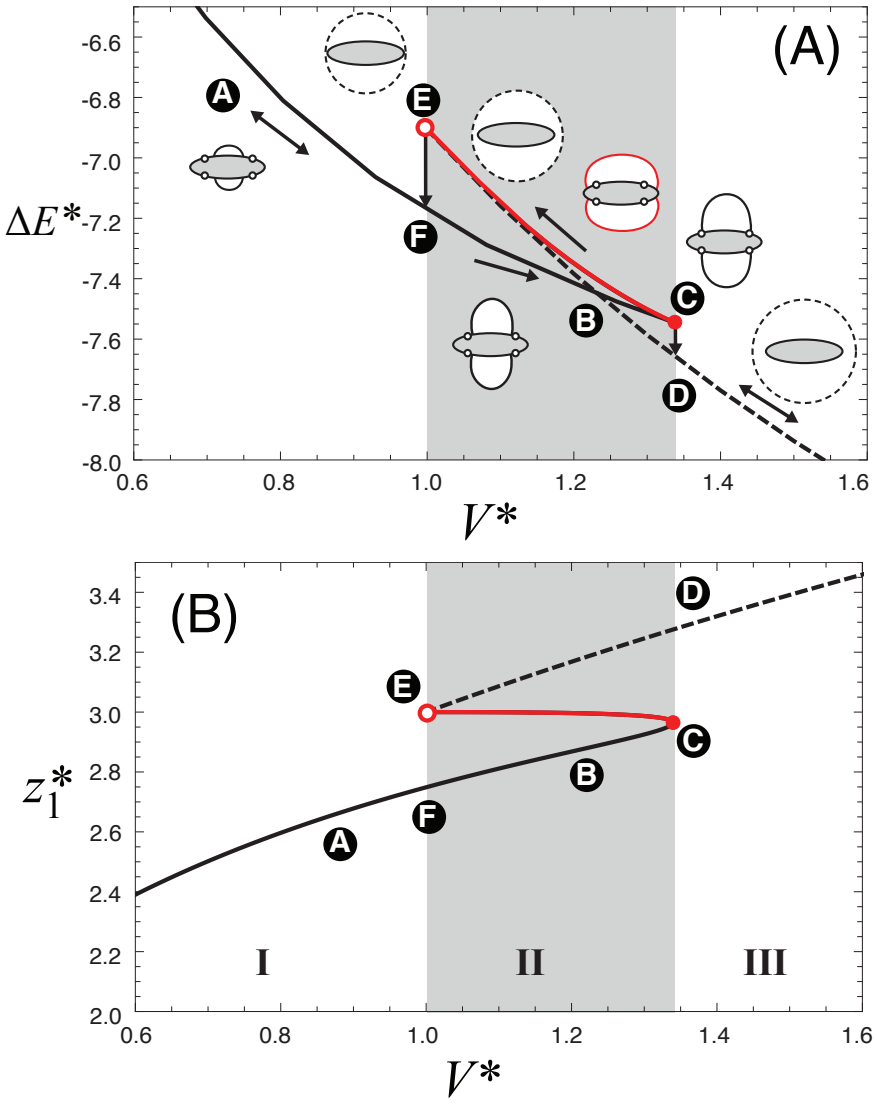

Fig. 2.8: A magnified image of the framed region in Fig. 7. ΔE^*(A) and z_1^* (B) are depicted as functions of V^*. $\theta = 60^\circ$ and $\varepsilon = 3$. The arrows describe a gedanken experiment.

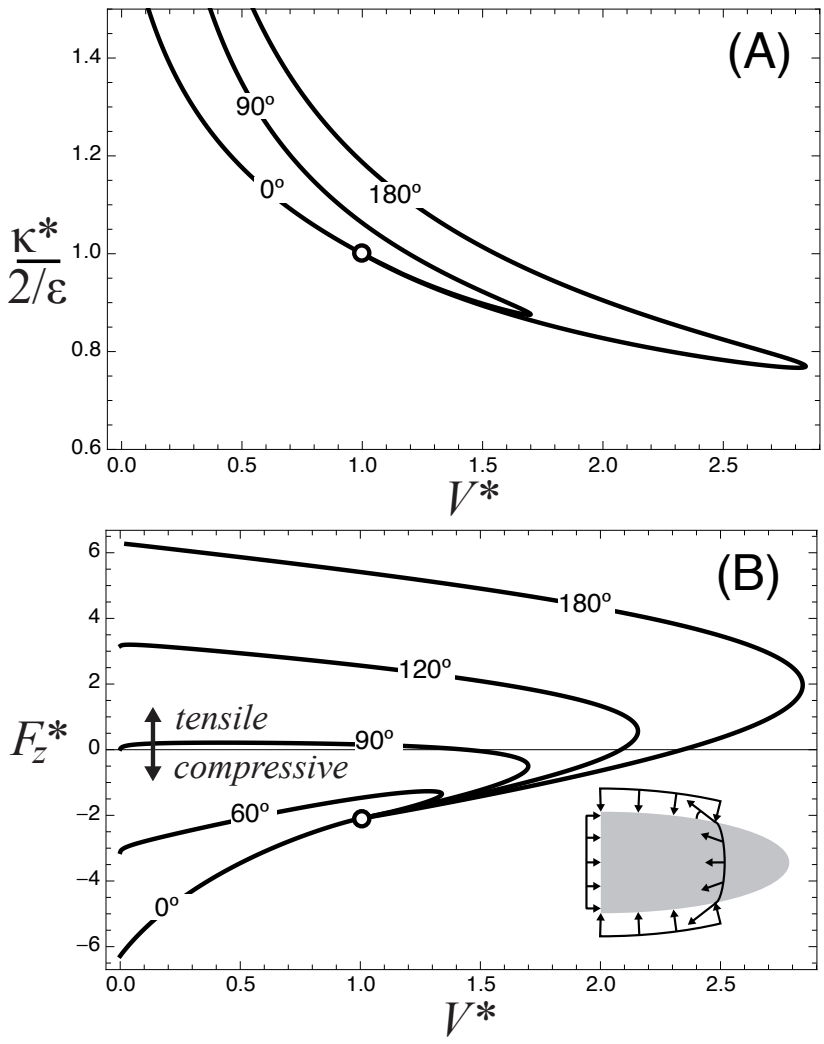

Fig. 2.9: Normalized curvature (A) and axial force (B) as functions of dimensionless volume; $\varepsilon = 3$. Hollow circle denotes a spherical, engulfing drop.

2.6. Conclusion

We have studied the shape of axisymmetric drops enclosing a slender, ellipsoidal particle as a function of drop volume and contact angle. Calculations of the droplet geometry were carried out using two different methods that yielded nearly identical results. The theoretical results agreed favorably with experimental observations.

The theory shows that there is a maximum volume that can be supported by pinned unduloidal morphologies. It remains, however, to be seen whether or not volumes beyond this limit point can be supported by asymmetric clam-shell states. Similarly, while we have identified multiple stationary states and the possibility of hysteretic encapsulation behavior, further investigations are required to determine if these transitions are physically realizable given that asymmetric morphologies may be preferable in certain cases. Our work was also limited to rigid particles. Another interesting extension of the work would be to address the behavior of flexible (compliant) particles.

Chapter 3. Liquid-Gas Interface Observations in SEM and TEM

3.1. Motivation

In recent years, investigations into the existence and stability of nanobubbles (100s of nanometers and below) have been pursued by many groups [51]-[64]. The hypothesis of persistent surface-bound nanobubbles began as a result of indirect measurements; it was found that the force between two hydrophobic surfaces immersed in water varied in a step-wise matter at the sub-micron scale. The magnitude and discrete nature of the force jumps were not consistent with predictions based on Van der Waals forces and were ultimately attributed to nanobubble coalescence and/or adsorption events. A review of these findings can be found in Parker *et al*. [65].

In Engineering applications, nanobubbles have been implicated in the anomalous scrubbing of interfaces exposed to ultra sound [66], [67] and the ease with which heterogeneous nucleation of vapor bubbles occurs after repeated cycles of heating [68]. Recent experimental investigations have relied on the solvent-exchange method to reliably deposit surface nanobubbles on hydrophobic surfaces and the use of atomic force microscopy (AFM) for observations. However, these measurements are temporally restricted to the scanning rate of the AFM tip. The AFM measurement is also intrusive. As a result, it is still unclear whether the bubbles nucleate heterogeneously, or if nucleation occurs homogenously and is followed by surface adsorption[69]. It also remains difficult to directly assess nanobubbles' role in physical processes without real-

time direct observations. The spatial and temporal resolution of electron microscopy makes it an attractive imaging tool to complement AFM measurements. The large density difference between liquids and gases make liquid-gas interface easy to spot with electron microscopy.

Electron microscopy has existed since the 1930's, beginning with the development of the transmission electron microscope (TEM) and followed by the scanning electron microscope (SEM). While the desire to visualize liquids and liquid-bound samples by way of electron beam illumination has existed for a long time, the low operating pressures required to maintain a coherent electron beam have prohibited such investigations. Environmental scanning electron microscopy (ESEM) allows the observation of samples such as hydrated solids but still operates at pressures too low for prolonged observations. Because secondary electrons are used for imaging, the ESEM is not capable of probing deep within a liquid sample. The strong need to interrogate aqueous nanometer scale phenomena has precipitated the creation of a fairly new field of study, liquid cell electron microscopy. The maturation of micro-fabrication techniques has made possible the development of pressure vessels thin enough to allow transmission of electrons with minimal scattering (so as to work with TEMs and SEMs operating in transmission mode), but mechanically robust enough to maintain pressure differences of multiple atmospheres. A review of recent liquid cell technology and a detailed description of the device used in this work can be found in [70].

While the issue of containment has been to a large degree surmounted by using Silicon-Nitride or Graphene as window materials, there are additional imaging and experimental issues specific to electron microscopy of liquids that need to be considered.

Primarily, interactions between the electron beam and the irradiated material can be strong and manifest themselves through thermal, electrical, and chemical means.

The chemical effects in particular have received an increasing amount of attention lately. Exposing water to high-energy electrons induces changes in pH and hydrogen peroxide concentration through a process called radiolysis. The changes have important effects on the growth of electro-deposited films, nanoparticle stability[71], and precipitation of cations from solutions of metal-salts[72]-[74]. Indeed, chemical changes are drastic enough to produce large amounts of molecular hydrogen and oxygen that may form bubbles under certain conditions [15], [72], [75].

While radiolysis bubbles are often an undesirable occurrence in liquid cell experiments, their growth and movement will be the focus of this and subsequent chapters. In addition to providing a way to probe fundamental interfacial phenomena, understanding nanobubble movement may have immediate benefits to the liquid cell community who wish to mitigate their influence on experiments. In this chapter, observations will be qualitatively and quantitatively discussed. Recent studies have shown that electron radiation can induce condensation [76] and mediate electro-wetting phenomena [77], [78]. The goal of this chapter is to understand the mechanisms of nanobubble migration and growth.

3.2. Experimental Methods

Nanoaquarium liquid cells[70] were loaded with a solution of gold nano-rods which possessed trace amounts of cetrimonium bromide (CTAB) surfactant. A schematic cross-

section of the device used is shown Fig. 3.1. Nano-bubbles were ostensibly created from the interaction of products of water radiolysis resulting from the electron irradiation [15], [16] of a transmission electron microscope (Hitachi H9000) with water. We used a 300 keV beam, a current of 1-10nA and a beam radius ~2 um. An optical fiber transfers light from the TEM's phosphor screen to a CCD (charge-coupled device) and stores images on a digital tape at a rate of 30 frames per second.

Changing beam settings affords some control over nanobubble growth [15], [72], [75]. However, in general nucleation sites and the dissolved concentration of oxygen and/or hydrogen cannot be controlled or measured directly. Additionally, the internal pressure of the device cannot be measured directly and can only be estimated in serendipitous circumstances; thus the difficulty in knowing the level of super-saturation is further confounded. The loading procedure requires the application of set-screws to a set of O-rings. As a result, the pressure of the device is highly sensitive to the final setting of these screws and the volume of fluid loaded.

The thin (~50nm) silicon-nitride membranes that encapsulate the liquid sample are capable of large strains. The square 100x100 um membranes have been shown to bow outward 100s of nanometers or more when holding 4 atmospheres against vacuum. This mechanics problem has been tackled previously in the literature; an analytical result found by Maier-Schneider furnishes a relationship between pressure and deflection [79]. Fig. 3.2 (left) plots the membrane deflection as a function of position for a few internal pressures. This model also provides us with the slopes of the membrane that we can expect to find in the experiment, which are on the order of $10^{-5} - 10^{-1}\,\mathrm{rad}$, see Fig. 3.2 (right).

In an auxiliary experiment, loaded liquid cells were viewed using STEM and the deflections were compared to the predictions of the thin membrane-bending model with pressure as the unknown variable. We conclude that pressures from 0.05 to 4 atmospheres can be expected, one such example is plotted in Fig. 3.3. For simplicity, we assume that image intensity is linearly related to liquid thickness (this is valid in the limit of very thin samples). We calibrate the relationship between thickness and intensity (which has two unknowns) by noting that the thickness of liquid near the edge of the window must be 200 nm and that after the bubble has formed the liquid thickness is ~0 nm.

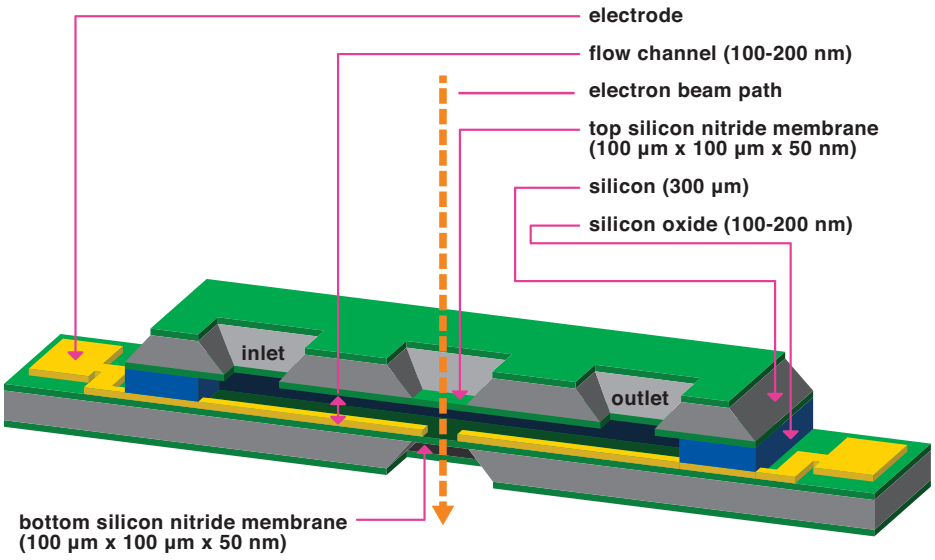

Fig. 3.1: A schematica cross-section of the microfabricated lqiuid cell described in [70]. The schematic shows etched Silicon (gray), Silicon-Nitride (green), Silicon-Oxide spacer (blue), and electrodes (yellow) for use in electrochemical experiments.

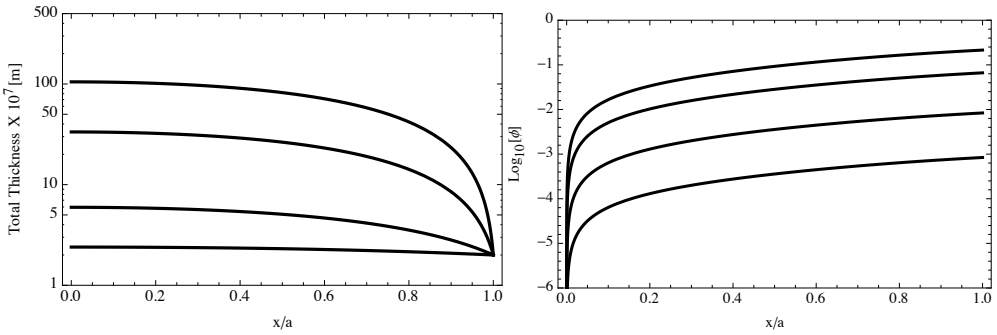

Fig. 3.2: (Left) Total cell thickness and (Right) slope as a function of dimensionless position where a is the half-width of the membrane $a = 50\mu m$ (the origin is at the center of the membrane) for $P/P_{atm} = 10^{-2}, 10^{-1}, 10^{0}$ and 10.

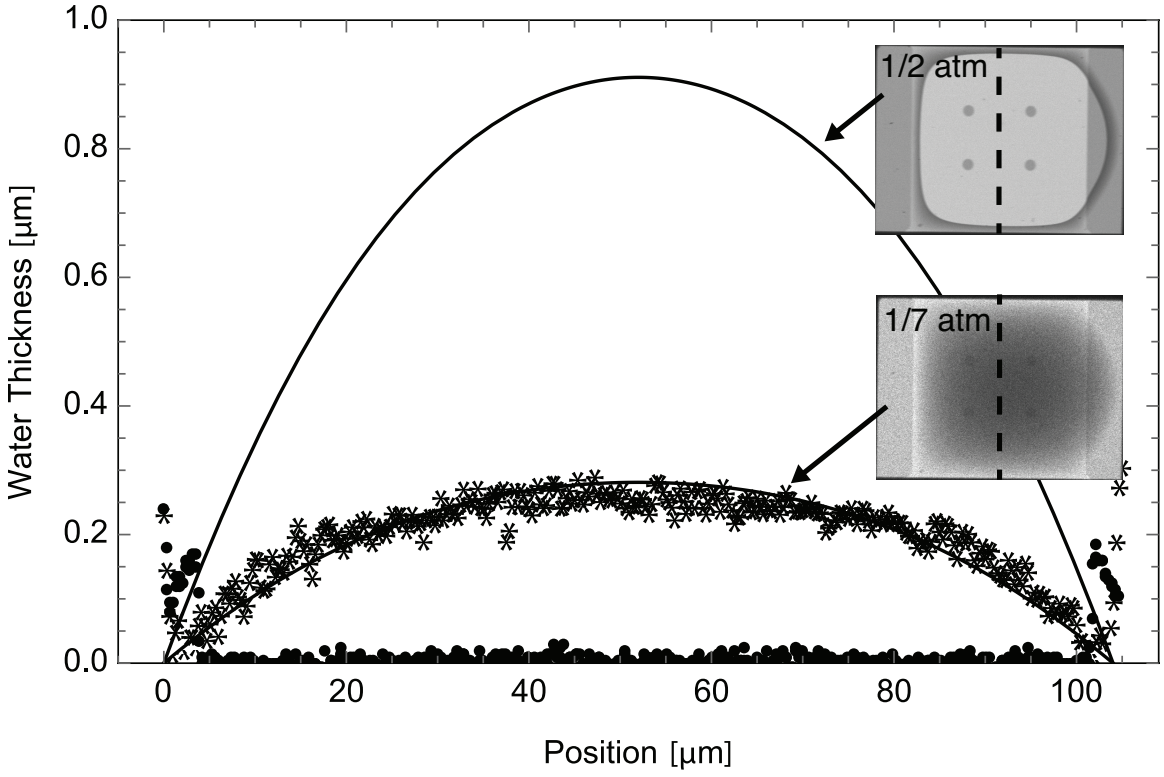

Fig. 3.3: Intensity profiles from two STEM images (inset) before (bottom) and after (top) bubble creation converted to water thickness (asterisks and circles correspond, resptively, to before and after bubble creation) compared to the Maier-Schneider theory[79]. Estimated pressures were respectively ~1/7 and ~1/2 of an atmosphere.

However, this theory is only applicable under idealized circumstances. During manufacturing of the liquid cell or during filling, the imaging chamber's roof and ceiling can be drawn together by capillary forces to form a collapsed structure. Fig. 3.4 shows light microscopy images of the filling process impeded by window adhesion. The schematics show the cross-section (deformations are exaggerated for clarity). Typically, loading the cell and subjecting it to vacuum is sufficient to separate the membranes. When they do not separate, however, gaps of less than the nominal $200[\mathrm{nm}]$ are also possible. The optical clarity and the limited mobility of, to be described, $\sim 10[\mathrm{nm}]$ bubbles strongly suggests that this is the case for the experiments discussed in this thesis. Color variations in Fig. 3.4 are due to constructive and destructive interference of different wavelengths. Since neither monochromatic light nor filters were used in the acquisition of the image, performing a true quantitative analysis was not possible. However, we know that interference peaks of green light ($\lambda = 540$ nm) occur every ~150 nm of additional water thickness (the order of magnitude is similar for other visible wavelengths) [70]. Because we see very few striations for each color, we can conclude that the membrane is undergoing deformations on the order of ± 100 nm .

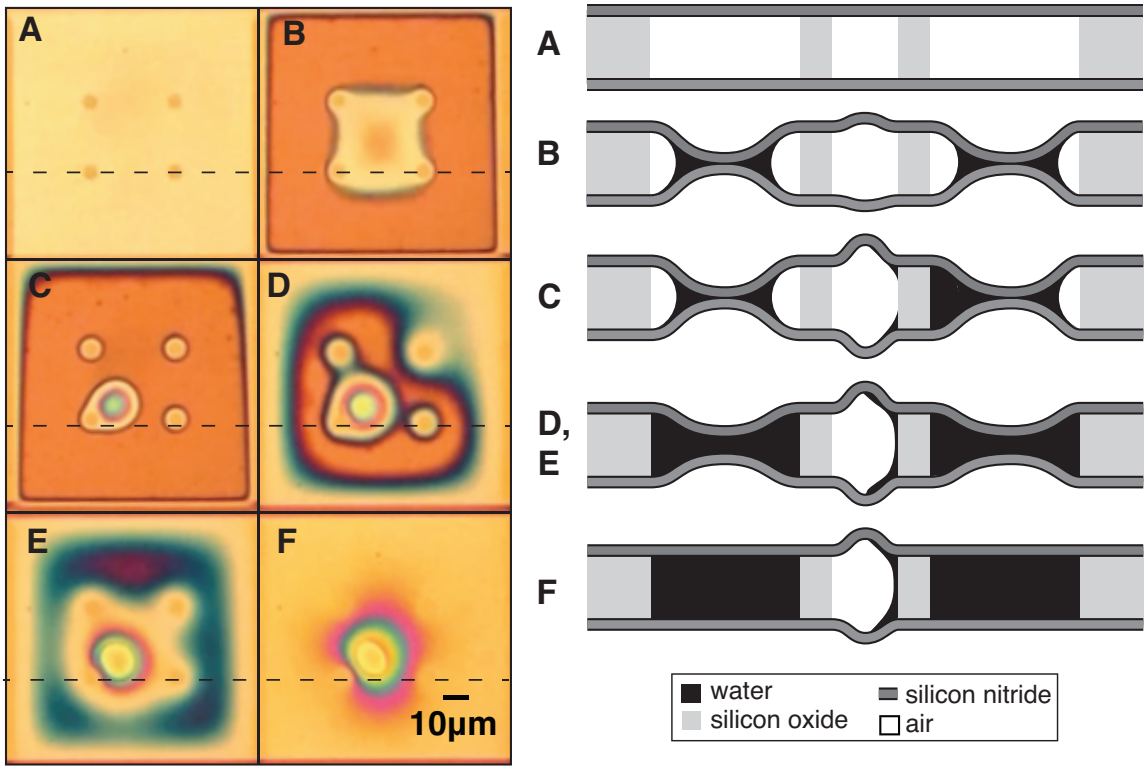

Fig. 3.4: (Left) Light microscope images of the silicon nitride membrane at various stages of liquid cell filling and (Right) a schematic of the cross-section along the dashed line (not to scale, deformations are exageratted for clarity). Color variations are due to height variatons that result in constructive and destructive interference of different wavelengths. (A) Unfilled liquid cell. (B-C) Capillary action pulling the windows together, and trapping an air bubble. (D-F) After adding liquid to the ports, the membranes spontaneoulsly relax, note that the bubble's projected area increases.

3.3. Initial Observations of Sub-Micron Bubbles in TEM

To begin the discussion of sub-micron bubbles, consider the composite image in Fig. 3.5. The images were manually selected from a video recording of a TEM experiment; common image elements were used as reference points to align the images. The composite shows various bubble morphologies: bubbles that might be described as

circular or spheroidal on one end of the spectrum, or elongated, tear-drop-like, or finger-like, on the other. Additionally, the image shows variations in the intensity of the regions outside the bubbles indicating that the liquid is non-uniform. At the level of an individual still, vignetting around the edge is a result of the finite illumination of the beam and the fiber-optical system that transmits the phosphor image to a CCD. By examining a collection of images, however, it becomes apparent that there are larger scale gradients in the transmission of the sample that cannot be attributed to the optical system alone. Specifically, note that the upper-right quadrant in the composite is generally darker than the lower-center.

Qualitative observations reveal that all bubbles with the same nucleation site migrate in a common direction. In the particular composite (Fig. 3.5), the bubbles were generally moving towards the upper-right. To confirm and quantify this, a simple series of image processing steps were applied in Mathematica to track the centroids, hydraulic radii, and the principal values and axes of bubbles. The first step of the scheme consists of manually finding or constructing a "blank" TEM image where no water is present so that it may be subtracted from any frame of interest to minimize the impact of vignetting. Such an image is shown in Fig. 3.6. After subtraction, noise is removed by applying a Gaussian blur function, and a black and white image is created using a "Binarize" filter (a simple function that replaces all pixels above a specified threshold with a "1" white and those below it with a "0" - black) with appropriate level set. Finally, a Mathematica function "Morphological Components" is used to acquire several metrics of bubble geometry and motion for all bubbles within a frame. These include projected area, hydraulic radii, principal values and orientation of a bounding ellipse, and centroid

position. This series of steps is repeated for manually selected sections of footage and yields a "disordered" matrix where each row represents a unique bubble and frame, and contains the aforementioned quantities and the frame number. The matrix is disordered in the sense that there is no explicit structure. For example, each line contains the information of one bubble, the following line could be the same bubble at a different frame, or a different bubble at either the same frame or a different frame.

While such an unstructured list might be useful to obtain statistics on bubble features, it is also of interest to track the temporal evolution of radius, aspect ratio, etc. of an individual bubble. To appropriately create this structure, the resulting matrix is exported to Matlab where a version of John. Crocker and Eric Weeks' particle tracking code (ported to Matlab by Daniel Blair and Eric Dufresne) is used to stitch together bubble trajectories [80], [81]. The code examines particle centroids and time stamps to identify bubbles across frames; the additional parameters are simply along for the ride. Trajectories created using this process from a few different locations within a liquid cell are plotted in Fig. 3.7.

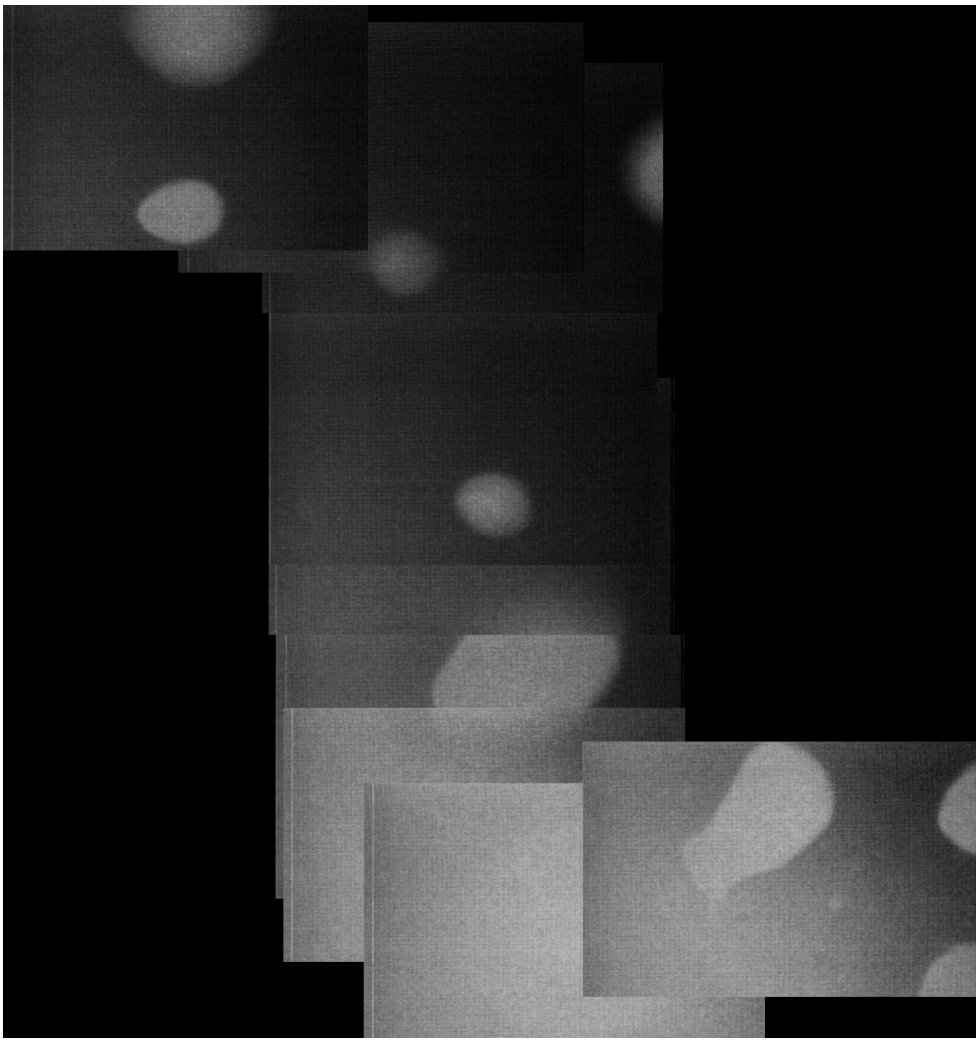

Fig. 3.5: Composite image created from several TEM images observed at a magnification of 5,000X. All images are unaltered to illustrate the difference between vignetting and larger scale transmission gradients. Each still is $1.8[\mu m]$ across.

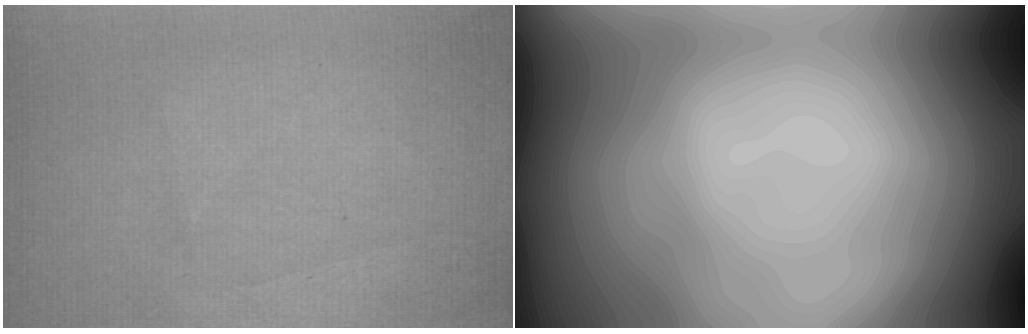

Fig. 3.6: (Right) TEM image of an empty liquid cell and (Left) the same image with enhanced contrast, illustrating vignetting.

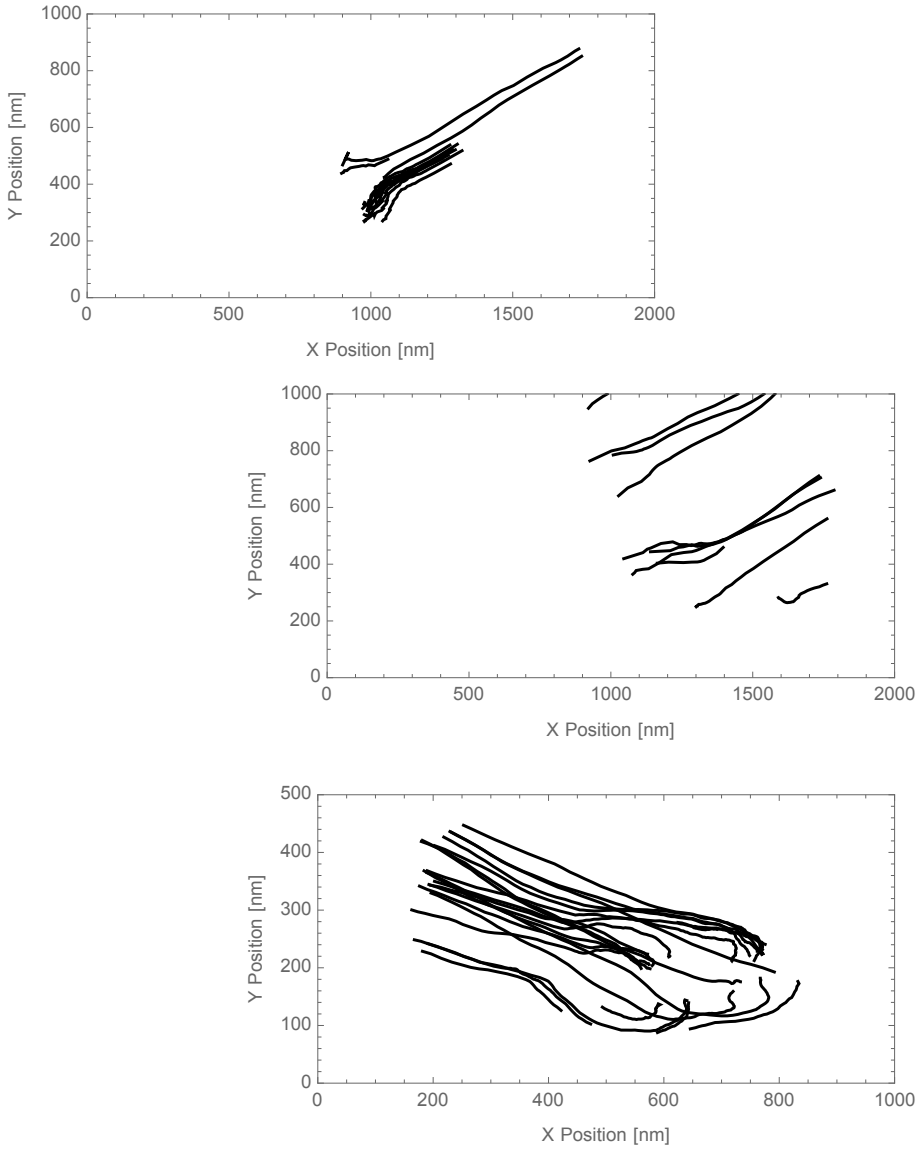

Fig. 3.7 : Trajectories of bubbles observed at three different nanoaquarium locations. (A – top) and (B - middle) are observations made at 5,000x, (C - bottom) is at 10,000x.

3.4. Bubble Transport Hypotheses

We now address possible mechanisms for the observed bubble locomotion. We begin with beam-centric physics, since there is some precedent in the literature for strong beam-liquid interactions. Firstly, energy deposited in the liquid-cell can locally heat the membrane and liquid. Even though the estimated temperature increase is small[72], surface tension is a function of temperature and a discrete bubble might experience Marangoni driven propulsion [50]. The magnitude of Marangoni effect on a spherical bubble can be estimated by calculating Marangoni number

$$\mathrm{Ma} = \frac{d\gamma}{dT}\left|\frac{dT}{d\mathbf{x}}\right|\frac{R^2}{\eta\alpha} \quad . \qquad [3.1]$$

In the above, the bubble radius $R \sim 10$ nm, the thermal diffusivity of the suspending liquid $\alpha = 1.43\times10^{-7}$ m^2/s, the liquid viscosity $\eta = 8.9\times10^{-4}$ Pa s, $d\gamma/dT \sim 2\times10^{-4}$ J/m^{2}K, and $\left|dT/d\mathbf{x}\right| \sim 1\times10^{6}$ K/m. We find that $\mathrm{Ma} \sim \mathrm{O}\left(10^{-4}\right)$. An estimate for the temperature gradient is arrived at by using the beam radius $\sim 1\mu m$ and a temperature rise of 1 K [72]. While small, we continue with the thought experiment. Motion of the bubble through this mechanisms result because a surface tension gradient proportional to the temperature gradient is introduced along the surface of the bubble. Such a gradient creates in a tangential force that must ultimately be balanced by viscous stresses, this forms a toroidal recirculating flow within the bubble driven by the surface motion. Since surface tension tends to decrease with increased temperature, this flow diverges at the hot side of the bubble as the surface is pulled away from the area of low surface tension, and converges at the cold pole. This action would, therefore, tend to propel the bubble towards the hotter region of the beam center. In the experiment, we

observe some bubbles migrating towards the beam's center, while others away from it. Thus, surface tension gradients cannot be the dominating force responsible for bubble locomotion.

Another effect is local charging of the membrane[77] or the localized introduction of free charge into the liquid by way of radiolysis[15]. Such charging can have at least two effects on the fluid. If one can argue that the beam precipitates a region of high electric field intensity through some mechanism, then the expulsion of the less polarizable bubble in favor of highly polarizable water is plausible. Similarly, for bubbles that wet the Silicon-Nitride, local changes in contact angle, which favor the wetting of water, are also possible. Several groups in the liquid-cell community have noted such manipulations of water by the beam, though the physics remain ambiguous because the interactions between high-energy electrons, and thin solids and liquids are still ill understood[76]-[78]. Electro-wetting, like polarization forces, would tend to draw liquid towards the irradiated region, and expel bubbles.

A common denominator that all these mechanisms share is that they are beam-centric; they propose energy gradients that would tend to evacuate all bubbles from the field of view, or draw them to it, regardless of position. However, this is inconsistent with the large majority of observed trajectories. For a given location, trajectories seem to have one preferred direction that is not radially outward from the beam center, and which seems to persist even as the viewing area changes. Bubbles either nucleate in the field of view and exit or pass through the viewing area; bubbles have never been observed that enter from out of the beam region and seek the beam center. Examining the intensity

profiles of bubbles more closely will suggest a different mechanism that does not rely on beam-induced effects.

As the electrons travel through the irradiated medium they are scattered, thus darker sections of the image indicate more scattering events and a thicker liquid layer. Gradients in intensity therefore correspond to variations in liquid layer thickness and a varying geometry of the liquid cell. This allows us to note two related features that signify a locally tapered geometry of the liquid cell. Firstly, consider the bubble in Fig. 3.8 and its intensity profile taken along its direction of motion (white arrow); the dotted line hi-lights the drop in background intensity from aft to fore supporting the idea of a varying cell geometry. Secondly, we note that bubbles' edges are not sharply defined; this is because there is some curvature to the interface. However, the distance over which the transition from the bubble's interior to the background intensity tends to vary along the perimeter of a given bubble. That is, portions of a bubble's perimeter appear sharp while others appear softer or more blurred. Fig. 3.8 shows a typical migrating bubble along with an intensity profile taken along its direction of motion. The intensity slice highlights the extrema of these gradients: sharpest at the trailing edge of the bubble, and more gradual at the leading edge.

We find that the bubbles tend to migrate towards the darker region, like in in Fig. 3.8, and that when bubbles appear non-circular, they're axes also point towards these regions. To quantify this effect for all observed bubbles, regions of video frames devoid of bubbles are examined to create maps of the background intensity gradient ∇I. We assume that, to first order, these gradients are proportional to the confinement gradient ∇h. Using the image processing steps described earlier, we collect all bubble aspect

ratios in a histogram, Fig. 3.9**.**A, to establish that, in general, bubbles possess some elongation even if it is slight. Fig. 3.9**.**B depicts the distribution of the angle between the direction of the bubble velocity vector $\dot{\mathbf{x}}$ and the direction of the intensity/confinement gradient ∇h (light gray), and the distribution of the angles between the bubble's principal axis $\mathbf{p}$ (arrow in Fig. 3.9**, inset**) and ∇h (dark gray). Both distributions peak when the vectors are aligned. The preferential growth and migration in the direction of the confinement gradient ∇h, common to all bubbles, suggests that the observed dynamics are dominated by confinement gradients.

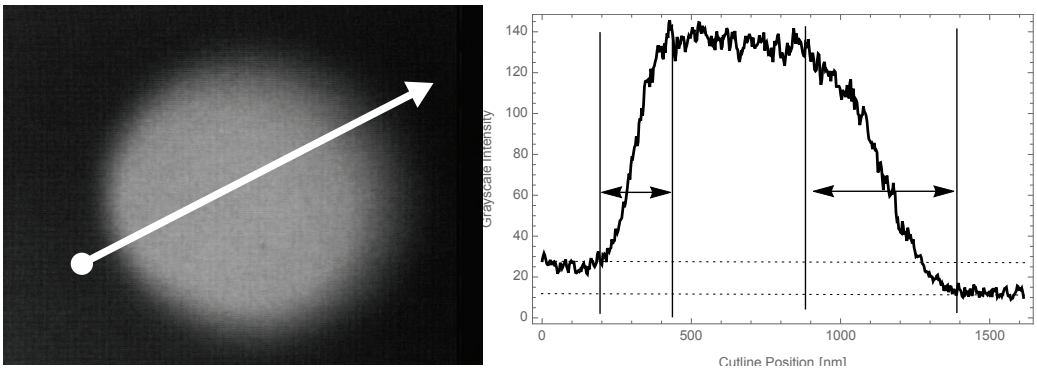

Fig. 3.8: A typical bubble and its intensity profile taken along the principal axes and the direction of motion. Markings on intensity profile illustrate the drop in background intensity that occurs across the length of the bubble.

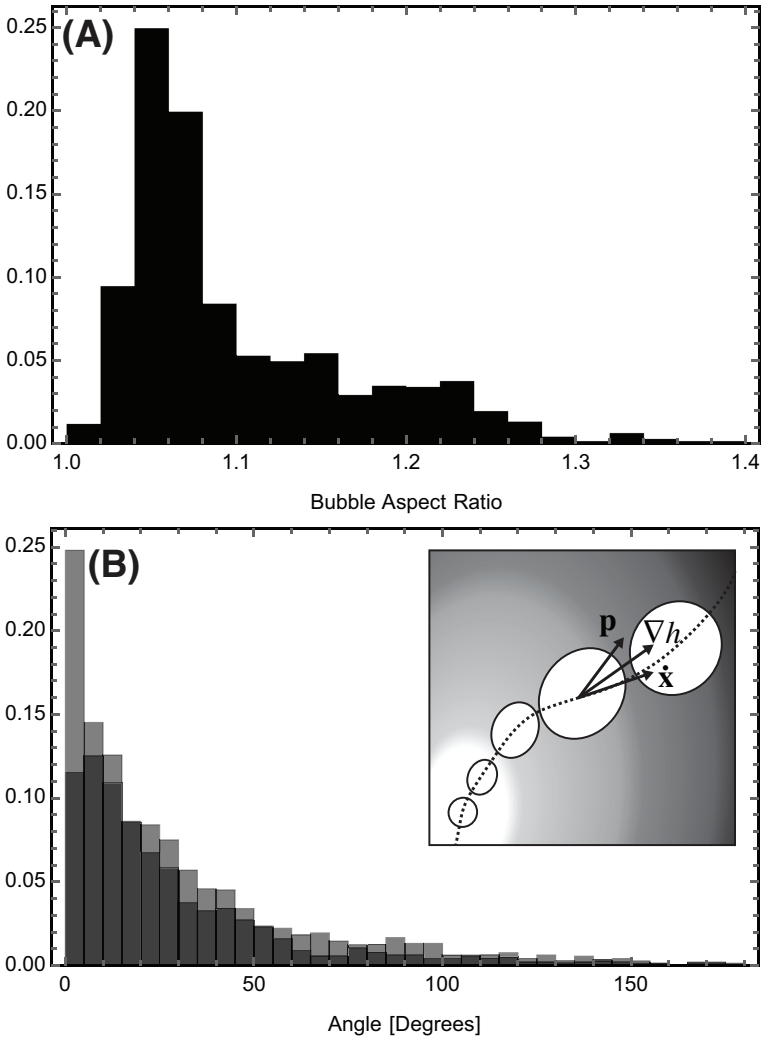

Fig. 3.9: (A) Fraction of bubbles as a function of aspect ratio for bubbles observed at 5000x from 5 different nanoaquarium locations. (B) Angle between background intensity gradient $\propto \nabla h$ and velocity (light gray) and angle between bubble's principal axis $\mathbf{p}$ and velocity $\dot{\mathbf{x}}$ (dark gray). The inset shows a schematic of a bubble whose position, radius, and aspect ratio evolve in time with the vectors for velocity, background gradient, and principal axis labeled.

Another strong indicator that bubbles move because of confinement gradients is that bubbles that appear very "soft" do not move at all. Fig. 3.10.A shows such a bubble, along with an intensity profile. We assert that such bubbles are not large enough to have adhered to both membranes (bridge between both membranes) because they do not possess the characteristic plateau in their intensity profile (as seen in Fig. 3.8 and Fig. 3.10.C) and therefore are not subject to confinement gradient driven motion. Furthermore, elongated geometries, like Fig. 3.10.C, are always seen exhibiting flat intensity profiles. Thus we envision bubble growth as occurring in roughly two stages. In the first, the bubble nucleates heterogeneously and grows on one substrate. Eventually, the bubble approaches the second substrate (Fig. 3.10.B), makes contact and symmetrically wets the top and bottom substrates. In the second, the bubble continues to grow in a top-bottom symmetric manner and travel to the wider parts of the tapered conduit. These stages require different theoretical treatments; the lattermost regime will be the focus of in the next two chapters.

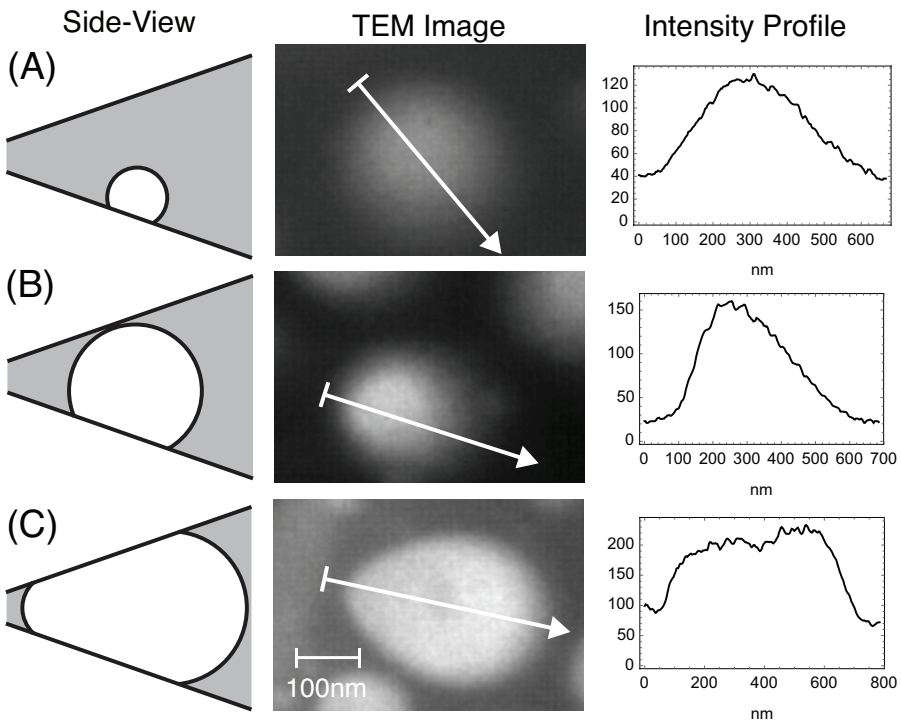

Fig. 3.10: Three characteristic bubbles at different stages in growth: A) a sessile bubble touching one surface, B) bubble beginning to bridge between membranes and C) a bubble touching both membranes and growing anisotropically due to confinement gradient. The columns are, respectively, from left to right: schematics of the side view, bright field TEM images, and intensity profiles taken along the principal axis.

3.5. "Sliding" Sphere Model

The established preferential growth and migration direction common to bubbles within a given region of the nanoaquarium, the fact that movement occurs only past a certain size, and the variable edge definition of the bubbles during motion suggest that observed dynamics are dominated by confinement gradients resulting from the either a bowed out or collapsed nanoaquarium. Given the extremely low Capillary ($10^{-9} - 10^{-7}$) and Bond ($10^{-11} - 10^{-9}$) numbers in our experiments, the bubble must have a nearly uniform curvature. Uniform curvature alone does not imply a spherical geometry.

However, since a sphere satisfies a uniform contact angle when intersecting a tapered conduit [82], such a case is considered briefly. A spherical bubble will appear blurrier on the edge facing the thicker part of the wedge since more of its surface protrudes; thus, a spherical geometry is qualitatively consistent with asymmetric intensity gradients noted earlier in micrographs Fig. 3.8 and Fig. 3.10. We note, however, that when the opening angle is very small, this feature may not be clearly observed. When a stationary bubble gains mass, its volume increases, which in turn would cause the bubble's contact angle to deviate from its equilibrium value, unless the bubble moves. We examine the hypothesis that a bubble migrates to preserve its equilibrium contact angle at all instances. The half-wedge height at the bubble's center $h \sim x\tan\varphi$, where x is the distance from the wedge cusp and $\varphi = \arctan\left(\left|\nabla h\right|\right)$ is the wedge half angle. We consider two simple bubble geometries: a bubble that bridges between the two wedge surfaces (Fig. 3.10.C) and a bubble growing on a single surface (Fig. 3.10.A).

When the bubble bridges, the following must be satisfied

$$R = h\frac{\cos\varphi}{\cos\theta_0} = x\frac{\sin\varphi}{\cos\theta_0}\ , \qquad [3.2]$$

where θ_0 is the contact angle and *h* is the channel half-height at the center of the sphere. For the contact angle to retain its equilibrium value when the bubble grows, we need

$$\dot{R}\cos\theta_0 = \dot{x}\sin\varphi\ . \qquad [3.3]$$

Not surprisingly, smaller slopes require larger velocities for the same $\dot{R}$ since the bubble must travel further to retain the magnitude of its contact angle. In the case of parallel

plates ($\varphi = 0$), the model becomes invalid because non-spherical geometries are needed to accommodate the growth. The velocity predicted by this model is not physically realizable since the model does not account for dynamics. It merely states how fast a spherical bubble must travel to retain its equilibrium contact angle.

When the bubble grows on a surface (without bridging), the sphere's center projected onto the wedge's plane of symmetry exhibits the apparent translational velocity

$$\dot{x} = \dot{R}\cos\theta_0 \sin\varphi . \qquad [3.4]$$

Fig. 3.11 depicts the velocity of the bubble's center of mass $\dot{x}$ as a function of the bubble growth $\dot{R}$. The symbols, solid lines, and dashed lines correspond, respectively, to experimental data (where we plot the rate of change of the hydraulic radius $R_H = \left(A/\pi\right)^{1/2}$ and A is the measured projected area), predictions for the bridging bubble eqn. [3.3] (solid lines), and predictions for the surface bubble eqn. [3.4] (dashed lines). The various lines correspond to different wedge angles. The bridging spherical bubble model overestimates while the surface bubble model underestimates the measured velocities. The large symbols correspond to two specific bubbles that were continuously monitored over time.

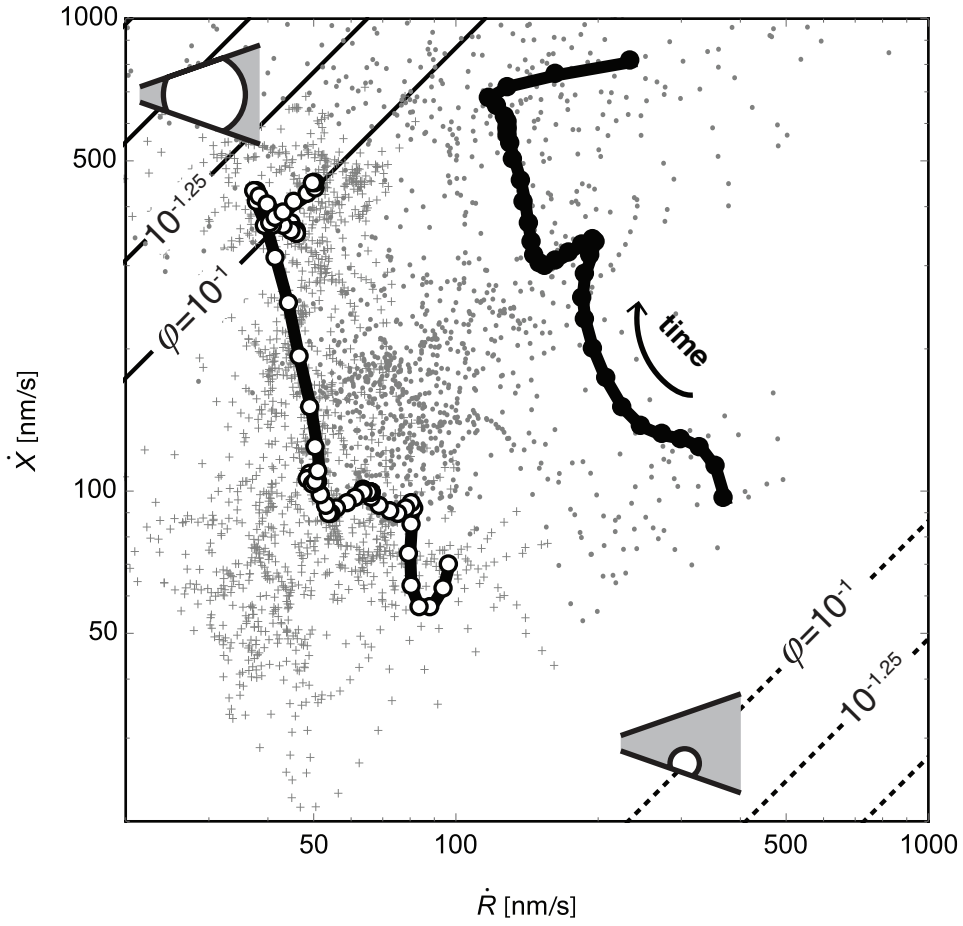

Fig. 3.11: Translational velocity $\dot{x}$ as a function of growth rate of the hydraulic radius $\dot{R}$ for bubbles observed at 10,000x (gray "+") and 5,000x (gray dots) magnifications. A bubble at each magnification is hilighted (connected points) along with its moving average trajectory in $\{\dot{R},\dot{x}\}$ space. Solid and dashed lines are, respectively, eqn. [3.3] (Fig. 3.10.C) and eqn. [3.4] (Fig. 3.10.A). $\theta_0 = 45^\circ$. $\varphi = 10^{-1}, 10^{-1.25}, 10^{-1.5} \cdots$.

The poor agreement between this simple model and the experimental data is very informative. The lack of proportionality between $\dot{x}$ and $\dot{R}$ indicates that the observed bubbles are not spherical and do not transport with constant contact angle. Similarly, the disagreement tells us that the bubbles are not moving as fast as they "need" to in order for their contact lines to be at equilibrium. We expect the slopes in the liquid cell to be small, but the agreement in Fig. 3.11 gets worse as slopes get smaller. Further, in the

experiment the bubbles tend to evolve towards higher velocities for similar growth rates as time goes on; since the model possesses no explicit time dependence, it cannot account for this feature either. One could conclude from Fig. 3.11 that bubbles are simply moving from regions of high-slope to low-slope. This is consistent with the direction of migration (bubbles are moving towards the center of the device where the slope is zero). However, this would require slopes to change rapidly within the viewing area (1-2 microns), and thus require large curvatures. The goal of the next chapter will be to determine the physics relevant to this problem.

3.6. Growth Anisotropy Revisited

As the bubble grows to contact both windows, there is a possibility that the bubble will be partially pinned to its nucleation site, which possesses either a chemical or physical defect (or both); contact lines of a representative bubble before and after departure are shown in Fig. 3.12 (the higher the transparency of the contact line, the earlier the time). Fig. 3.13 provides additional information on the bubble dynamics by examining the nucleation site, which repeatedly produced highly deformed bubbles; the figurereports the velocity of the center of mass as a function of the bubbles' projected hydraulic radius R_H (A) and as a function of the aspect ratio of a bounding ellipse (B). The symbols represent experimental data. In Fig. 3.13.B, the symbol's size is proportional to the bubble's radius. Since the data is noisy, we added solid lines (red) for guidance. When the bubble's radius is smaller than a critical radius $R_C \sim 110$ nm , the velocity of the bubble's center of mass increases slowly with the radius. Once the

bubble's radius exceeds R_C, the velocity of the bubble's center of mass increases rapidly as the radius increases. We hypothesize that small bubbles ($R_H < R_C$) are partially pinned but ask whether or not forces at the contact line inhibiting motion are enough to achieve the observed geometries or if complete immobility of part of the contact line is required. This is addressed in the next chapter by comparing model results for the case when both contact lines are free to move at the Blake-Haynes velocity and when the rear contact line is immobilized (pinned). As the bubble grows ($R_H < R_C$), it attains a teardrop shape and its aspect ratio increases. Once the bubble radius exceeds R_C and the bubble's aspect ratio exceeds ~1.3, the bubble departs, and its aspect ratio decreases. Furthermore, while bubbles acquire geometries like those observed in the tapered Hele-Shaw microfluidic device of Dangla *et al.* [83], it is unclear whether the departure is due to bubble breakup because of an instability[83] or if the entire bubble is released because a critical contact angle has been achieved at the rear portion of the contact line.

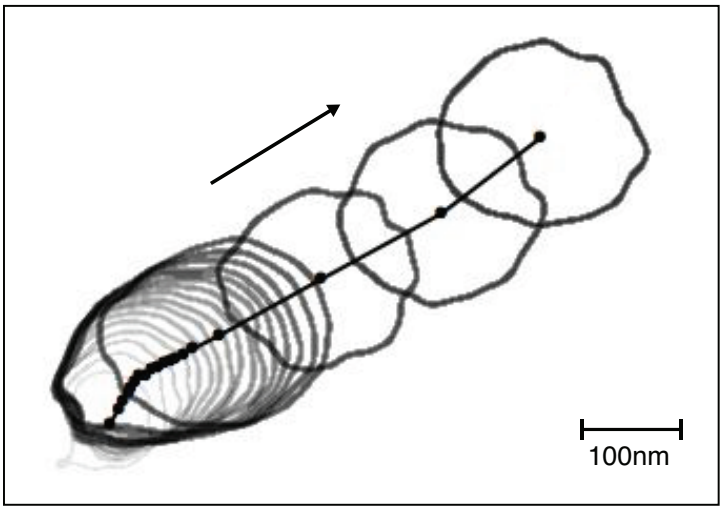

Fig. 3.12: Contact-line and centroid evolution of a bubble that nucleated in the field view. At early times the bubble grows while the position of the rear portion of the contact line changes very little; the last several frames show a sudden change in behavior. To show the passage of time, early profiles are plotted with more transparency. $\Delta t = 1/15$ s .

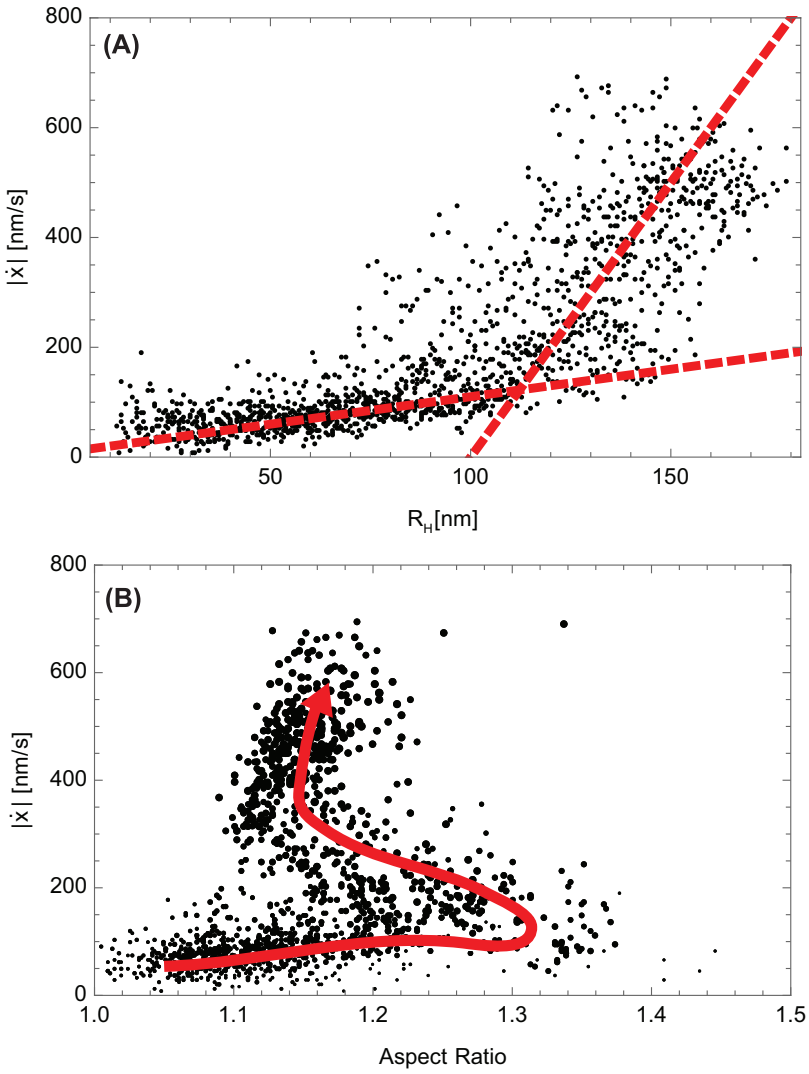

Fig. 3.13: Measured translational velocity (symbols) as a function of (A) bubble's hydraulic radius and (B) as a function of aspect ratio. N=23. Data symbol's size is proportional to the hydraulic radius. The solid lines in (A) correspond to $\dot{x} \sim R_H$ and $\dot{x} \sim 10R_H$. Solid arrow in (B) indicates the passage of time.

Chapter 4. Bubble Growth in Hele-Shaw Devices

4.1. Motivation

Understanding phenomena associated with bubbles and droplets growing and moving in a liquid cell relies on multiple pools of knowledge. In order to model the growth of the sub-micron bubbles described in the previous chapter, modifications to classical theories need to be considered. In the following analysis, the growth dynamics of a compressible, soluble bubble due to mass transfer in a super-saturated solution while it is confined between two divergent plates is considered. The gaseous bubble is composed of species that are produced by radiolysis of the surrounding fluid (water)[15], [72]; for simplicity it will be assumed that radiolysis maintains a steady far field concentration and that Hydrogen is the main contributor to growth.

The analysis will begin with a review of classical mass transfer driven growth theory that includes inertial and viscous forces[18], [19], [21]. Several assumptions are made at the onset such as neglecting the flow field within the bubble itself and dynamics slow enough to warrant isothermal expansion. This is in contrast to phase change phenomena such as cavitation in which rapid bubble growth and collapse would more closely be described by adiabatic or polytropic processes. Experimentally observed growth rates are used to generate a time scale, and scale the governing equations. The result justifies the assumption of quasi-static mass transfer, and negligible inertia and viscous stress contributions to bubble pressure, and prompts a closer look at the fluid dynamics specific to confined bubbles.

The transport and geometry of droplets and bubbles in confined geometries have attracted considerable attention in the scientific community. G. I. Taylor, Tanveer and Saffman studied the migration and interfacial instability of droplets in Hele-Shaw cells [84], [85]. Bretherton used matched asymptotic expansions to understand the geometry of the liquid-gas interface at the advancing and trailing edges of a gas slug in a cylindrical tube [8]. Park and Homsy extended Bretherton's theory to model advancing, weakly non-uniform interfaces in Hele-Shaw geometries[7].

Typically, bulk flow and/or buoyancy provoke bubble/drop motion. However, when the disperse phase only partially wets the substrate, gradients in substrate elasticity [86] and surface chemistry [87], [88] also spontaneously drive motion on single-substrates. Similarly, geometric gradients can promote transport of drops inside tapered capillaries [89], [90] and on conical wires [41], [91]. To minimize their surface energy, wetting drops seek confinement while non-wetting drops and bubbles avoid it. The dynamics of bubbles and droplets in tapered Hele-Shaw devices when the continuous phase wets *completely* the substrates [83], [92], [93] or when a film between the disperse phase and substrate exists [94] have been considered as well. In the cases considered by Metz *et al.* [92] , Reyssat [93] and Jenson [94], drops and/or bubbles are dispensed into a tapered channel and traverse towards their equilibrium positions where they can exist as spherical sections that satisfy the equilibrium contact angle [82] or be completely free floating droplets/bubbles.

Metz *et al.* [22] modeled the propulsive driving force by estimating a fore-aft capillary pressure difference and balancing it against dissipative mechanisms in the bulk and at the contact line. To circumvent the problem of modeling the precise geometry of

the bubble, only the component of the curvature in the confinement direction is considered (*i.e.*, for two plates separated by a gap of 2*h,* the curvature would be *1/h)*. In contrast, Reyssat estimates the propulsive force by taking the spatial gradient of the surface energy of the system (assuming constant volume) and balances it against bulk viscous dissipation and a Bretheron-like drag law developed by Cantat[95]. Jenson et al. [94] performed microgravity experiments at larger length scales and identified flow regimes dominated by capillary forces, inertia, and viscous forces; however, the specifics of the contact line were not considered.

The migrating bubbles described in Chapter 3 range in size from tens to hundreds of nm. Since the water wets the silicon nitride, bubbles migrate towards the wider part of the taper as expected to minimize surface energy; however, energy considerations alone do not allow one to estimate bubbles' velocities and dynamically created shapes. Scaling analysis suggests that the observed bubble migration and geometry cannot be explained by buoyancy and capillary force-based theories since both growth and migration take place at very small Capillary ($10^{-9} - 10^{-7}$) and Bond ($10^{-11} - 10^{-9}$) numbers. Our experimental situation differs in three important ways from prior works. Firstly, since the Capillary numbers of our experiments are much lower than those encountered in the cited works and our surface does not perfectly wet the substrate, we cannot presume the existence of a liquid lubrication layer between the bubble and substrate. Secondly, the volume and mass of our bubbles are changing with time. Lastly, since the mass transport into our bubbles is ostensibly driven by diffusion, it is proportional to the pressure within the bubbles, which at the sub-micron scale is sensitively related to the bubble curvature, $\propto R^{-1}$.

The ultra-low capillary number at which our bubbles grow and move suggests that the dynamics progresses through uniform-mean curvature conformations, thus we posit that bubbles in our experiment move only because they are growing. The statics of capillary surfaces confined between two parallel plates or in a wedge has also been considered extensively. When plates are parallel, interfaces can assume axisymmetric shapes that satisfy constant contact angle and volumetric constraints. These interfaces are described by elliptical integrals and can be classified as either nodoidal, unduloidal or catenoidal [82]; special cases can result in cylindrical and spherical shapes. However, it has been shown that if the planes are tilted infinitesimally, equilibrium can be lost entirely unless the wedge angle 2φ and equilibrium contact angle θ_0 (measured from within the continuous phase) satisfy the inequality $\theta_0 - \pi/2 < \varphi$. When this inequality is satisfied and $\varphi \neq 0$, a section of a sphere is the equilibrium surface [82], [96], this fact was used earlier to help sort the data in Chapter 3.

For the bubble to move in the absence of Laplace-pressure-gradients, however, the driving force must arise at the contact line itself through the unbalanced Young's force $f \sim \gamma\left(\cos\theta - \cos\theta_0\right)$, where θ is the instantaneous contact angle [12], [97], [98]. We consider a system for which the gas-liquid interface is always at mechanical equilibrium while the contact angle is driven out of equilibrium by mass transfer.

The dominance of contact line dynamics at ultra-low Capillary numbers is also encountered in a slightly different system, the adsorption of colloidal particles to interfaces [99]. Unlike prior works[92]-[94], in the present model we leverage the limit $Ca \to 0$ to explicitly couple contact angle and radius of curvature. This motivates us to develop a model that explicitly describes the contact angle and radius of curvature

evolution. For simplicity we begin with a two-dimensional analysis and qualitatively compare our theoretical predictions with what we have observed in experiments.

4.2. Governing Equations and Scaling

Before we consider the contact line physics specific to the nanobubble problem, the problem of a growing bubble in an infinite medium is briefly reviewed. In the classical Rayleigh-Plesset bubble growth problem, analysis begins with mass and momentum conservation. The radial flow field generated by a spherical bubble's moving interface is given by the potential flow

$$u(r,t) = \frac{R^2}{r^2}\dot{R}\,, \qquad [4.1]$$

where it has been assumed that mass transfer at the interface is negligible. This is reasonable even in phase change phenomena (boiling and cavitation) so long as the densities of the two phases are sufficiently disparate. The Navier-Stokes equation for a spherically symmetric flow is given by

$$\rho_L\left(\frac{\partial u}{\partial t} + u\frac{\partial u}{\partial r}\right) = -\frac{\partial P}{\partial r} + \mu\left[\frac{1}{r^2}\frac{\partial}{\partial r}\left(r^2\frac{\partial u}{\partial r}\right) - \frac{2u}{r^2}\right]. \qquad [4.2]$$

Since the flow is irrotational, viscous terms drop upon substituting in [4.1], simplifying to

$$-\frac{\partial P}{\partial r}\frac{1}{\rho_L} = 2\frac{R^4}{r^5}\dot{R}^2 - \frac{1}{r^2}\left(R^2\ddot{R} + 2R\dot{R}^2\right). \qquad [4.3]$$

The expression can readily be integrated to remove the radial dependence

$$\frac{P(R)-P_\infty}{\rho_L}=\left(-\frac{1}{2}\frac{R^4}{r^4}\dot{R}^2+\frac{1}{r}\left(R^2\ddot{R}+2R\dot{R}^2\right)\right)\Bigg|_R^\infty . \qquad [4.4]$$

After some rearrangement we have an equation for the pressure directly outside the bubble as a function of the bubble radius, radial growth rate, and acceleration

$$\frac{P(R)-P_\infty}{\rho_L}=R\ddot{R}+\frac{3}{2}\dot{R}^2 . \qquad [4.5]$$

The pressure inside the bubble P_B can replace the pressure directly outside of the bubble $P(r=R)$ by performing a force balance on a portion of the interface. In spherical coordinates the component of the stress tensor we are interested in is given by

$$\sigma_{rr}=2\mu\frac{\partial u}{\partial r}-P . \qquad [4.6]$$

At the interface, we have the following jump condition due to the curvature of the bubble's interface:

$$\sigma_{rr,outside}-\sigma_{rr,inside}=\frac{2\gamma}{R} \qquad [4.7]$$

$$\left(2\mu\frac{\partial u}{\partial r}-P\right)\Bigg|_{outside}-\left(2\mu\frac{\partial u}{\partial r}-P\right)\Bigg|_{inside}=\frac{2\gamma}{R} \qquad [4.8]$$

Since $\mu_{H_2O_2}\ll\mu_{H_2O}$, the pressure directly outside of the bubble is given by

$$P(R)=P_B-\frac{2\gamma}{R}+2\mu\frac{\partial u}{\partial r}=P_B-\frac{2\gamma}{R}-4\mu\frac{R^2}{r^3}\dot{R} . \qquad [4.9]$$

Applying this boundary condition yields a second order ODE for the bubble radius:

$$P_B = \rho_L\left(R\ddot{R} + \frac{3}{2}\dot{R}^2\right) + \frac{2\gamma}{R} + 4\mu\frac{R^2}{r^3}\dot{R} + P_\infty . \qquad [4.10]$$

Since this equation depends on the pressure inside the bubble, we need another equation to describe the thermodynamic state of the gas. Assuming that the gas(es) within the bubble are incondensable we have from the ideal gas law that the number of moles in the bubble

$$N = \frac{P_B V}{BT} = \frac{4\pi}{3}\frac{R^3 P_B}{BT} . \qquad [4.11]$$

In the above, B is the universal gas constant and T the absolute temperature. Taking the time derivative (and assuming isothermal expansion) yields the rate of change of the number of molecules within the bubble:

$$\dot{N} = \frac{4\pi}{3BT}\left(3R^2\dot{R}P_B + R^3\dot{P}_B\right) . \qquad [4.12]$$

The total flux supplied to the bubble through diffusion is given by:

$$\dot{N} = 4\pi R^2 D\frac{\partial C}{\partial r} . \qquad [4.13]$$

Note that there is no direct contribution from convection in this flux term; this is true so long as the interface and bulk fluid move at the same velocity. Equating these two equations yields a first order ODE for the pressure of the bubble that must be solved simultaneously with the momentum equation, [4.10].

$$4\pi R^2 D\frac{\partial C}{\partial r} = \frac{4\pi}{3BT}\left(3R^2\dot{R}P_B + R^3\dot{P}_B\right) . \qquad [4.14]$$

To close the problem, an expression of the mass flux is needed. The task is complicated by the moving boundary of the interface and the changing concentration at the surface of the bubble, since $C\left(r=R\right)\propto P_B$. Beginning with the unsteady diffusion equation

$$\frac{\partial C}{\partial t}+v_r\frac{\partial C}{\partial r}=D\frac{1}{r^2}\frac{\partial}{\partial r}\left(r^2\frac{\partial C}{\partial r}\right), \qquad [4.15]$$

we can introduce the variable transformation $u=C-C\left(R\right)$,

$$\frac{\partial u}{\partial t}+\frac{\partial C_s}{\partial t}+v_r\frac{\partial u}{\partial r}=D\frac{1}{r^2}\frac{\partial}{\partial r}\left(r^2\frac{\partial u}{\partial r}\right) \text{ with } C\left(R\right)=H\left(P_\infty+\frac{2\gamma}{R}\right), \qquad [4.16]$$

where *H* the Henry's constant for the solute of interest. Of course, this would not be a practical transformation to effectuate a solution since it simply moves the problematic boundary condition at $r=R$ to $r\to\infty$, however, it will allow us to compare the size of various terms.

$$\frac{\partial u}{\partial t}-\frac{H\gamma}{R^2}\frac{\partial R}{\partial t}+v_r\frac{\partial u}{\partial r}=D\frac{1}{r^2}\frac{\partial}{\partial r}\left(r^2\frac{\partial u}{\partial r}\right). \qquad [4.17]$$

Let's now non-dimensionalize the system according to $r^*=r/R_0$, $t^*=t\dot{R}_0/R_0$, and $u^*=u/C_\infty$ where R_0 is a characteristic bubble radius and $\dot{R}_0$ is a characteristic velocity of the interface. The governing equations alone do not furnish us with a timescale different than the one associated with diffusion. However, we choose to use an arbitrary interface velocity so that we can gain insights into the observed experimental situation that we hypothesize possess additional physics. Introducing these scales and simplifying yields

$$Pe\left(\frac{\partial u^*}{\partial t^*}+v_r^*\frac{\partial u^*}{\partial r^*}\right)-\Omega_3\frac{1}{R^2}\frac{\partial R^*}{\partial t^*}=\frac{1}{r^{*2}}\frac{\partial}{\partial r^*}\left(r^{*2}\frac{\partial u^*}{\partial r^*}\right). \quad [4.18]$$

and gives rise to two dimensionless groups. The familiar Peclet number and another that quantifies the importance of boundary condition transience

$$Pe=\frac{\dot{R}_0R_0}{D} \text{ and } \Omega_3=\frac{H\gamma\dot{R}_0}{DC_\infty}. \quad [4.19]$$

When these quantities are much less than one then using the flux from the steady diffusion equation is justified. Using the following values $H=7.74\times10^{-6}[\text{mol/m}^3\text{Pa}]$, $D=4.5\times10^{-9}[\text{m}^2/s]$, $R_0\sim10^{-8}[\text{m}]$, $\dot{R}_0\sim10^{-7}[\text{m/s}]$, $\gamma\sim40\times10^{-3}[\text{J/m}^2]$, and letting the far field concentration scale as the initial surface concentration of the bubble $C_\infty\sim H\gamma/R_0$ such that $\Omega_3=R_0\dot{R}_0/D=\text{Pe}$ gives $\text{Pe}\sim10^{-8}\ll1$ and eqn. [4.18] simplifies to

$$0=\frac{1}{r^{*2}}\frac{\partial}{\partial r^*}\left(r^{*2}\frac{\partial u^*}{\partial r^*}\right). \quad [4.20]$$

Applying these same scales to [4.10] gives

$$P_B^*=\text{We}\left(R^*\ddot{R}^*+\frac{3}{2}\dot{R}^{*2}\right)+\frac{2\gamma}{R^*}+\text{Ca}4\frac{\dot{R}^*}{R^*}+P_\infty^*, \quad [4.21]$$

where the Weber and Capillary numbers naturally arise

$$\text{We}=\frac{\rho\dot{R}_0^2R}{\gamma} \text{ and } \text{Ca}=\frac{\mu\dot{R}_0}{\gamma}, \quad [4.22]$$

and are both much less than one. With $\text{We, Ca}\ll0$, eqn. [4.21] becomes simply

$$P_B^*=\frac{2\gamma}{R^*}. \quad [4.23]$$

The conclusion of this dimensional analysis is that a quasi-static analysis is suitable for bubbles growing and/or moving at the rates described in the previous chapter. The scaling also shows that inertial and viscous forces can be safely omitted. However, since we plugged in experimentally observed velocities to generate the time scale, the scaling analysis cannot furnish us with *why* bubbles grow the way they do. The task of the next section is to establish the importance of additional physics at the contact line.

4.3. Contact Line Dissipation

The previous scaling served to establish that quasi-static mass transfer is a valid approximation, which will be utilized below. Taking a closer look at dissipation mechanisms in our system, we find four contributors: viscous dissipation in the bubble interior, viscous dissipation in the bulk fluid surrounding the bubble (while this was ruled out for a bubble in an infinite medium, we briefly reconsider it here for a bubble in a Hele-Shaw device), fluid circulation in the vicinity of the contact line [10], [100], and the movement of the contact line itself [11], [12]. We may safely ignore the dissipation within the bubble itself because of the large viscosity contrast between the gas and the liquid. The bulk viscous dissipation of a bubble of $R \sim 100$ nm translating at $U \sim 1\ \mu\text{m/s}$ (the maximum velocity we observe experimentally) in water confined within a Hele-Shaw cell of half-height $h \sim 100$ nm scales as $\eta (U/2h)^2 R^2 2h \sim 10^{-23}$ J/s[101]. There is often debate over which of the final two mechanisms dominate in a given scenario. For a spreading spherical droplet, the de Gennes model for hydrodynamic dissipation in the

vicinity of the contact line yields $\sim 6\pi U^2 \ln\left(R/R^*\right) R/\theta_D \sim 10^{-21} - 10^{-20}$ J/s, where θ_D is the dynamic contact angle ($\theta_D = \theta_0 = 30^\circ$ is assumed for the purposes of the estimate) and $R^* \sim 0.1$ nm is the molecular cutoff length [9]. Alternatively, the Blake-Haynes-Eyring approach for molecular contact line dissipation gives $2\pi R U^2 \eta_{CL} \sim 10^{-21} - 10^{-17}$ J/s, where $\eta_{CL} = k_B T / \left(\lambda^3 \kappa_0\right)$ is the contact line viscosity ([Pa s]). The characteristic length $\lambda \sim 0.1$ nm is the atomic lattice spacing of the substrate and the hopping frequency $\kappa_0 \sim 10^3 - 10^9$ s^{-1} [11]. The dominance of one dissipation mechanism over the other will therefore depend strongly on these two unknown parameters. We focus on the Blake-Haynes model because it affords greater flexibility since it is not tied directly to the bulk viscosity and can include, for example, the effect of surfactants on adsorption kinetics [14].

4.4. 2D Cylindrical Bubble Growing in a Wedge Model

To explore the impact of contact line resistance on bubble motion, a 2D model is proposed. Fig. 4.1 depicts the bubble's cross-section and defines the relevant geometric parameters. We seek the time evolution of the contact line positions $x_\pm$, contact angles $\theta_\pm$, and the radius of curvature *R*. Subscripts + and – denote, respectively, variables associated with the interfaces facing the wide (right) part and the narrow (left) part of the conduit. Since water does not completely wet silicon nitride and the observed interfacial

velocities are well below the threshold required to support a film, we assume that the bubble contacts the surfaces. The absence of a liquid film between the bubble and the surface is consistent with Bretherton's theory that predicts a film thickness $d \propto h\mathrm{Ca}^{2/3}$, where $\mathrm{Ca}=\mathrm{U}\eta/\gamma$ is the capillary number. When $\gamma \sim 4\times10^{-2}$ N/m (water surface tension in the presence of a surfactant), $U \sim 10^{-6}$ m/s, $\eta = 8.9\times10^{-4}$ Pa s (water), and $h \sim 100$ nm, Bretherton's theory predicts $d \sim 10^{-13}$ m, which is non-physically small.

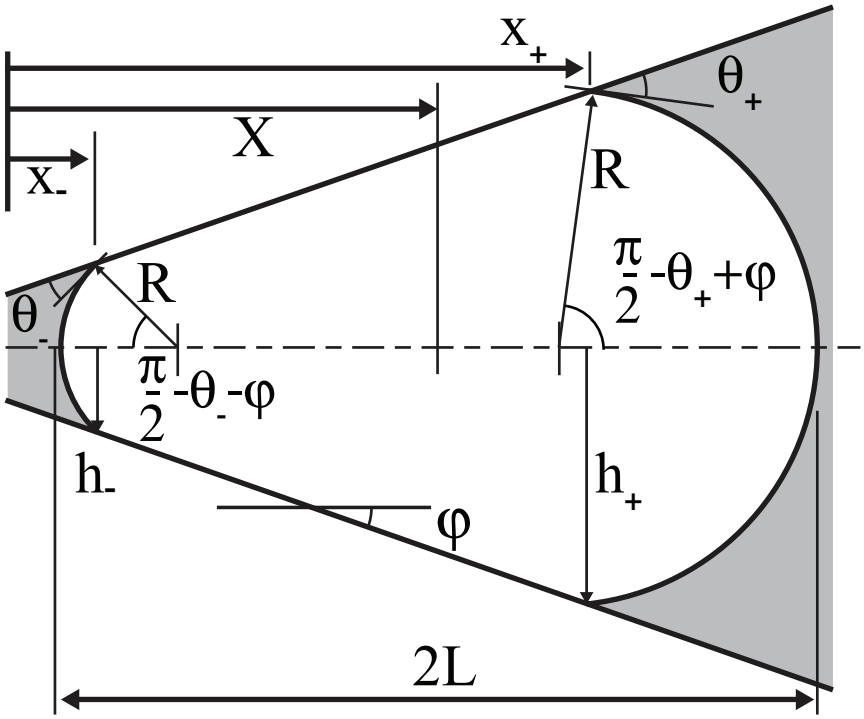

Fig. 4.1: Schematic of 2D bubble slug showing contact line positions $x_{\pm}$, contact angles $\theta_{\pm}$, local channel half-height $h_{\pm}$, radius of curvature *R*, half-length *L*, and center position *X* with exaggerated taper φ.

Proceeding with the Blake-Haynes model, the projection of the contact line velocity on the wedge symmetry plane

$$\dot{x}_{\pm} = \pm U_0 \sigma\left(\theta_{\pm}\right) \cos\varphi \sinh\left[W_0\left(\cos\theta_{\pm} - \cos\theta_0\right)\right], \qquad [4.24]$$

with

$$\sigma\left(\theta_{\pm}\right) = \begin{cases} 1 & \theta_{\pm}/\theta_0 \le \beta_R \\ 0 & \beta_R < \theta_{\pm}/\theta_0 < \beta_A \\ 1 & \theta_{\pm}/\theta_0 \ge \beta_A \end{cases} \qquad [4.25]$$

In the above, $W_0 = \lambda^2\gamma/\left(2k_BT\right)$ is the normalized energy barrier that needs to be surmounted to move the contact line by a characteristic distance λ (typically the lattice spacing of the substrate) [12]. $U_0 = 2\kappa_0\lambda$ is the molecular velocity scale with the hopping frequency κ_0. θ_0 is the equilibrium contact angle. To explore deviations from smooth behavior, we introduce the function $\sigma\left(\theta_{\pm}\right)$ to include hysteresis, which are controlled by changing the values $\beta_{A,R}$. Subscripts *A* and *R* correspond, respectively, to advancing and receding contact angles $\beta_A \ge 1$ and $\beta_R \le 1$ (note, by convention advancing and receding refer to movement of the liquid phase; when liquid has moved into an area previously occupied by the bubble that contact line is said to have advanced and *vice versa*). Blake-Haynes behavior can be retrieved by letting $\beta_{A,R} = 1$. For simplicity, we assume a small W_0 and linearize eqn. [4.24] for small deviations from the equilibrium contact angle to yield

$$\dot{x}_{\pm} = \pm \frac{\gamma}{\eta_{CL}} \sigma\left(\theta_{\pm}\right)\left(\cos\theta_{\pm} - \cos\theta_0\right)\cos\varphi\,, \qquad [4.26]$$

where γ is the macroscopic surface tension and $\eta_{CL} = k_B T / \left(\kappa_0 \lambda^3\right)$ is the contact line viscosity.

The half-heights of the channel at the contact line positions are

$$h_{\pm} = R\cos\left(\theta_{\pm} \mp \varphi\right). \qquad [4.27]$$

We assume that the bubble is at a uniform pressure and therefore has a uniform radius of curvature R. Initially, we take the bubble to be shaped like a segment of a circular disk with equilibrium contact angles. $h_{\pm}\left(t=0\right) = R_0\cos\left(\theta_0 \mp \varphi\right)$. Where,

$$\frac{R_0}{h_0} = \frac{\cos\varphi}{\cos\theta_0} \qquad [4.28]$$

defines the relationship between the initial radius R_0 and conduit half height at the initial disk's center h_0. In what follows, the origin of x is fixed at the position of the center of the initial bubble. Eqn. [4.27] , the relationships $h_{\pm} = h_0 + x_{\pm}\tan\varphi$, and the uniform curvature condition yield the two equations:

$$R = \frac{h_0 + x_{-}\tan\varphi}{\cos\left(\theta_{-} + \varphi\right)} = \frac{h_0 + x_{+}\tan\varphi}{\cos\left(\theta_{+} - \varphi\right)}\,. \qquad [4.29]$$

It is convenient to express the bubble size in terms of its length $2L$ along the wedge axis

$$2L=\left(x_{+}-x_{-}\right)+R\left[2-\sin\left(\theta_{-}+\varphi\right)-\sin\left(\theta_{+}-\varphi\right)\right]. \qquad [4.30]$$

At $t=0$, $L=R$. The location of the bubble's geometric center

$$X=\frac{1}{2}\left(x_{-}+x_{+}+R\left[\sin\left(\theta_{-}+\varphi\right)-\sin\left(\theta_{+}-\varphi\right)\right]\right). \qquad [4.31]$$

We examine the motion induced by mass transfer into the bubble. We assume that the gas in the bubble behaves like an ideal gas $PV=nBT$, where P is the uniform pressure in the bubble, *n* is the number of moles per unit depth, B is the universal gas constant, and T is the absolute temperature. Given the very high Laplace pressure of the bubble, deviations from ideal gas behavior are expected, but not considered to avoid obscuring the goal of the model. The time derivative of the state equation yields

$$\dot{P}V+P\dot{V}=\dot{n}BT. \qquad [4.32]$$

The volume per unit depth is:

$$V=\frac{R^2}{2}\begin{bmatrix}2\pi-2\left(\theta_{-}+\theta_{+}\right)\\-\sin\left(2\theta_{-}+2\varphi\right)-\sin\left(2\theta_{+}-2\varphi\right)\end{bmatrix}+\left[2h_0+\left(x_{-}+x_{+}\right)\tan\varphi\right]\left(x_{+}-x_{-}\right). \qquad [4.33]$$

We assume quasi-static conditions with the pressure in the bubble given by Laplace equation $P_\infty + 2\gamma / R$, where P_∞ is the liquid's pressure, and that the bubble's volume increase does not appreciably alter the liquid pressure. The solute gas concentration at the liquid's interface with the bubble obeys Henry's law $C\left(r = R\right) = HP$, where *H* is Henry's constant. For simplicity, we assume that the solute concentration $C_\infty = C\left(r = R_\infty\right)$ at the distance R_∞ from the bubble's center is held constant at all times. This assumption is reasonable when the bubble's volume is much smaller than the liquid's volume and/or when solute is continuously produced to maintain its equilibrium concentration as during electron beam irradiation [15]. The total solute mass flow per unit depth is:

$$\dot{n} = 2\left(\pi - \theta_- - \theta_+\right)\frac{D\left[C_\infty - H\left(P_\infty + \gamma / R\right)\right]}{\ln\left(R / R_\infty\right)}\ , \qquad [4.34]$$

where *D* is the solute diffusivity. Substituting eqn. [4.34] into [4.32] along with the constraint eqns. [4.29] and the Blake-Haynes eqn. [4.26] gives the mass transfer driven system. We define the excess solute concentration as

$$\alpha = \log_{10}\left(\frac{C_\infty}{C_0} - 1\right), \qquad [4.35]$$

where $C_0 = H\left(P_\infty + \gamma / R_0\right)$ such that $C_\infty = H\left(10^\alpha + 1\right)\left(P_\infty + \gamma / R_0\right)$. We choose this definition for the far field concentration so that we can readily control it relative to what is needed to initiate growth $C_\infty > C_0$. Given C_∞ and initial conditions, the equations can be integrated to yield R, $\theta_\pm$, and $x_\pm$ as functions of time.

For comparison, if we assume $\eta_{CL} = 0$ and $\theta_{\pm} = \theta_0$. We have an Epstein-Plesset-like theory. In this case, the pressure remains the same, but volume per unit depth is given by

$$V_{EP} = \pi R^2 \left[1 - 2\left(\frac{\theta_0}{2} - \sin\left(\frac{\theta_0}{2} \right) \right) \right] \qquad [4.36]$$

and the mass flow per unit depth becomes

$$\dot{n}_{EP} = 2\left(\pi - 2\theta_0\right) \frac{D\left[C_\infty - H\left(P_\infty + \gamma / R \right) \right]}{\ln\left(R / R_\infty \right)} \qquad [4.37]$$

.

4.4.1. Volume Driven Growth Results

We now examine the dynamics of the system in response to a prescribed volume (per unit depth) variations with time. Thus we set $V\left(t\right) \sim V_0 t^2$ in eqn. [4.33]. Serendipitously, this choice of volume evolution permits the existence of a steady-dynamic state (constant velocity $\dot{X}$ and growth rate $\dot{L}$). This allows us to qualitatively examine the transient effects of initial conditions, wedge angle, and equilibrium contact angle. We non-dimensionalize the system using the length scale h_0 and timescale $h_0 \eta_{CL} / \gamma$. Thus, the dimensionless volume flow $V_0^* = V_0 \eta_{CL} / \left(\gamma h_0 \right)$, equilibrium contact angle θ_0, slope φ and the initial conditions govern the evolution of the system.

Fig. 4.2 (A) and (B) shows, respectively, the effect of V_0^* and φ on the evolution of $\theta_{\pm}$ and R in time. In the long time, we observe that the trailing (leading) contact

angle is greater (lesser) than the equilibrium contact angle. This is consistent with both interfaces moving to the right at the same velocity, towards the wider part of the wedge. At short times, however, both contact angles are observed to decrease below the equilibrium value. This corresponds to an outward expansion of the droplet. Interestingly, very short times, this is accommodated completely by a change in the radius of curvature, which must decrease initially (Fig. 4.3). Increasing V_0^* and φ have similar effects: a larger departure from equilibrium in the long time and a more pronounced non-monotonic evolution. Decreasing the slope also affects the time required for the rear contact line velocity to assume a positive value, this is shown in the inset of Fig. 4.2.A. As the slope becomes *smaller* the time spent growing outward in both directions *increases*.

Simply put, the response of the bubble occurs in two phases with a transition region in between: an expansion phase in early times and a phase where translation and growth coexist. In the limit $\mathrm{Ca} \to 0$, bulk viscous dissipation does not exist and therefore *decreasing* the radius of curvature is the path of least resistance to accommodate growth. In other words, these results show that physics at the contact line feed back into the global geometry of the bubble or droplet; this has important implications for any processes that depend on the internal pressure of the bubble. When the radius of curvature responds instantly in this way, both contact angles $\theta_{1,2}$ are forced to decrease below their equilibrium values. However, they do so asymmetrically $\theta_2 < \theta_1 < \theta_0$ and eventually the contact lines "cooperate" to allow for translation of the disperse phase.

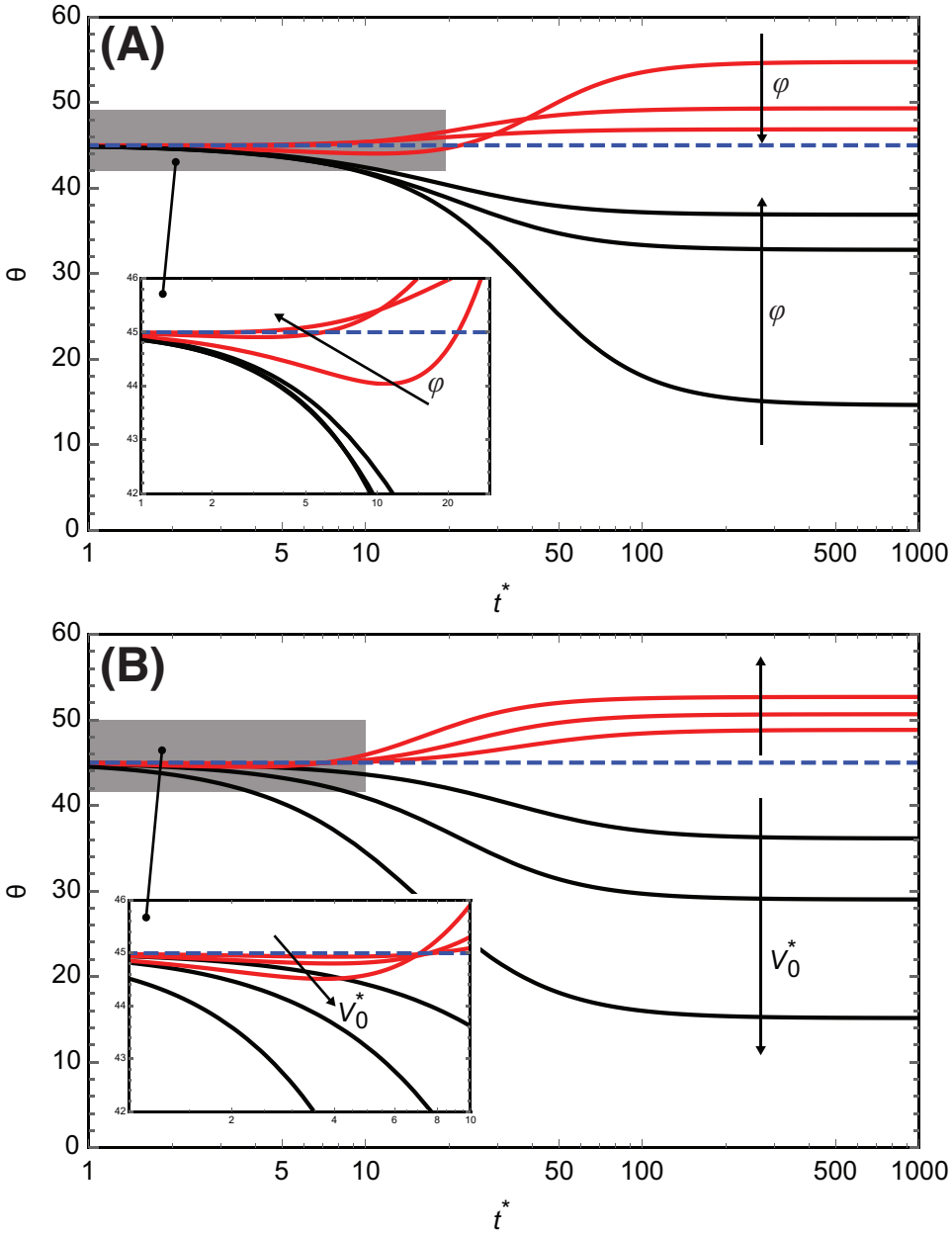

Fig. 4.2: θ_- (red) and θ_+ (black) contact angle evolution (A) when the wedge angle $\varphi = \{0.1, 0.3, 0.5, 0.7\}$ ($V_0^* = 0.004$ and $\theta_0 = 45^\circ$) and (B) when the area flux $V_0^* = \{0.001, 0.002, 0.01, 0.02\}$ ($\varphi = 0.25$ and $\theta_0 = 45^\circ$).

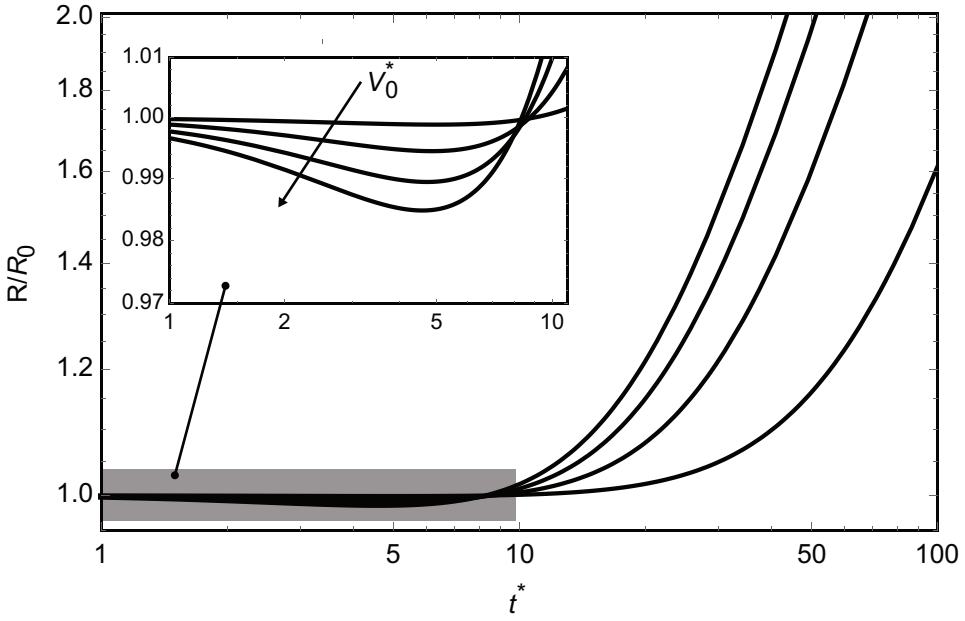

Fig. 4.3: Bubble radius of curvature normalized by starting radius as a function of time. $V_0^* = \{0.001, 0.002, 0.01, 0.02\}$. $\varphi = 0.25$ and $\theta_0 = 45^\circ$.

4.4.2. Mass Transfer Driven Growth Results

We now consider the more realistic case of mass transfer-controlled growth of the wedged bubble. Fig. 4.4 depicts the bubble's half-length L and radius R (A), the velocity of the bubble's center (B), , and the ratio *R/L* (C) as functions of time. Lines with symbols (▲, △, ●, ○), dashed lines, extra thick lines, and symbols correspond, respectively, to theoretical predictions, predictions for a pinned rear contact line, predictions based on Epstein-Plesset (EP) theory [20], and experimental data.

For comparison, we've selected data of bubbles that nucleate in the field of view and begin translating instead of bubbles that simply pass through the viewing window but have already grown to a large size. We found it instructive to include longer time predictions to highlight the differences between our theory and classical theories (i.e.,

EP) and demonstrate the asymptotic convergence of our theory to EP's theory at long time. In the theoretical calculations, we use $h_0 = 15$ nm, $\alpha = -4$, $\theta_0 = 30^\circ$ [102], P_∞ =0.1MPa, $H_{H_2} = 7.74 \times 10^{-6}$ mol/Pa m^3 [103], $D_{H_2} = 4.5 \times 10^{-9}$ m^2/s [104]and $\gamma = 40$ mN/m. The surface tension of the gas-liquid interface is lower than that of pure water to account for the presence of the CTAB surfactant. While the device is hermetically sealed, the flexibility of the membrane permits a range of pressures[70]; since we are unable to measure these deflections in-situ, we assume a pressure of one atmosphere.

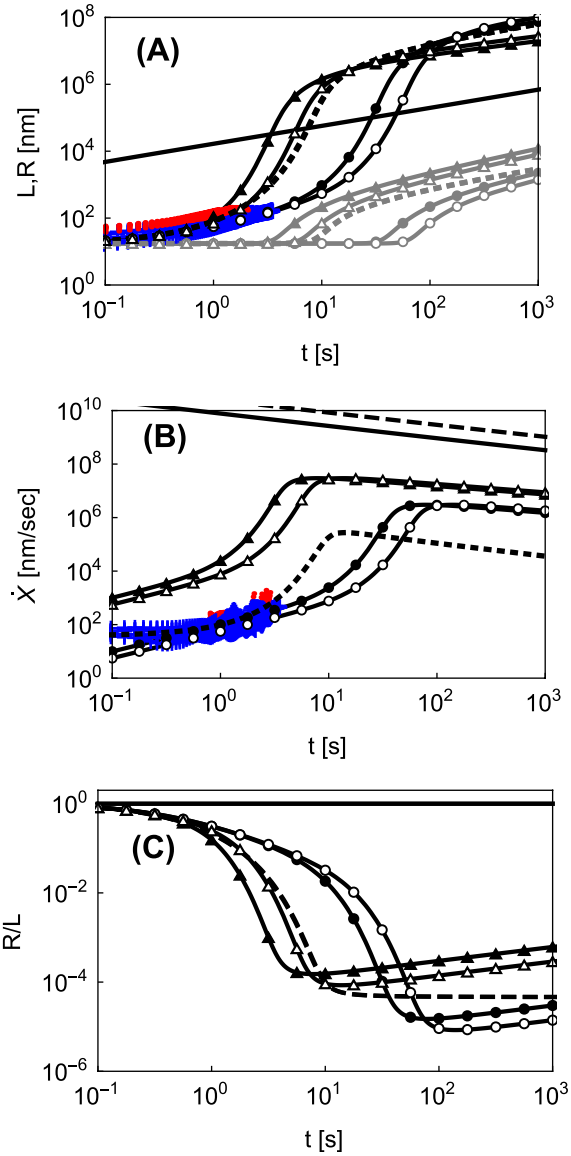

Fig. 4.4: Bubble half-length and radius (A), velocity (B), and ratio *R/L* (C) as functions of time. The blue "+" and red dots represent experimental data from, respectively, 10,000x and 5,000x observations. We plot four combinations of η_{CL} and φ: $\eta_{CL} = \eta_0\{10^1, 10^3\}$ are respectively, triangles and circles; and $\varphi = 10^{-6}, 10^{-6.25}$ are respectively solid and hollow symbols. Dashed lines correspond to $\eta_{CL,-} \to \infty$. Solid and dashed lines are Epstein-Plesset theory using eqn. [3.3] for the velocity with $\varphi = 10^{-6}$ and $10^{-6.25}$ (note that the growth rates are nearly identical while the velocities differ). In (B), black trends are the half-length *L* and gray trends are t he corresponding radius of curvature *R*. $\eta_0 = 8.9\times10^{-4}$ Pa s, $h_0 = 15$ nm, $\alpha = -4$, $\theta_0 = 30^\circ$, and $\gamma = 40$ mN/m.

To examine the sensitivity of our predictions to contact line viscosity and the wedge slope, we present predictions in Fig. 4.4 for $\eta_{CL} = \eta_0 \{10^1, 10^3\}$ (▲, △ and ●, ○), where $\eta_0 = 8.9 \times 10^{-4}$ Pa s and slopes $\varphi = 10^{-6}$ (▲, ●) and $10^{-6.25}$ (△, ○). Note that even small changes in the slope shift the curve noticeably. Decreasing the slope shifts the curves to the right because it increases the distance a bubble must travel to decrease its confinement. Bubbles eventually grow like EP theory predictions when they are large enough that contact line dynamics no longer dominate the geometry of the bubbles. That is, a small bubble must change its curvature much more than a large bubble in order to move and grow. The EP theory is applied to a wedged bubble undergoing diffusion-driven growth without contact line dissipation $\eta_{CL} \to 0$ (Supplement S5). In the latter case, the contact lines slide freely to maintain the equilibrium contact angle and equation [3.3] is used to find the translational velocity as a function of growth rate. We can understand the restricted growth through Fig. 4.5, which depicts $R/R_0 - 1$ (A) and $\theta_{\pm} - \theta_0$ (B) as functions of time when the supersaturation $\alpha = -2, -3$ and -4. Witness that at low super-saturation, the radius initially decreases slightly, suppressing mass transfer; attains a minimum and then increases again. The super-saturation level sets the magnitude of the dip because the surface concentration cannot exceed that of the bulk concentration. This type of behavior is absent in classical theories of bubble growth that tend to over-predict the rate of growth. As expected, as time increases, θ_+ increases while θ_- decreases. Unlike the free sliding case, smaller slopes result in small velocities because the growth is restricted by the inability to increase the radius of curvature. That

is, the contact line must move further for smaller slopes in order for the curvature to be permitted to decrease and growth to accelerate.

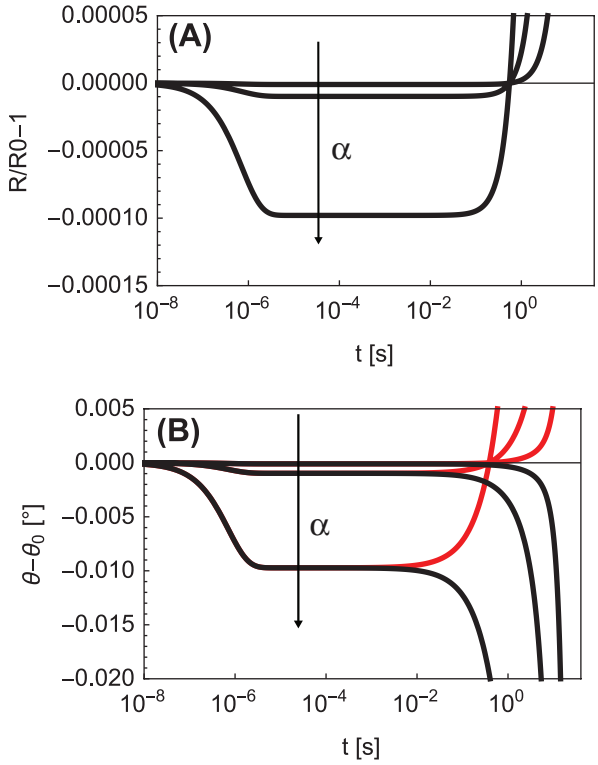

Fig. 4.5: $R/R_0 - 1$ (A) and $\theta_{\pm} - \theta_0$ ($\pm$ are, respectively, black and red) (B) as functions of time. $\alpha = \{-2,-3,-4\}$. $\eta_{CL} = \eta_0 10^3$ and $\varphi = 10^{-6}$. All other parameters are the same as in Fig. 4.4.

The bubbles we compare to the theory display non-circular footprints as they grow, especially during their early stages, Fig. 3.12 and Fig. 3.13. This raises the question whether Blake-Haynes contact line resistance alone or some degree of pinning is required to achieve such geometries. While our model is two-dimensional, we can still approximate these special cases. To do so we first examine the predictions when the rear contact line is pinned $\eta_{-,CL} \to \infty, \dot{x}_- \to 0$ (dashed line in Fig. 4.4), altering the slope φ to

$10^{-4.7}$ rad for a better fit with the experimental data. Further, Fig. 4.6 compares results of the Blake-Haynes theory with $\eta_{CL} = 10^3 \eta_0$, pinned rear contact line, and small amount of hysteresis $\beta_A = \{1.10, 1.15, 1.20\}$ ($\beta_R = 1$ for all) for fixed supersaturation $\alpha = -4$ and slope $\varphi = 10^{-5}$. We find that the pinned case produces velocities that are constant at early times, which is the same trend we observe in the experimental data. By introducing hysteresis instead of complete pinning, the model allows the bubble to depart (as observed in Fig. 3.12). Fig. 4.6 shows that larger amounts of hysteresis result in later departure as would be expected. The model predicts that bubbles can reattach at later times. This occurs because as the bubble grows, its growth rate and velocity diminish. The contact angles, therefore, tend towards their equilibrium values. If the departure from equilibrium is sufficiently small, the contact line will halt, resulting in reattachment. Detachment and reattachment events can be identified as the times when the hysteresis model begins to asymptote towards different extremes: predictions made by the pure Blake-Haynes model (dashed) and fixed rear contact line (dotted).

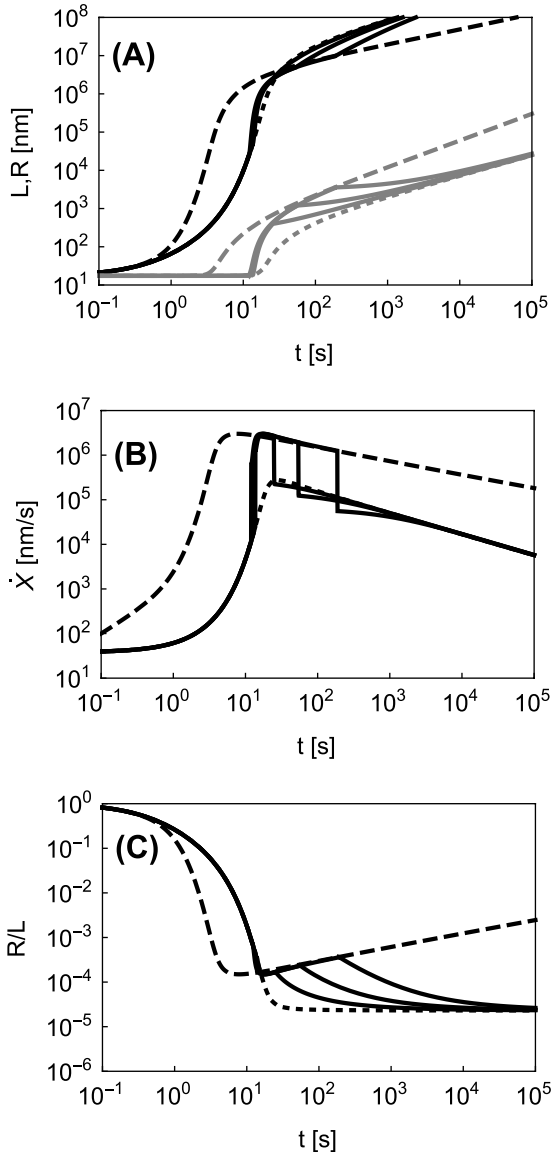

Fig. 4.6: Bubble half-length and radius of curvature (A), velocity (B), and ratio *R/L* (C) as functions of time. Blake-Haynes model $\eta_{CL} = \eta_0 10^3$ (dashed), pinned rear contact line $\eta_{CL,-} \to \infty$ (dotted), and hysteresis with $\beta_A = \{1.10, 1.15, 1.20\}$ and $\beta_R = 1$ (black, from left to right) results. For all trends, $\alpha = -4$ $\varphi = 10^{-6}$.

4.5. Conclusion

We observed highly transient bubble migration phenomena in the asymptotic limit of zero Capillary and Bond numbers that is only observable at sub-micron scales and proposed a model to explain the main features of the experimental data. Our model predicts continuous transport of a disperse phase in the absence of outside forces; all work is provided by the concentration gradient and subsequently dissipated at the contact line and in the creation of additional interface. The insights gained in this study have applications in multi-phase devices such as heat exchangers and catalytic devices where bubbles of vapor or gaseous products nucleate heterogeneously but must be cleared to free up surface area and maintain efficiency. Channel height, channel slope, and -in particular- contact line mobility are shown to play a crucial role in governing growth rate and velocity in both volume driven and mass transfer driven systems. Our results also have very specific applicability to liquid-cell electron-microscopy. Since liquid-cells used in electron-microscopy are created from thin, flexible materials, geometric non-uniformities are likely to be prevalent in many devices. Thus, confinement gradients need to be considered when fluid motion of drops and bubbles is observed. Conversely, one could take advantage of such a mechanism to prevent bubbles from interfering with an experiment, or draw them to a region for study.

The cylindrical nature of the bubble in our 2D model cannot address the tear-drop shaped bubbles seen in Fig. 3.10.C or predict pinch off events when bubbles are partially pinned [83]. However, our model does show that modifying diffusion limited growth to

include contact line dissipation can lower growth rates by orders of magnitude and bring theory much closer to observed dynamics. In order for the model to agree with experiment, we must use small gaps and small slopes; this supports the claim that the membranes have become laminated together in some way as described in Fig. 3.4 and are not bowed outward Fig. 3.3.

Chapter 5. Quasi-3D Bubble in a Hele-Shaw

5.1. Motivation

Chapter 4 introduced a two-dimensional dynamic model to describe the contact line and contact angle evolution of a bubble slug confined in a wedge geometry. The system was a convenient one to explore because the non-linear system of equations that describes the geometric constraints and Blake-Haynes relationship between contact angle and velocity could be readily solved using standard numerical tools. While the model did show how a bubble subject to mass or volume changes would force the contact angle out of equilibrium and drive both growth and net motion , questions remained about whether the prescription of the Blake-Haynes model would yield bubble geometries like those observed in liquid cell experiments described in Chapter 3 (the tear drop like bubbles in particular) and/or similar relationships between radial growth rate and velocity in a fully three-dimensional scenario. To deal with these shortcomings, a quasi-three-dimensional model will be developed in this chapter, and compared to the results of Chapter 4 and the experimental data from Chapter 3.

The model leverages four special limits. Firstly, as with all other models in this thesis, the zero Capillary number limit will be employed, allowing the details of the fluid flow interior and exterior to the bubble to be ignored. Secondly, the Young-Laplace equation will be scaled using two length scales: a characteristic radius of the projected bubble P and a characteristic thickness h_0. When these length scales are sufficiently disparate, the curvature equation can be simplified. Thirdly, it will be assumed that the bubble resides in a wedge that opens very slowly. Lastly, the geometry of the contact line

(projected onto the xy-plane) will be assumed to be nearly circular. The latter two of these simplifications will permit a spectral representation of the system. Such a representation will then allow integration of the spatial dimension to be performed analytically, leaving only the temporal evolution of the system to be determined numerically. Once the general model is derived, it will be used to explore four cases: prescribed volume $V \propto t^3$, mass transfer driven growth/migration, and each of those cases with and without an immobilized portion of the contact line.

5.2. Simplifying the Young-Laplace Equation

To begin, we consider a surface *z* parameterized in cylindrical coordinates by the radial position *r* and polar angle ψ . For such a surface, the Young-Laplace equation is given by

$$\frac{r\left[r\frac{\partial z}{\partial r}+r\left(\frac{\partial z}{\partial r}\right)^3+\frac{\partial^2 z}{\partial r^2}\left(r^2+\left(\frac{\partial z}{\partial \psi}\right)^2\right)+\frac{\partial^2 z}{\partial \psi^2}\left(1+\left(\frac{\partial z}{\partial r}\right)^2\right)\right]}{\left\{r^2\left[1+\left(\frac{\partial z}{\partial r}\right)^2\right]+\left(\frac{\partial z}{\partial \psi}\right)^2\right\}^{\frac{3}{2}}}=\frac{\Delta P}{\gamma} \qquad [5.1]$$

For a surface that is highly confined, the vertical length scale *h* is much smaller than the characteristic radius *P*. However, gradients with respect to *r* are sharp, and scale as *1/h*:

$$\begin{aligned} \frac{\partial}{\partial r} &\sim \frac{1}{h} \\ r &\sim P \\ z &\sim h \end{aligned} \qquad [5.2]$$

Applying these scales to the Young-Laplace equation gives

$$\frac{(P)r^*\left[\begin{array}{l}(P)r^*\dfrac{\partial z^*}{\partial r^*}+(P)r^*\left(\dfrac{\partial z^*}{\partial r^*}\right)^3+\left(\dfrac{1}{h}\right)\dfrac{\partial^2 z^*}{\partial r^{*2}}\left((P^2)r^{*2}+(h^2)\left(\dfrac{\partial z^*}{\partial \psi}\right)^2\right) \\ +(h)\dfrac{\partial^2 z^*}{\partial \psi^2}\left(1+\left(\dfrac{\partial z^*}{\partial r^*}\right)^2\right)\end{array}\right]}{\left\{(P^2)r^{*2}\left[1+\left(\dfrac{\partial z^*}{\partial r^*}\right)^2\right]+(h^2)\left(\dfrac{\partial z^*}{\partial \psi}\right)^2\right\}^{\frac{3}{2}}} = \left(\frac{h}{h}\right)\frac{\Delta P}{\gamma} = \left(\frac{1}{h}\right)\Delta P^* \qquad [5.3]$$

where we've introduced a dimensionless pressure jump $\Delta P^* = \Delta P\left(h/\gamma\right)$ .Rearranging and introducing the aspect ratio $\varepsilon = h/P$ gives

$$\frac{r^*\left[\varepsilon r^*\dfrac{\partial z^*}{\partial r^*}+\varepsilon r^*\left(\dfrac{\partial z^*}{\partial r^*}\right)^3+\dfrac{\partial^2 z^*}{\partial r^{*2}}\left(r^{*2}+\varepsilon^2\left(\dfrac{\partial z^*}{\partial \psi}\right)^2\right)+\varepsilon\dfrac{\partial^2 z^*}{\partial \psi^2}\left(1+\left(\dfrac{\partial z}{\partial r^*}\right)^2\right)\right]}{\left\{r^{*2}\left[1+\left(\dfrac{\partial z^*}{\partial r^*}\right)^2\right]+\varepsilon^2\left(\dfrac{\partial z^*}{\partial \psi}\right)^2\right\}^{\frac{3}{2}}} = \Delta P^* \qquad [5.4]$$

.

In the limit as the aspect ratio ε goes to zero, the equation reduces to

$$\frac{\dfrac{\partial^2 z^*}{\partial r^{*2}}}{\left\{1+\left(\dfrac{\partial z^*}{\partial r^*}\right)^2\right\}^{\frac{3}{2}}} = \Delta P^* \quad . \qquad [5.5]$$

Integration readily shows that a circle satisfies this differential equation. Thus, in the lubrication limit, each cross section of the interface is circular and variations with respect to the polar angle do not affect the pressure. While it is possible to consider higher order corrections, as discussed by Park and Homsy [7], we will henceforth assume that, in a plane oriented with the local normal of the contact line, the interface is a section of a circle.

5.3. Contact Line Geometry

By utilizing the lubrication limit, we no longer have to concern ourselves with the behavior of the interface in the *z*-direction. This section will show how the bubble geometry can be completely described in terms of its contact line and radius of curvature *R*.

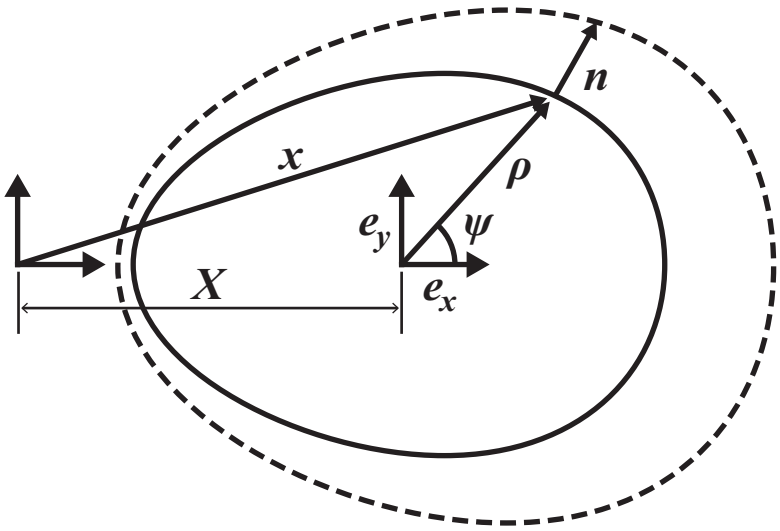

Fig. 5.1: Problem schematic, top view. Solid curve is the contact line, dashed curve is the bubble geometry at the mid-plane of the wedge.

We define the projection of a contact line point on the *xy*-plane in polar coordinates as

$$\mathbf{x}(\psi,t)=\left\{\rho(\psi,t)\cos\psi+X(t),\rho(\psi,t)\sin\psi\right\} \qquad [5.6]$$

To minimize clutter, once variable dependencies such as $\rho(\psi,t)$ are explicitly stated, they will be omitted in the remainder of the analysis. We define our coordinate system such that **x** (Fig. 5.1) is the global or lab Cartesian *xy*-coordinate, X is the center of the bubble measured in the lab frame of reference and ρ is the radial position of the interface measured from a coordinate system centered about X. An evolution equation for X will be developed later in the analysis. We define the center of the lab reference frame such that at $x=0$, the half-height of the channel is h_0; h_0 will be defined when the initial conditions for the model are discussed (eqn. [5.36]). In a coordinate system oriented with

the normal of the contact line, we have two equations for the local height of the tapered conduit that together will yield a unique equation for the local contact angle (as measured from the continuous phase). The first equation relates the radius of curvature R to the slope of the wedge in the plane normal to the contact line $\varphi(\psi)$ and $\theta(\psi)$

$$h = R\cos\left(\theta(\psi) - \varphi(\psi)\right) . \qquad [5.7]$$

We arbitrarily let the planes of the Hele-Shaw device diverge in the *x*-direction such that

$$h = h_0 + x\tan\Phi = h_0 + \left(X + \rho\cos\psi\right)\tan\Phi , \qquad [5.8]$$

where 2Φ is the total opening angle of the wedge. Equating [5.7] and [5.8] and solving for the contact angle gives

$$\theta = \cos^{-1}\left[\frac{h_0 + \left(X + \rho\cos\psi\right)\tan\Phi}{R}\right] + \varphi . \qquad [5.9]$$

A distinction must be made between the global or maximum wedge angle Φ and the local wedge angle $\varphi(\psi)$. The latter depends on the local normal of the contact line through the relationship

$$\tan\varphi = \hat{\mathbf{n}}\cdot\hat{\mathbf{e}}_x \tan\Phi \ , \qquad [5.10]$$

where

$$\hat{\mathbf{n}} = \left\{ \begin{array}{c} \rho\cos\psi + \dfrac{\partial\rho}{\partial\psi}\sin\psi \\ \rho\sin\psi - \dfrac{\partial\rho}{\partial\psi}\cos\psi \end{array} \right\} \sqrt{\rho^2 + \left(\frac{\partial\rho}{\partial\psi}\right)^2}^{-1} \ . \qquad [5.11]$$

For example, when $\hat{\mathbf{n}}\big|_{\psi=0} = \hat{\mathbf{e}}_x$, $\varphi\big|_{\psi=0} = \Phi$; when $\hat{\mathbf{n}}\big|_{\psi=\pi/2} = \hat{\mathbf{e}}_y$, $\varphi\big|_{\psi=\pi/2} = 0$. The relationship between φ and Φ (eqn. [5.10]) can be found by considering two vectors (one oriented along the *x*-axis, and another at an angle ω from the *x*-axis) that begin at the origin and end at points in the tapered conduit with the same height. The vector $\hat{\mathbf{e}}_x$ naturally sees the channel as diverging at an angle Φ. If we arbitrarily let the length of the second vector be W, from eqn. [5.8], we have

$$h_0 + W\tan\varphi = h_0 + W\cos\omega\tan\Phi \ , \qquad [5.12]$$

where we can recognize $\cos\omega$ as being the value of the scalar product of any unit vector with $\hat{\mathbf{e}}_x$. The normal vector can easily be derived from the equations $\hat{\mathbf{n}} = \dfrac{d\hat{\mathbf{t}}}{d\psi} \Big/ \left|\dfrac{d\hat{\mathbf{t}}}{d\psi}\right|$, where $\hat{\mathbf{t}} = \dfrac{d\mathbf{x}}{d\psi} \Big/ \left|\dfrac{d\mathbf{x}}{d\psi}\right|$ is the unit tangent vector. The full equation for the local wedge angle

$$\varphi = \tan^{-1}\left[\tan\Phi\left(\rho\cos\psi + \frac{\partial\rho}{\partial\psi}\sin\psi \right) \Big/ \sqrt{\rho^2 + \left(\frac{\partial\rho}{\partial\psi}\right)^2} \right]. \qquad [5.13]$$

For $\Phi \ll 1$, the expression can be linearized

$$\varphi \sim \Phi\left[\left(\rho\cos\psi + \frac{\partial\rho}{\partial\psi}\sin\psi \right) \Big/ \sqrt{\rho^2 + \left(\frac{\partial\rho}{\partial\psi}\right)^2} \right] + O\left(\Phi^2\right) \qquad [5.14]$$

An expansion about $\frac{\partial\rho}{\partial\psi} = 0$ for $\left(\frac{\partial\rho}{\partial\psi}\right) \ll 1$ (*i.e.* nearly circular bubble), yields additional simplification such that

$$\varphi \sim \Phi\left[\cos\psi + \frac{\partial\rho}{\partial\psi}\left(\frac{\sin\psi}{\rho}\right) + O\left(\frac{\partial\rho}{\partial\psi}^2\right) \right] + O\left(\Phi^2\right) \qquad [5.15]$$

.

The full expression for the local contact angle is

$$\theta = \cos^{-1}\left[\frac{h_0 + \left(X + \rho\cos\psi\right)\tan\Phi}{R} \right] + \tan^{-1}\left[\tan\Phi \frac{\left(\rho\cos\psi + \frac{\partial\rho}{\partial\psi}\sin\psi \right)}{\sqrt{\rho^2 + \left(\frac{\partial\rho}{\partial\psi}\right)^2}} \right]. \qquad [5.16]$$

When $\Phi \ll 1$ and $\left(\frac{\partial\rho}{\partial\psi}\right) \ll 1$ the expression can be linearized

$$\theta \sim \cos^{-1}\left(\frac{h_0}{R}\right) + \Phi\left[\cos\psi\left(1 - \frac{\rho}{HR}\right) - \frac{X}{HR} + \frac{\partial\rho}{\partial\psi}\left(\frac{\sin\psi}{\rho}\right) + O\left(\frac{\partial\rho}{\partial\psi}^2\right) \right] + O\left(\Phi^2\right), \qquad [5.17]$$

where $H = \sqrt{1-\left(h_0 / R\right)^2}$.

Under the Blake-Haynes description of contact line motion, the normal velocity of the interface is

$$\frac{\partial \mathbf{x}'}{\partial t} \cdot \hat{\mathbf{n}} = U_0 \cos\varphi \left[\cos\theta - \cos\theta_0 \right] \qquad [5.18]$$

where $U_0 = \gamma / \eta_{CL}$ and

$$\frac{\partial \mathbf{x}'}{\partial t} = \left\{ \frac{dX}{dt} + \frac{\partial \rho}{\partial t}\cos\psi, \frac{\partial \rho}{\partial t}\sin\psi \right\}, \qquad [5.19]$$

which comes directly from taking the time derivative of [5.6]. Note that we only consider the projection of the contact line motion in the *xy*-plane; there exists a small vertical component of the motion $\propto \sin\left(\varphi\right)$ that we do not need in the present analysis. As before, we linearize for $\Phi \ll 1$ and $\left(\frac{d\rho}{d\psi} \right) \ll 1$

$$\begin{aligned} &+\frac{\partial \rho}{\partial t} + \frac{dX}{dt}\left(\frac{\sin\psi}{\rho}\frac{\partial \rho}{\partial \psi} + \cos\psi \right) + O\left(\frac{d\rho}{d\psi}^2 \right) = \\ &\mathrm{U}_0 \left\{ \frac{h_0}{R} + \Phi \left[\frac{X}{R} + \cos\psi \left(\frac{\rho}{R} - H \right) - \frac{\sin\psi H}{\rho}\frac{\partial \rho}{\partial \psi} + O\left(\frac{\partial \rho}{\partial \psi}^2 \right) \right] - \cos\theta_0 + O\left(\Phi^2\right) \right\} \end{aligned} \qquad [5.20]$$

5.4. Bubble Center *X* Evolution

Since the geometry of the contact line is defined using polar coordinates and we assume $\partial\rho/\partial\psi \ll 1$, it is computationally advantageous to have the center of this coordinate system move with the contact line as it migrates. In order to find the evolution equation for the bubble's center, we require that $\rho(0,t)=\rho(\pi,t)$ or equivalently $(\partial\rho/\partial t)_{\psi=0}=(\partial\rho/\partial t)_{\psi=\pi}$ with $\rho(0,0)=\rho(\pi,0)$. Evaluating eqn. [5.20] for $\psi=0$ and $\psi=\pi$, subtracting the results, and incorporating $(\partial\rho/\partial t)_{\psi=0}=(\partial\rho/\partial t)_{\psi=\pi}$ gives the evolution equation

$$U_0\Phi\left(\rho(0)+\rho(\pi)\right)-R\left(2U_0\Phi H+2\frac{dX}{dt}\right)=0 \qquad [5.21]$$

.

5.5. Volume

The evolution of the contact line is governed by [5.20] and [5.21] but the space of possible interfaces needs to be further restricted for the system to be closed. For example, we could consider an isobaric process by letting $\dot{R}=0$ or enforce constant (or changing) mass or volume. For the latter two cases, an integral over the entire control volume needs to be written. The volume of the disperse phase can be divided into two contributions, a nearly cylindrical portion V_I and the portion that bulges out from the contact line V_{II}.

$$V_I=\int_0^{\rho(\psi)}\int_{-h(\psi)}^{h(\psi)}\int_0^{2\pi} r\,\mathrm{d}r\,\mathrm{d}z\,\mathrm{d}\psi=\int_0^{2\pi}\rho^2(\psi)\left(h_0+\rho(\psi)\cos\psi\,\mathrm{Tan}\,\Phi\right)\mathrm{d}\psi \qquad [5.22]$$

$$V_{II} = \int_0^S A\left(R,\varphi(\psi),\theta(\psi),\rho(\psi)\right)\mathrm{d}s = \int_0^{2\pi} \frac{R^2}{2}\begin{pmatrix}\pi - 2\theta(\psi) + 2\varphi(\psi) \\ -\sin\left(2\theta(\psi) - 2\varphi(\psi)\right)\end{pmatrix}\sqrt{\rho^2 + \left(\frac{d\rho}{d\psi}\right)^2}\,\mathrm{d}\psi \qquad [5.23]$$

In [5.23] it was assumed that $R \ll \rho$ to simplify the integrand. It can be further simplified by again lettering $\Phi \ll 1$ and $\left(\frac{d\rho}{d\psi}\right) \ll 1$ to yield

$$\begin{aligned} V &= V_I + V_{II} \\ &\sim \int_0^{2\pi} \frac{1}{2}\rho\left\{2h_0\rho + R^2\left[\pi - 2\mathrm{Cos}^{-1}\left(\frac{h_0}{R}\right) - \sin\left(2\mathrm{Sin}^{-1}\left(\frac{h_0}{R}\right)\right)\right]\right\} \\ &+\Phi\left[\frac{2}{3}\rho^3\cos\psi - h_0^2\frac{\partial\rho}{\partial\psi}\sin\psi + \rho^2\left(\frac{2h_0^2\cos\psi}{RH} + X\right) + \rho h_0^2\left(\cos\psi + \frac{2X}{RH}\right)\right] \\ &+O\left(\Phi^2\right)O\left(\frac{\partial\rho}{\partial\psi}^2\right)d\psi \end{aligned} \qquad [5.24]$$

.

5.6. Surface Area

Later in the analysis, a bubble subject to mass transport will be considered. Here we derive the expression for the *effective* surface area of a bubble available for mass transport. While the bubble is not perfectly cylindrical, the radius of the outward bulge is small compared to the overall radius of the contact line. We therefore expect the

concentration field around the bubble to be essentially similar to that around a cylindrical bubble. For an arbitrary cylinder the surface area is given by

$$S = \int_0^{2\pi} \int_{-h(\rho)}^{h(\rho)} \sqrt{\rho + \left(\frac{\partial \rho}{\partial \psi} \right)^2} \, dz \, d\psi \quad . \qquad [5.25]$$

Integrating in the z-direction gives

$$S = 2 \int_0^{2\pi} \left(h_0 + \left(X + \rho \cos\psi \right) \mathrm{Tan}\,\Phi \right) \sqrt{\rho + \left(\frac{\partial \rho}{\partial \psi} \right)^2} \, d\psi \quad , \qquad [5.26]$$

and linearizing yields the expression we will use for the effective area

$$S \sim 2 \int_0^{2\pi} \rho \left(h_0 + \Phi \left(X + \rho \cos\psi \right) \right) + O\left(\Phi^2 \right) O\left(\frac{\partial \rho}{\partial \psi} \right)^2 d\psi \quad . \qquad [5.27]$$

5.7. Spectral Representation

The system that resulted above consisted of a partial differential equation (the Blake-Haynes relationship), an integral constraint, and a point-wise constraint; the latter two equations being necessary to solve for, respectively, the radius of curvature and bubble center. To simplify the numerical integration of the mixed system of equations, a spectral decomposition of the contact line is proposed

$$\rho(\psi,t)=\sum_{n=0}^{N}\rho_n(t)\cos(n\psi)\ , \qquad [5.28]$$

and the governing Blake-Haynes equation [5.20] (BH) integrated with respect to ψ for each *n* used in [5.28]

$$\int_0^{2\pi}\cos(n\psi)\left(BH_{LHS}-BH_{RHS}\right)\mathrm{d}\psi=0\ . \qquad [5.29]$$

Such decomposition has the virtue of not only reducing the system to a set of non-linear ordinary differential equations but readily incorporating volume and point-wise constraints. Because the system is non-linear, such a Fourier-like expansion as this will not result in a system of independent equations governing the evolution of the coefficients (alternatively stated, the system does not permit a complete diagonalization as one is accustomed to when solving linear partial differential equations). Rather, we will be left with (*N*+1*)*+2 coupled equations (*N*+1 for the number of terms chosen, 1 for *X*, and a volume or mass constraint for *R*). Only even modes are selected because we expect the bubble to be symmetric with respect to the principal axis of the wedge (that is, symmetric about $\psi=0$). The problem could be generalized to include odd modes if, for example, initial conditions containing odd modes were of interest; odd modes will not be excited otherwise.

To illustrate the technique, we let N=2 and perform the integration on eqn. [5.20] , this gives three coupled equations corresponding to n=0,1 and 2 :

n=0

$$2\rho_0\frac{\partial\rho_0}{\partial t}+\rho_1\frac{\partial\rho_1}{\partial t}+\rho_2\frac{\partial\rho_2}{\partial t}=\frac{U_0}{R}\left\{2\rho_0\left[h_0-\cos\theta_0 R+\Phi\left(X+\rho_1\right)\right]+\Phi\rho_1\rho_2\right\}, \quad [5.30]$$

n=1

$$\frac{\partial\rho_2}{\partial t}\left(\frac{\partial\rho_1}{\partial t}-\frac{dX}{dt}\right)+2\rho_0\left(\frac{\partial\rho_1}{\partial t}+\frac{dX}{dt}\right)+\rho_1\left(2\frac{\partial\rho_0}{\partial t}+\frac{\partial\rho_2}{\partial t}\right) \quad [5.31]$$

$$=\frac{U_0}{2R}\left\{\begin{array}{l}4h_0\rho_1+\Phi\left[4\rho_0^2+4X\rho_1+3\rho_1^2+4\rho_0\rho_2+2\rho_2^2\right]\\+R\left[2\Phi H\left(\rho_2-2\rho_0\right)-4\cos\theta_0\rho_1\right]\end{array}\right\}$$

and

n=2

$$2\rho_2\frac{\partial\rho_0}{\partial t}+\rho_1\left(2\frac{dX}{dt}+\frac{\partial\rho_1}{\partial t}\right)+2\rho_0\frac{\partial\rho_2}{\partial t} \quad . \quad [5.32]$$

$$=\frac{U_0}{R}\left[2h_0\rho_2-R\left(2\Phi H\rho_1+2\cos\theta_0\rho_2\right)+2\Phi\left(\rho_0\rho_1+X\rho_2+\rho_1\rho_2\right)\right]$$

The remaining governing equations do not need to be integrated, substituting the form [5.28] into eqn. [5.21] gives

$$-U_0\Phi\left(\rho_0+\rho_2\right)+R\left(U_0\Phi H+\frac{dX}{dt}\right)=0\,. \quad [5.33]$$

The volume (eqn. [5.24]) and surface area (eqn. [5.27]) integrals give, respectively

$$V_{SE} = \frac{1}{rRH}\left\{\begin{array}{l} 4\pi HR\rho_0^2\left(h_0 + \Phi X + \Phi\rho_1\right) + 4h_0^2\pi\Phi\rho_1\rho_2 \\ +4\pi\rho_0\left[R^2 h_0 + \mathrm{Sin}^{-1}\left(\frac{h_0}{R}\right)HR^3 + h_0^2\left(h_0 + 2\Phi X + 2\Phi\rho_1\right) + \Phi HR\rho_1\rho_2\right] \\ +\pi HR\left[2\left(h_0 + \Phi X\right)\rho_1^2 + 2\left(h_0 + \Phi X\right)\rho_2^2 + \Phi\left(\rho_1^3 + 2\rho_1\rho_2^2\right)\right] \end{array}\right\}, \quad [5.34]$$

and

$$S_{SE} = 2\pi\left[2\rho_0\left(h_0 + \Phi\left(X + \rho_1\right)\right) + \Phi\rho_1\rho_2\right]. \quad [5.35]$$

5.8. Initial Conditions

As with previous chapters, we assume that the initial geometry of the bubble is spherical and possesses the equilibrium contact angle. While a spherical bubble does not satisfy the assumption $\varepsilon \ll 1$, it is the *only* geometry that creates a uniform contact angle along the entire contact line; using a different geometry would introduce additional dynamics at early times. From simple geometric considerations, we again have the following relationship between the initial radius and the height of the channel at the center of the sphere

$$R_0 = R\left(t = 0\right) = h_0\frac{\cos\Phi}{\cos\theta_0}. \quad [5.36]$$

The initial contact line is thus a circle with radius $R_0 \sin\theta_0$, but the projection of this circle onto the *xy*-plane is an ellipse with major and minor radii given by

$$\mathrm{R}_E = \left\{ \begin{array}{c} \mathrm{R}_0 \sin\theta_0 \\ \mathrm{R}_0 \sin\theta_0 \cos\Phi \end{array} \right\} = \left\{ \begin{array}{c} h_0 \tan\theta_0 \cos\Phi \\ h_0 \tan\theta_0 \cos^2\Phi \end{array} \right\} . \qquad [5.37]$$

In our polar coordinate system centered around X is described by

$$\rho\left(t=0\right) = \frac{h_0 \tan\theta_0 \cos^2\Phi}{\sqrt{\cos^2\psi + \cos^2\Phi \sin^2\psi}} . \qquad [5.38]$$

where the initial center of the *contact line*

$$X\left(t=0\right) = -h_0 \sin\Phi\cos\Phi . \qquad [5.39]$$

Note that this value is negative because the center of the contact line is to the left of the center of the sphere and we've set the zero for the global coordinate system such that the half-height at zero is h_0.

5.9. Model Results

5.9.1. Volume Controlled Case

In order to gain an initial understanding of this new system, we first consider an insoluble bubble/droplet subject to a prescribed volume variations $V \propto t^3$; all results presented in this section are in dimensionless form. The initial gap height h_0 is the length and the Blake-Haynes velocity U_0 enables us to generate the time scale h_0 / U_0. We initially explore the behavior of the system when N=3,4, and 5. We compare the predictions with three different truncations in Fig. 5.2. The figure shows that, while some information of bubble geometry flows into the higher order modes at short times, the long time behavior is governed by the leading order mode ρ_0 only. Initially, $\rho_2 \neq 0$ because the contact line begins with an elliptical geometry, eqn. [5.38]. Now that we've established that the leading order mode dominates for the most part, we can compare its evolution, as well as that of the radius of curvature *R* and position *X* as a function of time for different truncations, Fig. 5.3. If we take the N=5 truncation as our reference ("exact") solution, we can see that, with the exclusion of early times, increasing the level of the truncation does not alter the overall outcome of the key variables. In order to reduce the complexity of the system, all results presented henceforth are with N=3.

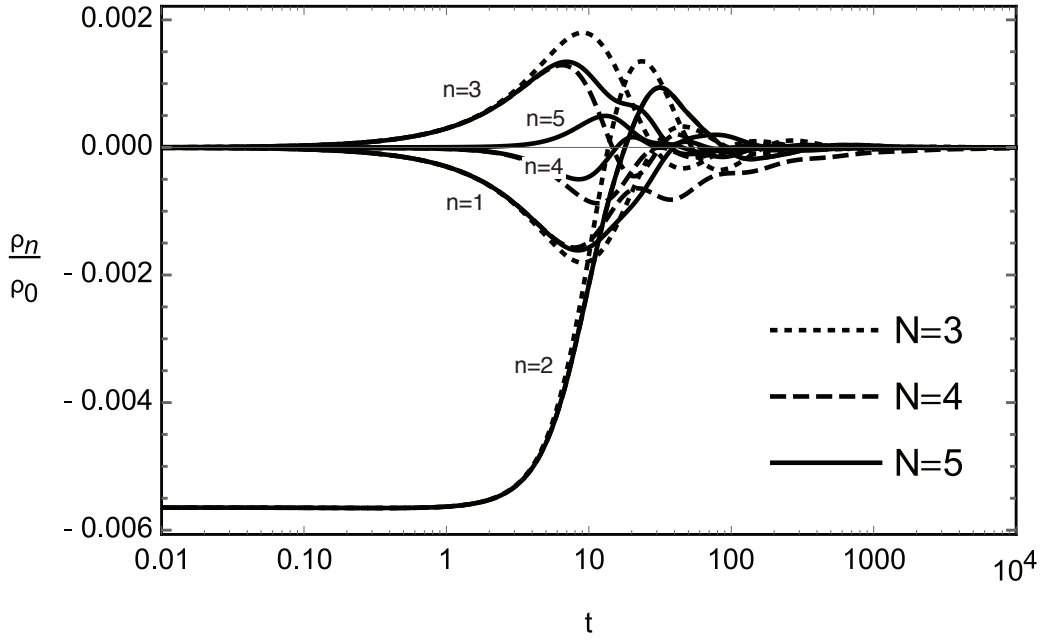

Fig. 5.2: Coefficient evolution (n=1,2…N) normalized by the 0th order mode for three different truncations (N=3,4,5). In the long time limit, the contact line assumes a perfectly circular geometry regardless of where the series was truncated. Different line styles correspond to the three different N used (see key); coefficents (n) are labeled.

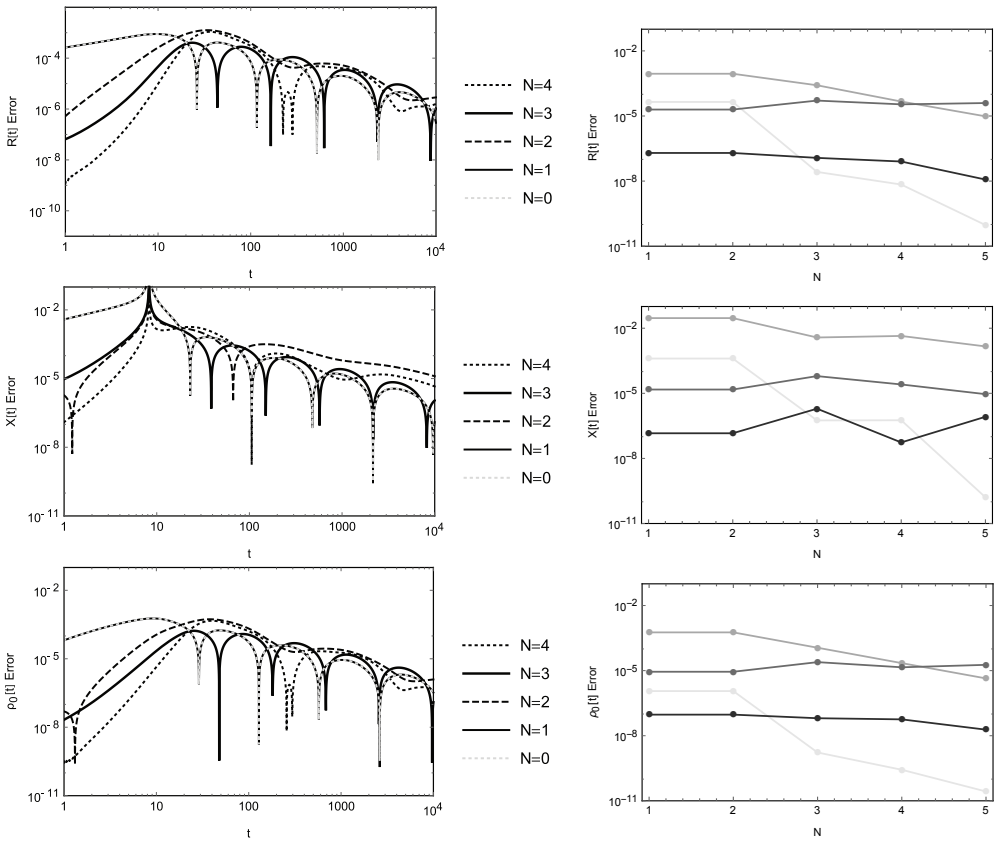

Fig. 5.3: Relative Error R, X and ρ_0 (1st, 2nd, and 3rd rows, respectively) for N=0,1,2,3,4 compared to N=5 ($\text{Error} = \left|\left(f_N - f_5\right)/f_5\right|$). Left column shows temporal evolution of the error and in the right column, gray scale indicate time (from light to dark, $t = 10^{-1}, 10^{1}, 10^{3}, 10^{5}$).

Fig. 5.4 depicts the evolution of X, R, ρ_0 and their rates of change; like the results of Chapter 4, dynamics become more pronounced as V_0^* gets larger. In Fig. 5.4, we observe non-monotonic evolution in both the radial growth rate $\dot{\rho}_0$ and rate of change of the radius of curvature $\dot{R}$. Fig. 5.5 and Fig. 5.6 show, respectively, the aspect ratio R/ρ_0 and contact angle distribution $\theta(\psi)$ for a few different growth rates. All of the quantities eventually grow $\propto t$; it then follows that the aspect ratio should reach a steady

value, which it does. To accommodate increasing volume the bubble has two avenues: spreading radially and moving down the confinement gradient to gain height. As the volume rate increases relative to the ability of the contact line to move, the bubble becomes more "pancake" like because it is unable to move to wider parts of the channel fast enough and instead, spreads radially. We note that the bubble initially begins at an aspect ratio that violates the assumptions, under which the model was developed, $\varepsilon \to 0$.

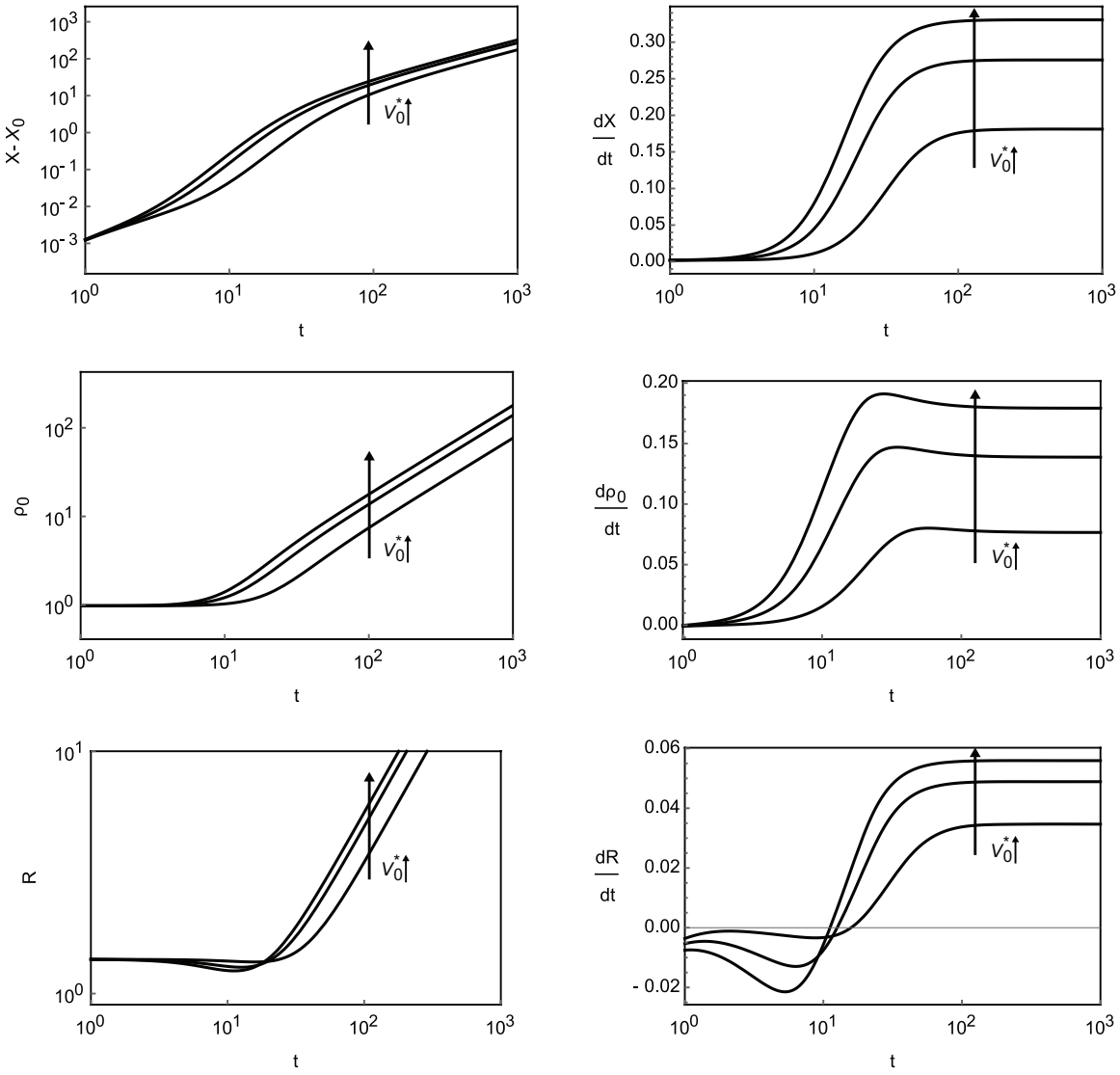

Fig. 5.4: (Left Column) Temporal evolution of bubble center X, average contact line radius ρ_0, and radius of curvature R and (Right Column) their time derivatives for $V_0 = \left\{1\times10^{-3}, 5\times10^{-3}, 1\times10^{-2}\right\}$; values correspond to curves from bottom to top in all plots.

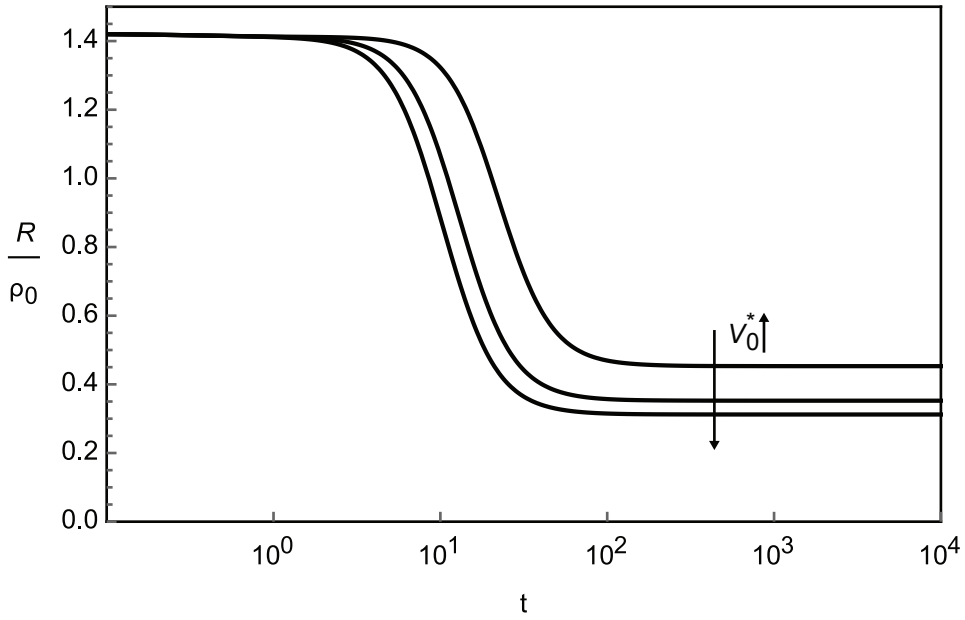

Fig. 5.5: Temporal evolution of the ratio between the radius of curvature R and the 0th mode ρ_0 that governs the average radius of the droplet. The droplet begins as a sphere (the initial ratio being dictated by the contact angle and wedge angle eqn. [5.37]) but becomes more "squashed" as time goes on. Under volume controlled cases $V^* \propto V_0^* t^3$, a geometric steady state of self-similar growth is reached. From top to bottom $V_0^* = \left\{1\times10^{-3}, 5\times10^{-3}, 1\times10^{-2}\right\}$. As noted when describing the initial conditions, the model is initiated as a sphere in order to satisfy an initially uniform contact angle, even though the assumption $R/\rho_0 = \varepsilon \ll 1$ is initially violated.

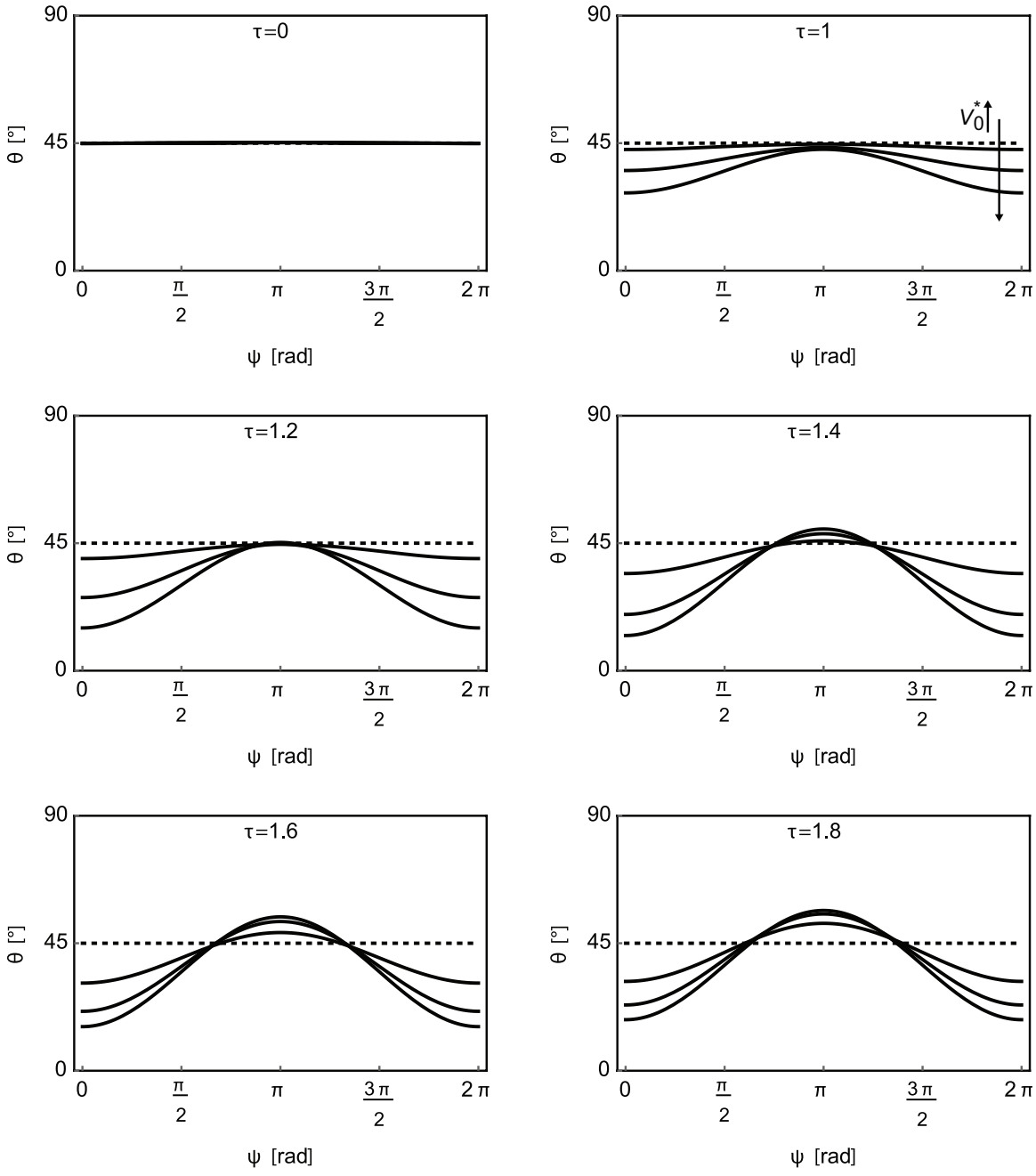

Fig. 5.6: Contact angle evolution for $V_0^* = \left\{10^{-3}, 5\times10^{-3}, 10^{-2}\right\}$; amplitude in contact angle variation increases with V_0^* . N=3.

We can formalize our finding that $\lim_{t\to\infty}\rho_0, X, R \propto t$ while $\lim_{t\to\infty}\rho_{1,2..N} = 0$ by letting $\rho_0, X, R \sim P^* t, X^* t, R^* t$, substituting into [5.30], and [5.34] and retaining only the leading order terms as $t \to \infty$. Doing so creates the the system

$$\begin{aligned} 2\pi P^*\left(3P^* X^* \Phi\right) - 3V_0 &= 0 \\ 2R^*\left(X^* + U_0\Phi\right) - 2P^* U_0 \Phi &= 0 \\ P^* R^* - U_0 X^* \Phi + R^* U_0 \cos\theta_0 &= 0 \end{aligned} \quad . \qquad [5.40]$$

The system has multiple roots, but only one physical solution. Fig. 5.7 compares the asymptotic solution to the full solution (N=3) and shows excellent agreement.

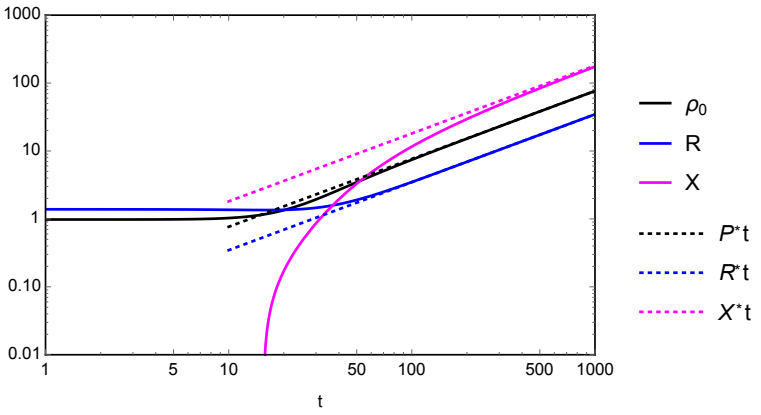

Fig. 5.7 : Comparison between N=3 system and asymptotic values found from $\Phi = 0.15, U_0 = 1, \theta_0 = \pi/4, V_0 = 10^{-3}$

The asymptotic forms can also be applied to the linearized contact angle equation [5.17] to yield the steady state contact angle distribution.

$$\lim_{t\to\infty}\theta \sim \frac{\pi}{2} + \Phi\left[\cos\psi\left(1 - \frac{P^*}{R^*}\right) - \frac{X^*}{R^*}\right] \qquad [5.41]$$

We conclude from this portion of the analysis that when the volume is prescribed to grow in time with the same exponent as the dimension of the problem $V \propto t^3$, a dynamic steady state is approached as $t \to \infty$. This asymptotic state is fully described by a linear evolution of the mean radius, position, and radius of curvature. This growth is scale invariant or self-similar because the relationships between the linear dimensions remain constant. Self-similarity is further evidenced by a steady state contact angle distribution, eqn. [5.41]. Stated alternatively: in the long time limit, the droplet/bubble possesses a contact angle distribution that furnishes a contact line velocity which brings the contact line to a new position at the next time instant where the identical contact angle distribution exists. To the best of my knowledge, this is the first time such an application of the Blake-Haynes model has been used to gain insights into bubble locomotion.

5.9.2. Partially Pinned Bubble – Volume Controlled

In Chapter 4, the case of a completely immobile, rear contact line was considered. To emulate this in the current model, a weighting function is introduced to our linearized BH eqn. [5.20] $\left(1+\cos\psi\right)/2$ such that

$$\frac{\partial \rho}{\partial t}+\frac{dX}{dt}\left(\frac{\sin\psi}{\rho}\frac{\partial \rho}{\partial \psi}+\cos\psi\right)= \\ \mathrm{U}_0\frac{\left(1+\cos\psi\right)}{2}\left\{\frac{h_0}{R}+\Phi\left[\frac{X}{R}+\cos\psi\left(\frac{\rho}{R}-H\right)-\frac{\sin\psi H}{\rho}\frac{\partial \rho}{\partial \psi}+\right]-\cos\theta_0\right\} \quad [5.42]$$

The weighting function enforces zero velocity at $\psi = \pi$ and smoothly transitions to the full BH velocity $\psi = 0$. The same integration as before, eqn. [5.29], is performed; for *N=2*, eqns. [5.30]-[5.32] become

n=0

$$2\rho_0 \frac{\partial \rho_0}{\partial t} + \rho_1 \frac{\partial \rho_1}{\partial t} + \rho_2 \frac{\partial \rho_2}{\partial t} = \frac{U_0\left[2\rho_0\left(h_0 - \cos\theta_0 R\right) + \Phi\left(\rho_1 + X\right)\right] + \Phi\rho_1\rho_2}{R}, \quad [5.43]$$

n=1

$$\begin{aligned} &\frac{\partial \rho_2}{\partial t}\left(\frac{\partial \rho_1}{\partial t} - \frac{dX}{dt}\right) + 2\rho_0\left(\frac{\partial \rho_1}{\partial t} + \frac{dX}{dt}\right) + \rho_1\left(2\frac{\partial \rho_0}{\partial t} + \frac{\partial \rho_2}{\partial t}\right) \\ &= \frac{U_0}{2R}\left\{\begin{array}{l} 4h_0\rho_1 + R\left[-\cos\theta_0\rho_1 + 2\Phi H\left(\rho_2 - 2\rho_0\right)\right]\ldots \\ +\Phi\left[4X\rho_1 + 3\rho_1^2 + 2\left(2\rho_0^2 + 2\rho_0\rho_2 + \rho_2^2\right)\right] \end{array}\right\} \end{aligned} \quad [5.44]$$

and

n=2

$$\begin{aligned} &2\rho_2 \frac{\partial \rho_0}{\partial t} + \rho_1\left(2\frac{dX}{dt} + \frac{\partial \rho_1}{\partial t}\right) + 2\rho_0 \frac{\partial \rho_2}{\partial t} = \quad . \quad [5.45] \\ &\frac{U_0}{R}\left[2h_0\rho_2 + R\left(-2\Phi H\rho_1 - 2\cos\theta_0\rho_2\right) + \Phi\left(2\rho_0\rho_1 + 2X\rho_2 + 2\rho_1\rho_2\right)\right] \end{aligned}$$

Eqn. [5.33] ,the constraint needed to describe the evolution of the center *X*, is modified as well, becoming

$$U_0\left(\frac{h_0 + \Phi\left(X + \rho_0 + \rho_1 + \rho_2\right)}{R} - \cos\theta_0 - \Phi H\right) = 2\dot{X} \quad . \quad [5.46]$$

Fig. 5.8 shows the contact line evolution for $\Phi = 0.1$ and 0.01, and $V_0 = 10^{-4}$. We see that, for the same volume and times, the contact line is more circular for the smaller slopes. By scaling the geometries (bottom row of Fig. 5.8) we see that over longer time scales, the $\Phi = 0.01$ case assumes geometries much like $\Phi = 0.1$.

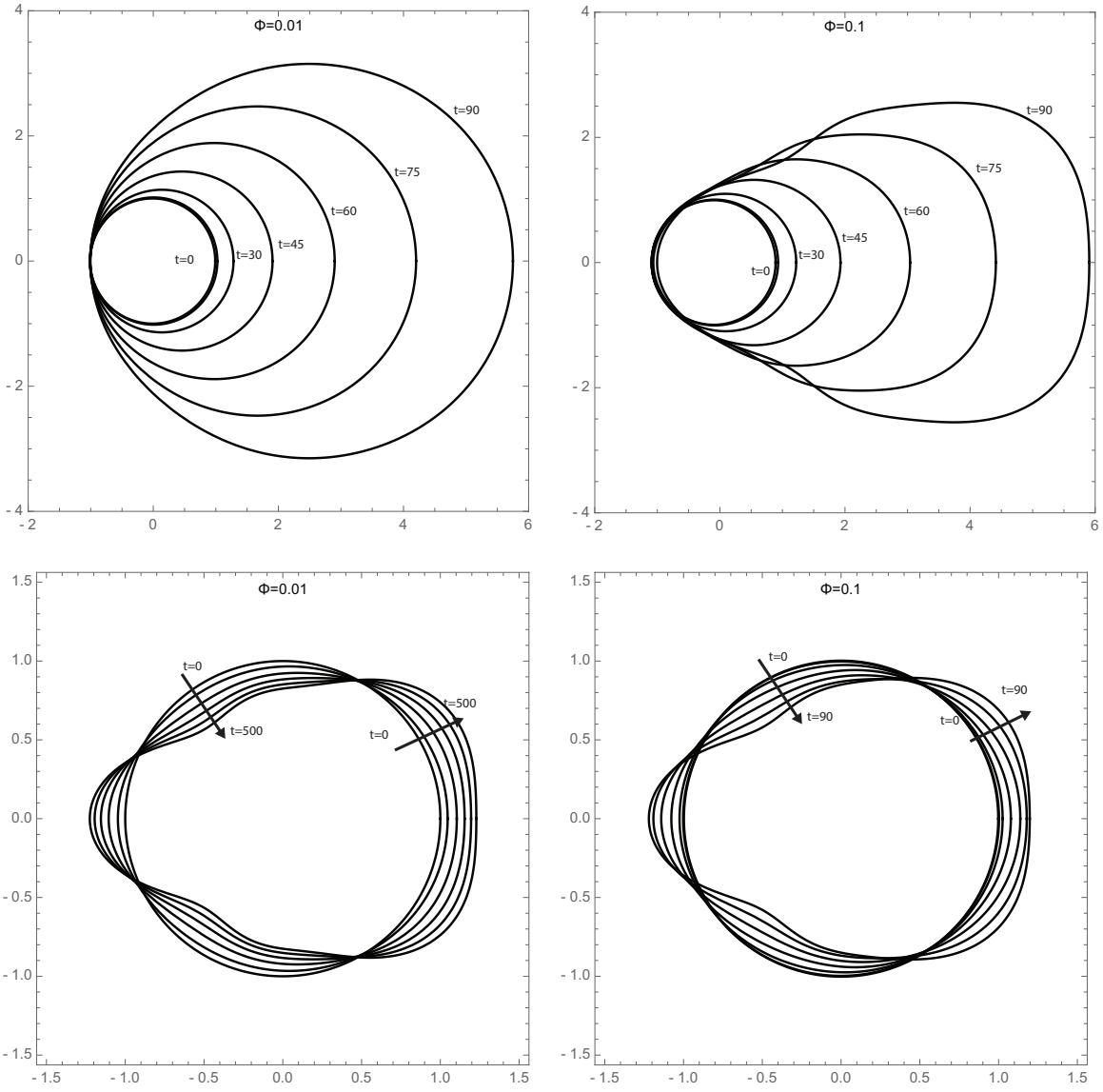

Fig. 5.8: (Top Row) Contact line evolution of a partially pinned bubble for $V_0^* = 10^{-4}$, $t = 0,15,30\cdots 90$ for two different slopes $\Phi = 0.01$ and 0.1; (Bottom Row) the same contact line normalized by the average radius ρ_0 and centered around X, note that a larger time range is used ($t = 0,100,200\cdots 500$) for the $\Phi = 0.01$ case to illustrate that the same elongated geometry of $\Phi = 0.1$ is approached. $\theta_0 = 45^\circ$

5.9.3. Mass Transfer Driven Growth

Finally, we explore the results of the model driven by mass transfer with and without partial pinning of the contact line. Fig. 5.9 compares the 2D model described in Chapter 4 to the model developed in this chapter for different Φ, both without any pinning. We observe qualitative agreement between the two models. The predictions differ slightly in the maximum growth rates and velocities achieved in the long time. The radius of curvature evolution also appears to be slightly more sensitive to changing slopes in the 3D case; that is, for the same change in slope, the curves are more spread out in time. However, unlike the 2D cases, in 3D, we can compare the entire contact line to the experimental data, not just the "reduced" metrics of half-length *L* (see Chapter 4) and position *X*. We are now poised to answer the question: does contact line dissipation result in "tear-drop" shaped bubbles?

Fig. 5.10 compares theoretical contact lines (for pinned A and unpinned B) to experimental observations. One can garner that, while the overall predictions of bubble size are the same for pinned and unpinned cases, only the pinned case can yield the teardrop geometries observed. Fig. 5.11 compares the 2D (dotted lines) and 3D (solid lines) models for pinned (gray) and unpinned (black) cases to experimental observations of one nucleation site (using the same model parameters as Fig. 5.10). Interestingly, we

see that the overall size evolution for the four different cases agree at early times. The biggest differences are seen in the velocity evolution. When the entire contact line is free to move at the Blake-Haynes velocity, the 2D and 3D predictions are roughly the same over the experimentally relevant time scale. However, when the contact rear portion of the contact line is fixed, 2D and 3D predictions differ; the 2D case predicts a constant velocity while the 3D, a deceleration. We can conclude from this that when contact line pinning is present, the ability of the bubble to accommodate mass by spreading out perpendicular to the confinement gradient has a strong impact on the overall velocity.

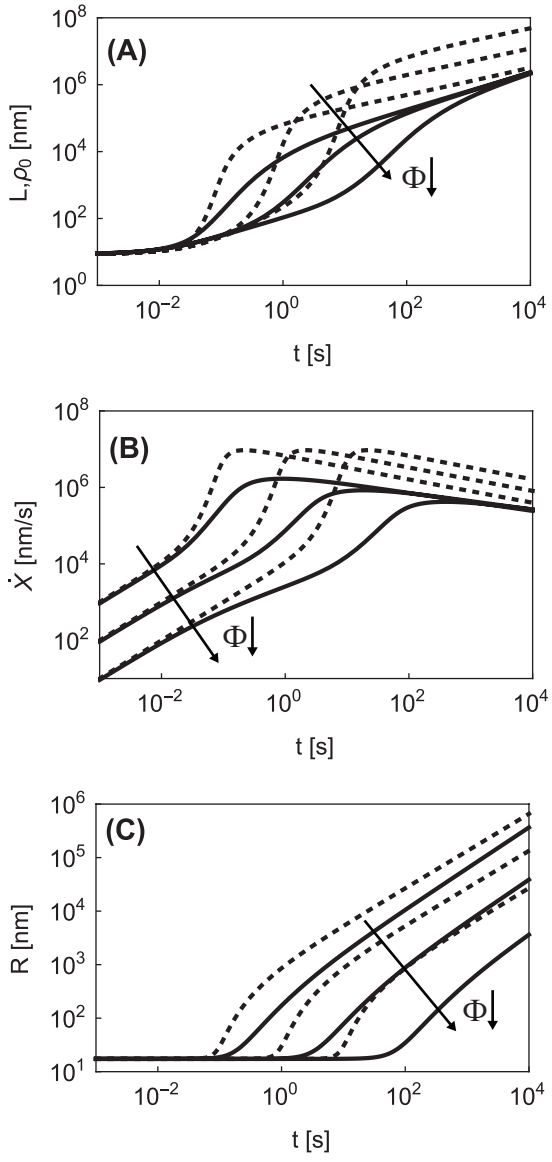

Fig. 5.9: Comparison between 2D model (dotted line) presented in Chapter 4 and 3D model (solid line) of (A) Bubble size (half length L for 2D model or ρ_0 for 3D model), (B) velocity, and (C) radius of curvature *R* for a few different wedge angles, $\Phi = \left\{10^{-4}, 10^{-5}, 10^{-7}\right\}$. Growth is driven by mass transfer. $\eta = \eta_0 10^3, \alpha = -3, h_0 = 15[nm]$

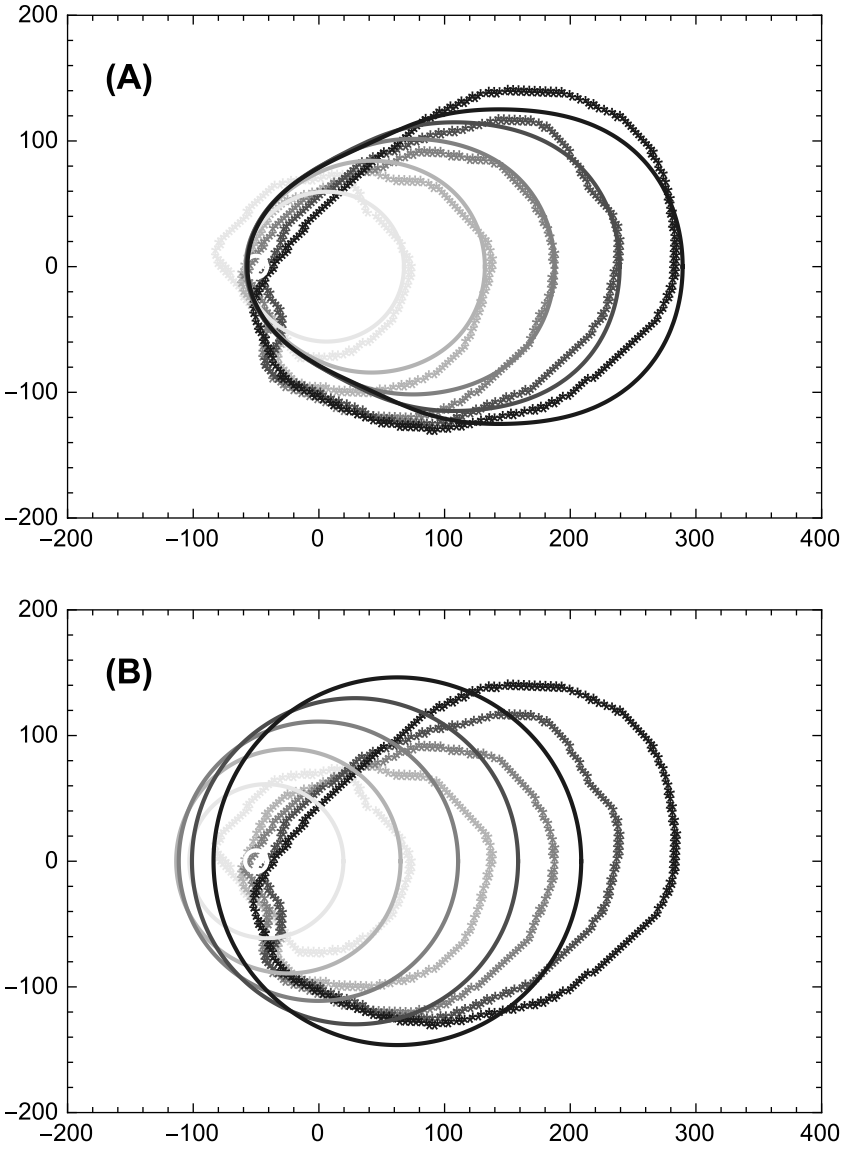

Fig. 5.10: Contact line evolution comparison between experiment (data points) and mass transfer driven model (lines) with partial contact line pinning (A) and without it (B), darker lines and points correspond to later times. Values that provided the best fit to the experimental data are $\Phi = 10^{-6.3}, \eta = \eta_0 10^2, \alpha = -2.73, h_0 = 15[nm]$, time between frames $\Delta t = 0.2[s]$.

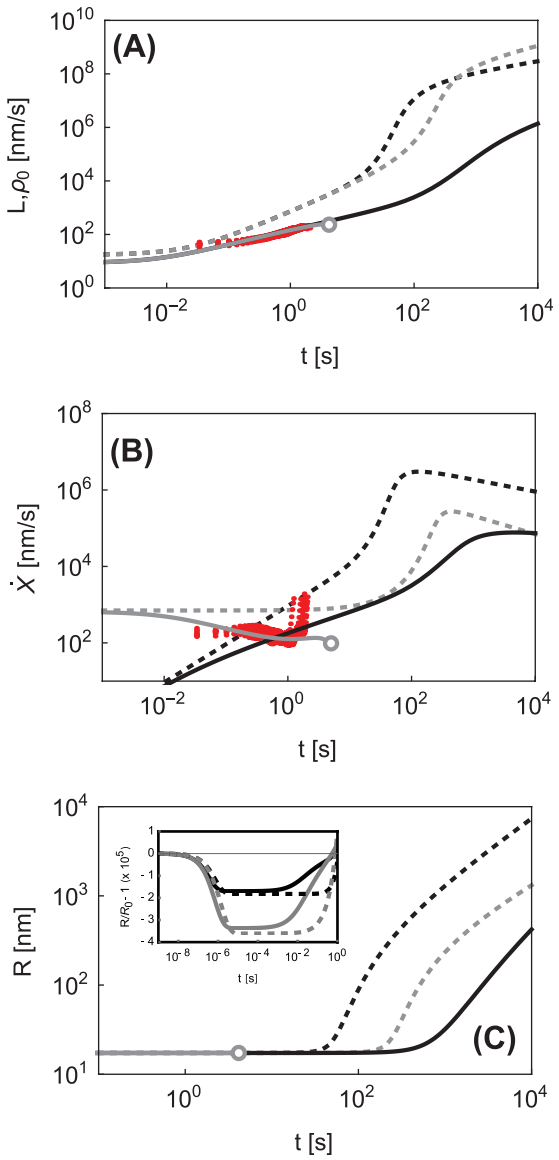

Fig. 5.11: Comparison between 2D model with (gray, dotted line) and without (black, dotted line) a pinned rear contact line, 3D model with and without contact line pinning (respectively, gray and black solid lines), and the experimental data of 7 bubbles that nucleated at the same location. (A) Bubble size (half length L for 2D model or ρ_0 for 3D model), (B) velocity, and (C) radius of curvature *R* for mass transfer driven growth $\Phi = 10^{-6.3}, \eta = \eta_0 10^2, \alpha = -2.73, h_0 = 15[nm]$, these are the same values that provided the best fit in Fig. 5.10. An open, gray circle marks the end of the predictions made by the pinned, 3D model.

5.10. Conclusions

A quasi-3D model has been derived and solved using a pseudo-spectral method. The volume-controlled case gives interesting insights into the coupling between bubble geometry, growth, and motion. In the long time limit, we are able to derive simple expressions for the geometric evolution of droplets and bubbles; in particular a simple expression for the contact angle distribution is furnished. When mass transfer and partial pinning are added, substantial agreement is found between model predictions and experimental observations. Namely, the 3D model allows us to conclude that contact line friction alone is not sufficient to achieve tear-drop-like geometries, as observed experimentally – partial pinning (modeled using a weighting function to the Blake-Haynes equation) must be included. However, while pinning must be included to get the *best* agreement, the unpinned model still produces velocities and growth rates orders of magnitude slower than Epstein-Plesset theory[20]. Including partial contact line pinning also makes another fact clear: contact line geometries are growth rate dependent. This is evidenced by Fig. 5.8; we see that the slower the growth rate, the more circular the contact line will be at early times. This may have important implications in determining the size at which bubbles "depart" from their nucleation site.

The experimental data shows a rapid change in velocity that we cannot account for in either 2D or 3D models. Since bubble geometries are well modeled up until that point, this is a strong indication that either instability driven breakup as described by Dangla *et al.* is occurring (however, unlike Dangla *et al.*, the geometries present here are growth rate dependent) or that contact angle hysteresis is present. Understanding the

departure mechanism is a logical next step for this work. Within the framework developed thus far, it is the most straight forward to consider the latter mechanism first. As suggested by the results of Chapter 4, introducing even small amount of contact hysteresis allows for rapid changes in velocity, Fig. 4.6. However, while it was possible to implement a contact angle hysteresis into the 2D model with relative ease, the spectral method employed in this chapter would have required many terms to satisfactorily account for a step-discontinuity in the equations of motion. Yet, this is a limitation of the solution method not the model itself and can perhaps be overcome if a more general numerical technique is employed. The biggest hurdle is implementation of a volume constraint, which was handled readily by the spectral method.

Chapter 6. Growing Sessile Bubble with Contact Line Dissipation

6.1. Motivation

The previous chapters established the potential large impact of confinement and contact line dissipation on diffusion driven growth of bubbles. In this chapter, a simpler case is examined, that of a spherical bubble growing on only one substrate. The importance of complete contact-line pinning on the persistence of sessile nanobubbles has been demonstrated by Lohse and Zhang [22]. Here we examine whether or not a contact line with only partially restricted movement can yield additional insights. Once the model is developed, we will our compare model predictions to the experimental work of Li *et al*. [105], who examined the growth of bubbles by diffusion on a substrate and published data on the evolution of both the radius and the contact angle.

6.2. Insoluble

To illustrate the impact of contact line resistance on bubble growth we first consider the case of an insoluble droplet with a transient but prescribed volume variations $V \propto t^3$. The volume of a spherical cap of radius R that makes a contact angle θ with the substrate (as measured through the continuous phase, Fig. 6.1) is given by [106]

$$V\left(R\left(t\right),\theta\left(t\right)\right)=\frac{1}{3}\pi R^3\left(2-\cos\theta\right)\left(1+\cos\theta\right)^2=V_0t^3\ , \qquad [6.1]$$

The system is closed using the linearized Blake-Haynes model[11], [12]

$$\eta_{CL}\left(\dot{R}\sin\theta+R\dot{\theta}\cos\theta\right)=\gamma\left(\cos\theta-\cos\theta_0\right), \qquad [6.2]$$

which relates the instantaneous contact line (which has radius $R\sin\theta$) velocity to the dynamic contact angle through the contact line viscosity η_{CL} and surface tension γ . It is assumed, by using this model, that the contact angle possesses no size or space dependency and that any departure from equilibrium is due purely to dynamics. Space heterogeneities could be the result of intentional patterning or contamination. A structurally patterned surface (such as a pillar array) could give rise to an apparent contact angle that differs from the actual, material contact angle. Such a surface might also see a size dependent contact line viscosity because the energy barrier associated with moving the interface would be that required to hop from one pillar to the next, instead of moving between substrate molecules. The system is now non-dimensionalized using the initial radius $R\left(t=0\right)=R_0$ as the length scale and the velocity scale γ/η_{CL} ,

$$\begin{aligned}&\frac{1}{3}\pi R^{*3}\left(2-\cos\theta\right)\left(1+\cos\theta\right)^2=V_0^*t^{*3}\\&\dot{R}^*\sin\theta+R^*\dot{\theta}\cos\theta=\cos\theta-\cos\theta_0\end{aligned}\ , \qquad [6.3]$$

where $V_0^*=V_0\eta_0/\gamma R_0^2$.

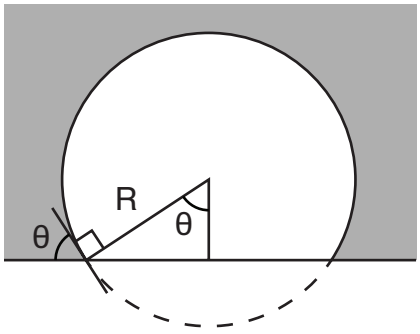

Fig. 6.1: Schematic of a spherical sessile bubble (white) of radius R with a contact angle θ (as measured from the liquid side, gray).

The time evolutions of R^* and θ for several values of V_0^* are plotted in Fig. 6.2; the results are qualitatively similar to the results for the 2D and quasi-3D bubbles presented in the previous chapters. When $V_0^* < 1$ the timescale associated with volume gain is smaller than that associated with contact line motion and only weak departures of the contact angle from equilibrium occur. When $V_0^* > 1$ contact line dissipation plays a more dominant role in controlling the geometry. Like the models in Chapters 4 and 5, self-similar growth is also achieved for this system in long times. The asymptotic values can be found by assuming the forms $\lim_{t\to\infty} R^* = R_\infty^* t$ and $\lim_{t\to\infty} \theta = \theta_\infty$, substituting them into [6.3], retaining only the largest terms as $t \to \infty$. These steps create the system

$$\left\{ \begin{array}{c} \frac{1}{3}\pi R_\infty^{*3}\left(2-\cos\theta_\infty\right)\left(1+\cos\theta_\infty\right)^2 \\ R_\infty^* \sin\theta_\infty - \cos\theta_\infty \end{array} \right\} = \left\{ \begin{array}{c} V_0^* \\ -\cos\theta_0 \end{array} \right\}, \qquad [6.4]$$

which can be numerically solved. The asymptotic values are plotted in gray, dashed lines in Fig. 6.2. A and B.

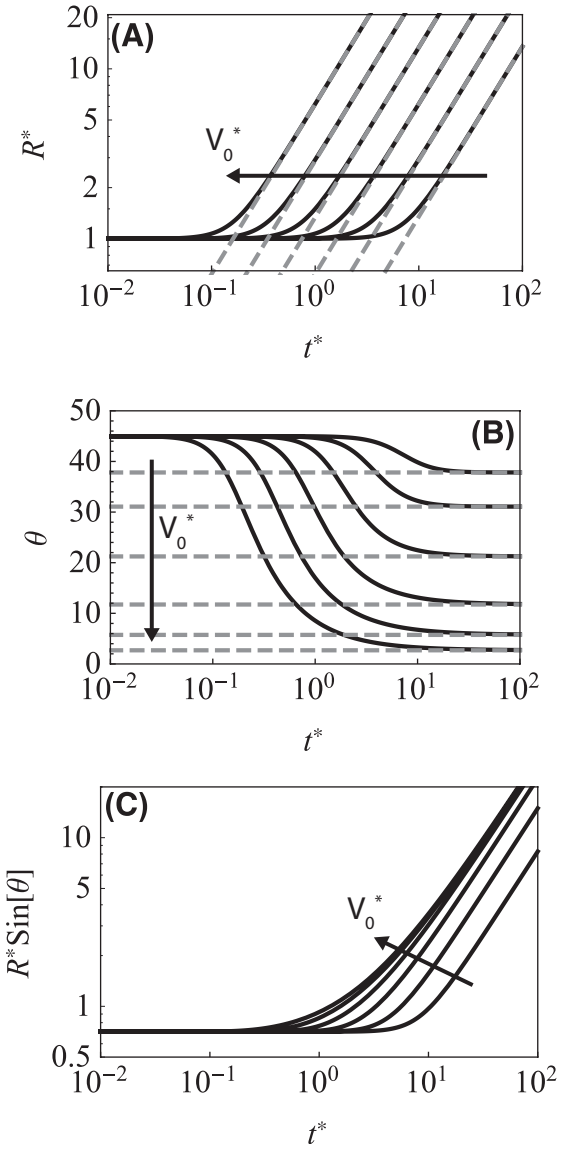

Fig. 6.2: (A) radius of curvature, (B) contact angle and (C) contact line radius of an incompressible droplet growing according to $V^* = V_0^* t^{*3}$, $V_0^* = \left\{10^{-2}, 10^{-1}, 1, 10, 10^2, 10^3\right\}$. At $t \gg 1$, $R \propto t$ (dotted line) and $\dot{\theta} \to 0$ (larger growth rates are associated with steady state values *further* from equilbrium). $\theta_0 = 45^\circ$

Another instructive case to examine is the relaxation of the droplet under the constraint of constant volume when the contact angle is initiated at a non-equilibrium value (Fig. 6.3). We change the reference length scale to be the final radius $\lim_{t\to\infty} R^* = 1$, and choose the initial radius $R^*\left(t=0\right)=R_i^*$ according to,

$$R_i^{*3} = \frac{\left(2-\cos\theta_0\right)\left(1+\cos\theta_0\right)^2}{\left(2-\cos\theta_i\right)\left(1+\cos\theta_i\right)^2} \quad . \qquad [6.5]$$

While there is only one natural time scale in the system of equations, we find from Fig. 6.3 that the relaxation time depends on the initial condition. We can gain additional insights into this behavior by linearizing the radius of curvature and contact angle about their initial conditions. To do so, the forms

$$\begin{aligned} R\left(t\right) &\sim R_i + \delta R\left(t\right) \\ \theta\left(t\right) &\sim \theta_i + \delta R\left(t\right) \end{aligned} \qquad [6.6]$$

are assumed and substituted into [6.3] and only the first order terms retained. The linear system is as follows

$$\begin{aligned} \delta\dot{R}\left(2\pi R_i^2 + 3\pi R_i^2\cos\theta_i - \pi R_i^2\cos^3\theta_i\right) - \pi R_i^3\sin^3\theta_i\delta\dot{\theta} &= 0 \\ \delta\dot{R}\sin\theta_i + \delta\dot{\theta}\left(\sin\theta_i + R_i\cos\theta_i\right) &= \cos\theta_i - \cos\theta_0 \end{aligned} \quad . \qquad [6.7]$$

The system allows us to show, formally, that the early exponential behavior depends on the initial conditions; the two time constants are

$$\lambda_1 = \frac{-32\cos^9\frac{\theta_i}{2}\left(\cos\theta_i - 2\right)\sec\theta_i \sin\frac{\theta_i}{2}}{R_i\begin{pmatrix}-\cos\theta_i - 3\cos^2\theta_i \\ +\cos^4\theta_i - \sin^4\theta_i\end{pmatrix}\begin{pmatrix}2+3\cos\theta_i - \cos^3\theta_i \\ +\sin^3\theta_i + \tan\theta_i\end{pmatrix}} \qquad [6.8]$$

$$\lambda_2 = 0$$

A comparison of the contact angle evolution between the linearized model and the full model is plotted in Fig. 6.4A for two initial contact angles; the model shows good agreement at early times as one would expect. The full spectrum of relaxation times as a function of initial contact angle θ_i for different equilibrium contact angles $\theta_0 = \left\{45^\circ, 90^\circ, 135^\circ\right\}$ is shown in Fig. 6.4. B. At the extremes $\theta_i = 0, \pi$, we see that the linear model fails to account for the dynamics indicating that higher order terms would need to be included to model early time dynamics for those initial conditions.

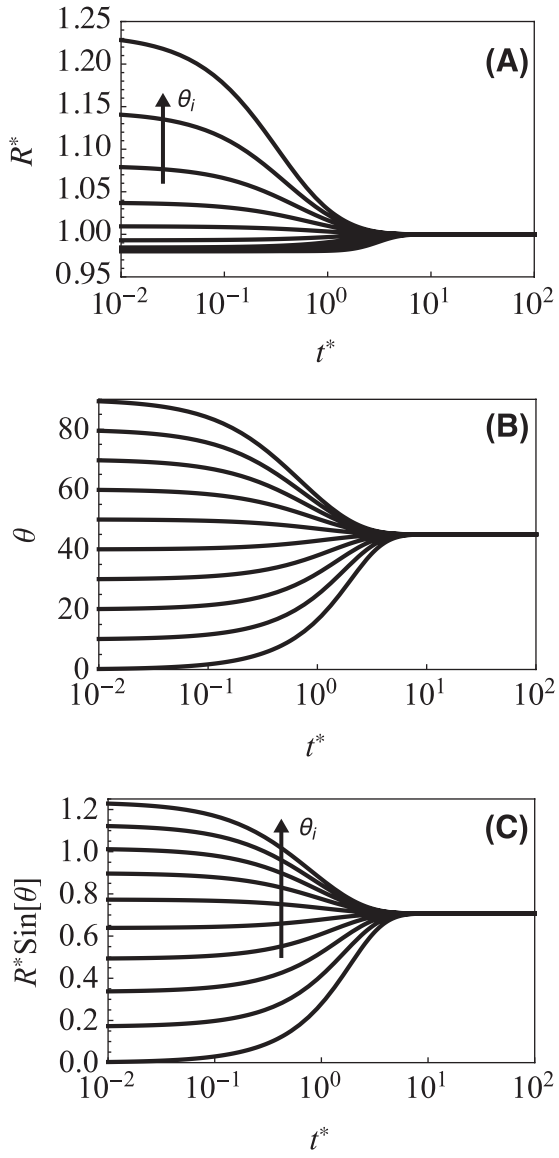

Fig. 6.3: (A) radius of curvature, (B) contact angle and (C) contact line radius of an incompressible droplet initiated at a non-equilibrium contact angle and relaxing toward its equilbrium state while conserving volume, $V_0^* = 0$. All droplets are given the same initial volume such that the final radius of curvature of the equiliberated droplet $R^* = 1$. $\theta_0 = 45^\circ$.

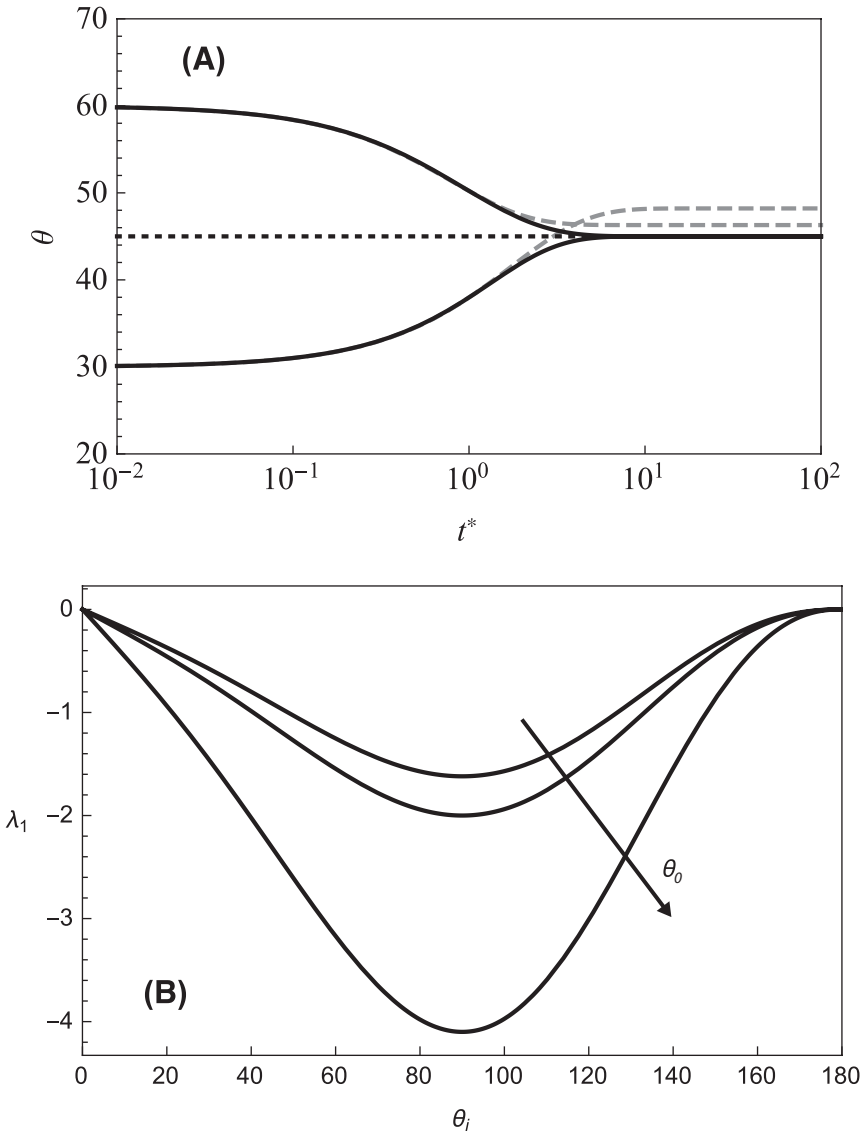

Fig. 6.4: (A) Contact angle evolution of a droplet beginning at a non-equilibrium contact angle while conserving volume $V_0^* = 0$. Trends compare full model (black line) and linearized model (eqn. [6.7]) (gray dashed line) for $\theta_i = \{30^\circ, 60^\circ\}$ with $\theta_0 = 45^\circ$. (B) Relaxation time constant λ_1 (eqn. [6.8]) as a function of initial contact angle for $\theta_0 = \{45^\circ, 90^\circ, 135^\circ\}$.

6.3. Compressible and Soluble

The case of a compressible bubble that is partially soluble in the surrounding fluid is now derived. Beginning with the ideal gas equation of state $PV = nBT$ and taking the time derivative yields $\dot{P}V + P\dot{V} = \dot{n}BT$, where B [mol J^-1 K^-1] is the universal gas constant, T [K] is the temperature, n [mol] is the total number of moles in the gas. The pressure P of the gas inside the bubble is given by the surrounding pressure plus the Laplace-pressure $P = P_\infty + 2/R$.

If we assume a spherically symmetric diffusion field (that is, we ignore the impact of the substrate), then the molar flux per unit area is given by the long-time Epstein-Plesset[20] equation

$$D\left.\frac{\partial C}{\partial r}\right|_{r=R} = D\left(C_\infty - HP_\infty - H\frac{2\gamma}{R}\right)\left(\frac{1}{R}\right). \qquad [6.9]$$

The solution excludes convection and assumes that the boundary conditions are steady with time, as was justified in Chapter 4. Integrating the flux along the exposed portion of the sphere gives a total molar flux of

$$\dot{n} = 2\pi R^2\left(1-\cos\theta\right)D\left(C_\infty - HP_\infty - H\frac{2\gamma}{R}\right)\left(\frac{1}{R}\right). \qquad [6.10]$$

However, this will tend to overestimate the mass flow when $\theta_0 < \pi/2$ and underestimate it when $\theta_0 > \pi/2$. To find the correction, an auxiliary finite element simulation is performed that includes the no-flux condition at the surface of the substrate, a sample of the mesh used is shown in Fig. 6.5.

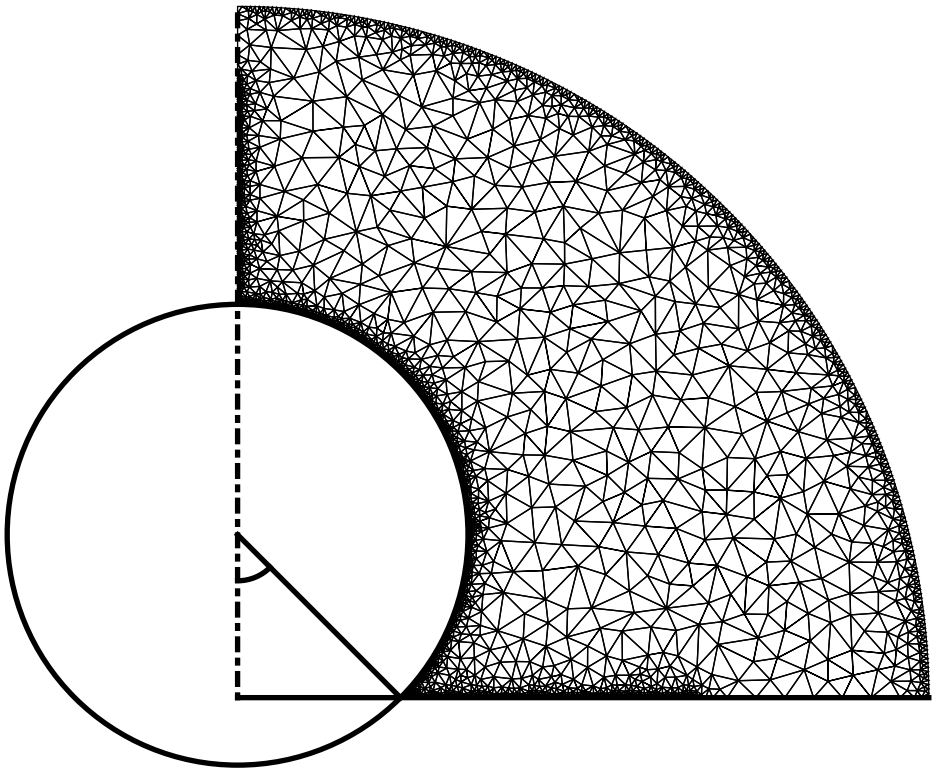

Fig. 6.5: A sample of the mesh (with $\theta_0 = 45^\circ$) used for the finite element calculation of the total mass flux into the bubble plotted in Fig. 6.6. The bubble has unit radius, the actual domain size used was 50 times the size of the bubble.

The dimensionless mass flow of the spherically symmetric analytical case $\dot{n}/\left(DR\Delta C\right) = 4\pi\left(1+\cos\theta_0\right)$ (black line) is compared to the FEM solution (black points). The numerical points are used to create a smooth interpolation function $f\left(\theta_0\right)$, which will be implemented as follows

$$\dot{n} = f\left(\theta_0\right) RD\left(C_\infty - HP_\infty - H\frac{2\gamma}{R}\right). \qquad [6.11]$$

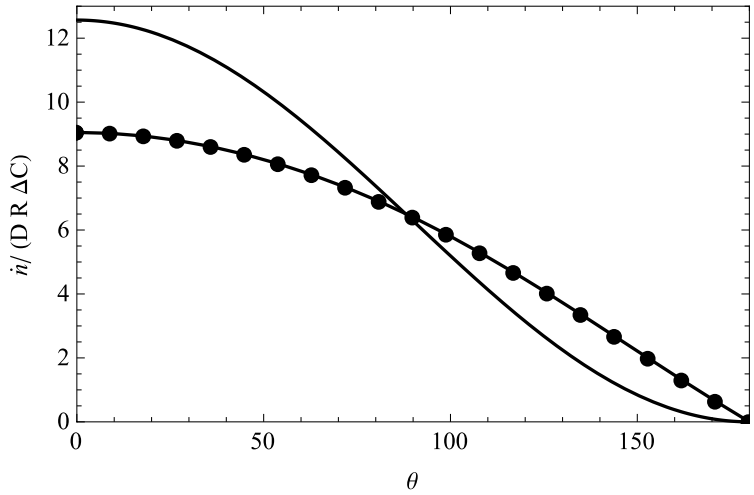

Fig. 6.6: Comparison of the (dimensionless) mass flow into a sessile bubble as a function of contact angle between a spherically symmetric solute field (black line) and a more realistic calculated using the finite element method (black points). Note that when the bubble is a perfect hemisphere ($\theta = 90^{\circ}$) the two methods agree due to symmetry.

Substituting eqn. [6.11] into the ideal gas equation along with [6.2] closes the system. We non-dimensionalize the system using, again, the initial radius as the length scale $R^* = R/R_0$ but this time the time scale associated with diffusion $t^* = tD/R_0^2$.

$$\left[\left(-\dot{R}^*\frac{2}{R^{*2}}\right)V^* + \left(P^*_{\infty} + \frac{2}{R^*}\right)\dot{V}^*\right] = \left(HBT\right)R^{*2}f\left(\theta_0\right)\left(C^*_{\infty} - P^*_{\infty} - \frac{2}{R^*}\right), \qquad [6.12]$$

and

$$\dot{R}\sin\theta + R\dot{\theta}\cos\theta = \Omega_2\left(\cos\theta - \cos\theta_0\right). \qquad [6.13]$$

This introduces the following dimensionless variables and quantities:

$$\Omega_1 = HBT\,,\Omega_2 = \frac{\gamma R_0}{\eta_{CL} D}\,,C_\infty^* = \frac{C_\infty R_0}{H\gamma}\,,P_\infty^* = \frac{P_\infty R_0}{\gamma} \qquad [6.14]$$

The group Ω_2 quantifies the importance of contact line friction and can be understood as a ratio of velocities. In the limit as $\Omega_2 \to \infty$, $\dot{\theta} \to 0$ and the equilibrium contact angle is maintained at all times. In the opposite limit $\Omega_2 \to 0$, the contact line seizes completely throughout the growth. We can see quite readily from this group that contact line dissipation will be more important at small scales or early times.

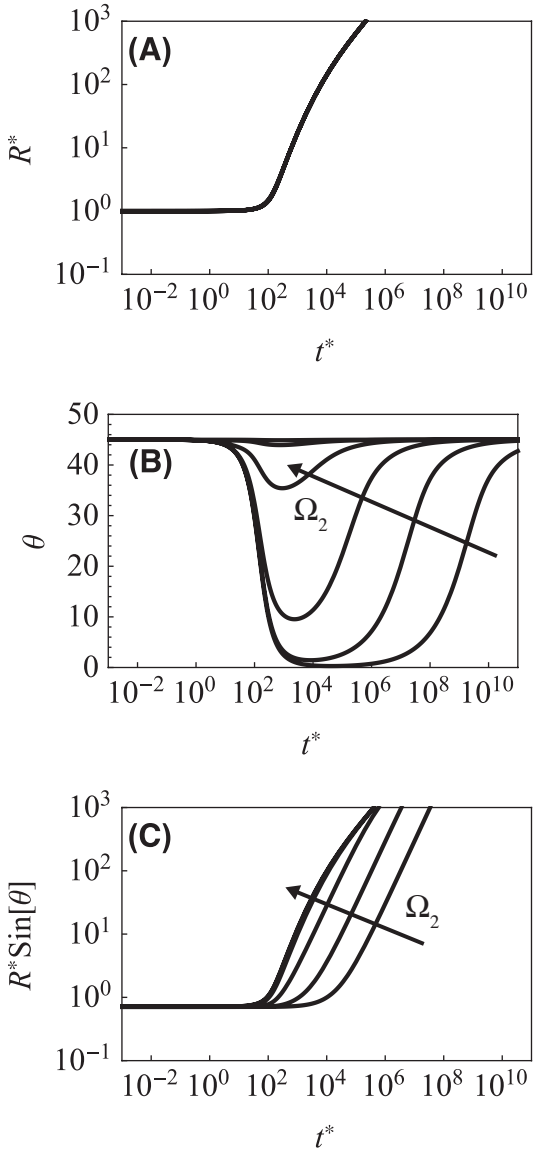

Fig. 6.7: (A) radius of curvature, (B) contact angle and (C) contact line radius of a shrinking bubble $\Omega_2 = \left\{10^{-4}, 10^{-3}, 10^{-2}, 10^{-1}, 1, 10\right\}$. $\alpha = 1.1$, $P_\infty^* = 0.01$ and $\Omega_1 = 0.019$.

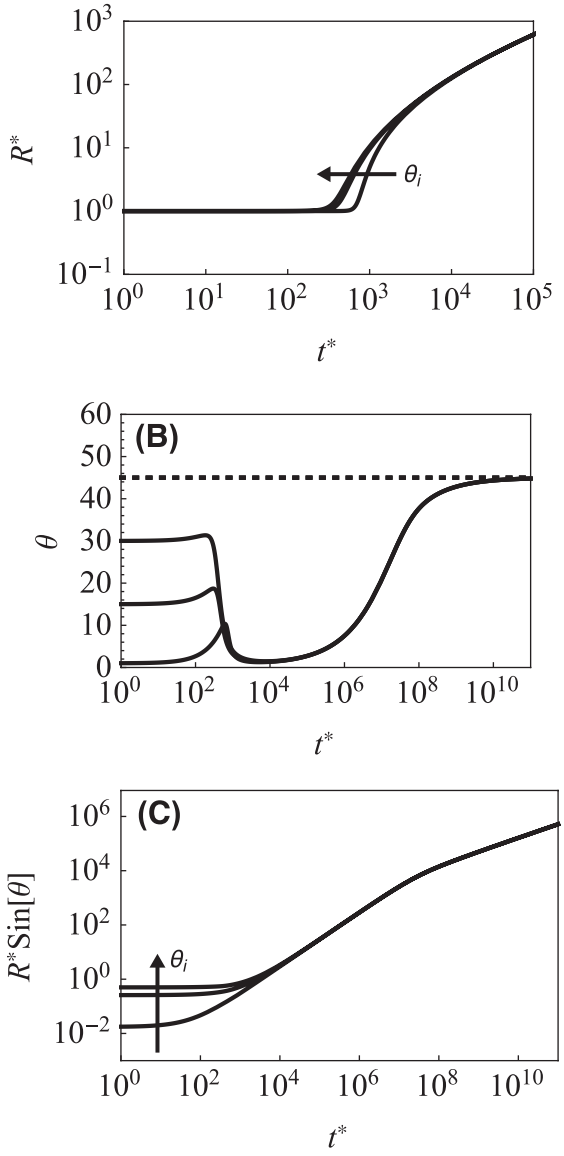

Fig. 6.8: (A) radius of curvature, (B) contact angle and (C) contact line radius of a bubble whose surface concentration matches the concentration in the solute initially $\alpha = 1$, but begins with a non-equilibrium contact angle, $\theta(0) = \{1^\circ, 15^\circ, 30^\circ\}$. The bubbles grow; however, the contact angle evolution is non-monotonic., $\theta_0 = 45^\circ$, $P_\infty = 0.01$, $\Omega_1 = 0.019$ and $\Omega_2 = 10^{-3}$.

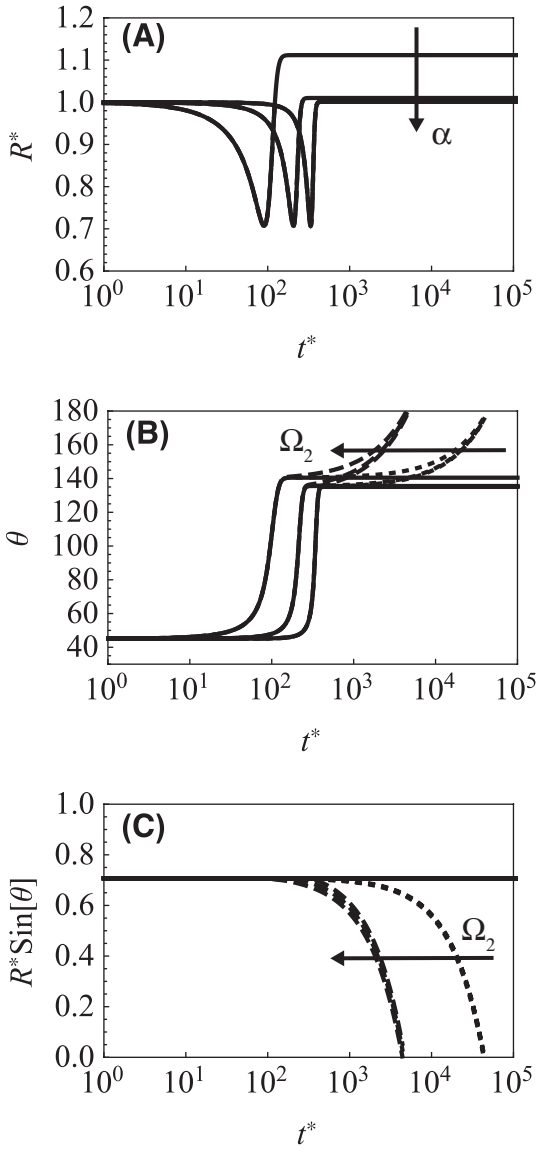

Fig. 6.9: (A) radius of curvature, (B) contact angle and (C) contact line radius of a shrinking bubble $\alpha = \{0.999, 0.99, 0.9\}$. Solid, dotted, and dashed lines are, respectively $\Omega_2 \to 0$, $\Omega_2 = 10^{-5}$ and $\Omega_2 = 10^{-4}$. $P_\infty^* = 0.01$ and $\Omega_1 = 0.019$.

We now choose to model a specific physical situation that has been realized experimentally by another group: the growth of a compressible and soluble bubble due to a diffusion limited growth following sudden change in super-saturation created by dropping the pressure. Like the nanobubble analysis, the inertial and viscous stages of the

growth are ignored and we view the problem as an instantaneous change in the super-saturation of dissolved gas.

In order to compare our results to the experimental work of Li *et al.*[105], we assume that the mass transfer driven growth begins with the bubble having a radius of curvature of $R_0 = 15[\mu m]$. In order to estimate the super-saturation value (which is not given in their paper), we assume that prior to the pressure drop that the bubble was at mechanical and chemical equilibrium with the surroundings. For the sake of making the problem self-consistent, we find the radius of the bubble prior to pressure expansion in order to find the super saturation that corresponds to its surface concentration by solving for R'

$$R'^3\left(P'_\infty + \frac{2\gamma}{R'}\right) = R_0^3\left(P_\infty + \frac{2\gamma}{R_0}\right). \qquad [6.15]$$

For $P'_\infty = 101$ [kPa] , $P_\infty = 35$ [kPa], $R_0 = 15$ [μm], and $\gamma = 70$ [mN m^{-1}], $R' \sim 11$ [μm]. If the pre-expansion bubble of this radius is at equilibrium, the bulk concentration of dissolved gas must be $C_\infty = H\left(P'_\infty + 2\gamma / R'\right) = 0.68\left[\text{mol m}^{-3}\right]$ for $H = 6.06e-6\left[\text{mol m}^{-3}\text{ Pa}\right]$. However, ultimately we find that $C_\infty = 0.44\left[\text{mol m}^{-3}\right]$ gives a better fit with the experimental data; this simply suggests that the initial assumption of chemical equilibrium was incorrect. Fig. 6.10 compares the evolution of the radius of curvature (A) and contact angle (B).

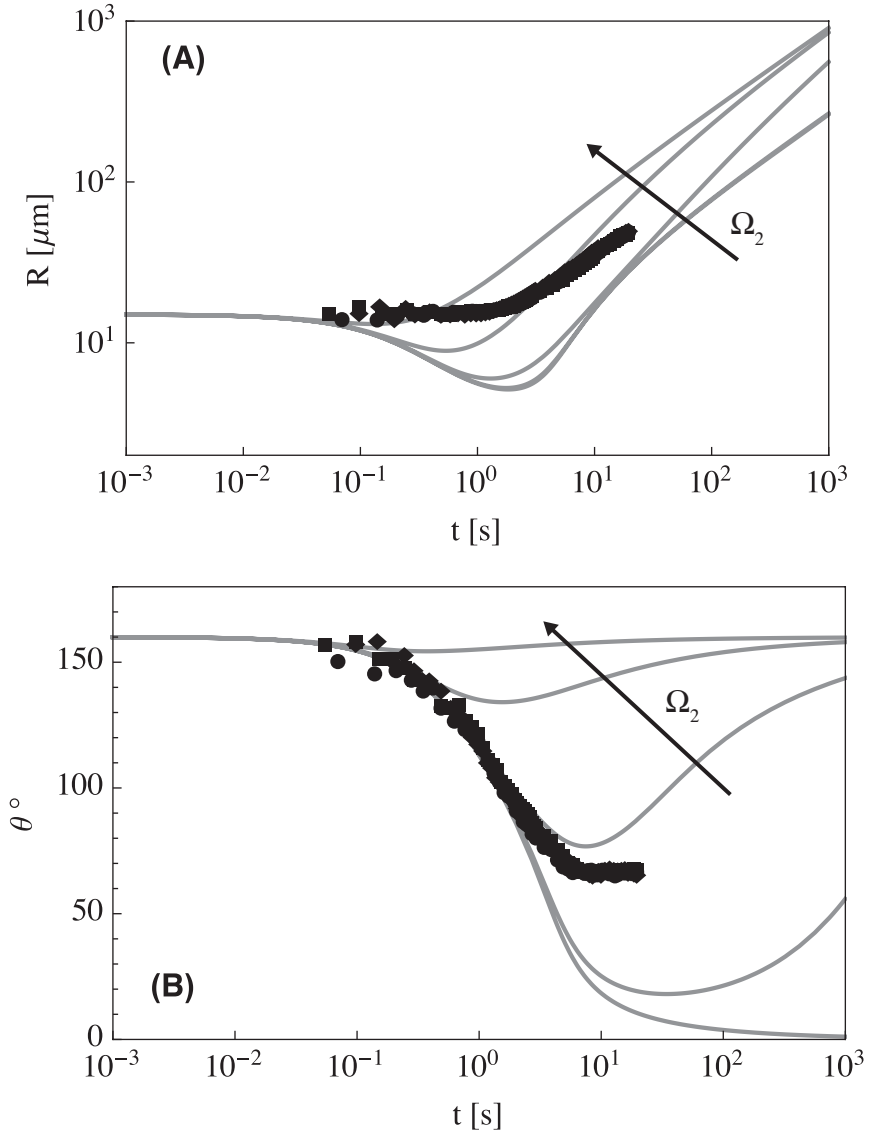

Fig. 6.10: (A) radius of curvature, (B) contact angle comparison between theory mass transfer driven theory and the experimental work of Li *et al.*[105]
$\Omega_2 = \{1, 10^{-1}, 10^{-2}, 10^{-3}, 0\}$, $\theta_0 = 160^\circ$.

In order the Blake-Haynes model to give a good agreement at early times, an equilibrium contact angle $\theta_0 = 160^\circ$ was used. However, the model also predicts a relaxation back towards this contact angle as the growth rate slows; this is in contast to the experimental data in which late stage growth proceeds with nearly constant contact angle.

6.4. Conclusion

A simple model of a sessile bubble growing and shrinking on a substrate with contact line dissipation is considered. Like previous chapters, when volume is prescribed and grows as the dimension of the system $V \propto t^3$, growth becomes self-similar. However, unlike the doubly-confined (Hele-Shaw) cases considered earlier, the evolution of the radius of curvature when diffusion drives growth does not deviate from Epstein-Plesset theory. Additionally, a comparison with the experimental data of Li *et al.* [105] is conducted. In their experiment, Li *et al.* show that the contact angle saturates at a constant value. In contrast, the Blake-Haynes model predicts a relaxation back towards the equilibrium, indicating that other physics at the contact line are present, such as contact angle hysteresis.

Chapter 7. Conclusions and Outlook

Droplet and bubble geometries in the zero Capillary and Bond number limits have been examined experimentally and theoretically with different substrate geometries. The low Capillary number limit is an important one in the maturing field of lab-on-chip technologies and other devices in which interface behavior at the sub-micron scale dominates performance such as multi-phase heat exchangers and gas-producing catalytic processes. Capillary driven assembly of micro- and nano- particles also occur in the low Capillary number regime.

In Chapter 2, the shape of axisymmetric drops enclosing a slender, ellipsoidal particle as a function of drop volume and contact angle was explored. Interface geometries satisfying contact angle and volume constraints were identified by finding unduloidal solutions (described by elliptical integrals). Solutions were compared to a numerical technique that found interfaces by minimizing the free energy of a discretized surface. The theory revealed that there is a maximum volume that can be supported by pinned unduloidal morphologies on an ellipsoidal substrate, that multiple stationary states exist, and that there is the possibility of hysteretic encapsulation behavior. This investigation was, however, restricted to axisymmetric (or, colloquially, "barrel") states. It has been established that barrel interfaces, when attached to a *uniform* cylindrical substrate, are unstable for some combinations of contact angle and volume, and give way to axisymmetric "clam-shell" geometries [36]. This situation is likely to persist for ellipsoidal particles as well. However, the phase space will be controlled by not just volume and contact angle, but aspect ratio as well. In addition to the barrel and clam-shell states encountered by Eral *et al.*, the fully engulfed state will have to be considered

as well. Finding the stability limit of the barrel state can be accomplished quasi-analytically using a technique developed by Brinkmann *et al.* [35]. The geometry and stability of the non-axisymmetric clam-shell state will need to be accomplished using a numerical method. While Surface Evolver is well equipped for this task, it should be noted that by default it utilizes gradient descent methods that are unlikely to find saddle points. Care must be exercised when choosing the search method; fortunately, documentation on enabling these features is thorough.

Chapter 3 discussed electron microscopy observations of radiolysis-induced bubble growth and anomalous migration in a liquid cell originally made by Joseph M. Grogan[17], [70], [107]. Ideal and non-ideal filling situations of the nanoaquarium are discussed; in particular, adhesion between the silicon-nitride membranes of the liquid cell are shown to produce both non-uniformities and levels of confinement smaller than the nominal 200nm spacing. The chapter concludes that, most likely, motion is driven by confinement gradients. Because many bubbles appeared circular and were growing and translating at ultra-low Capillary and Bond numbers, it was hypothesized that perhaps their geometry was spherical. By assuming a locally wedge-shaped conduit, a simple relationship between radial growth rate and translational velocity was established that assumed such geometry. It was then shown that the experimental data did not follow this prescription. This lead to the conclusion that while the bubbles appeared circular, they were not simply the projection of spherical shapes and further, that additional forces must be at play.

Scaling analysis in Chapter 4 revealed that bulk viscous and inertial stresses should not significantly impact bubble growth or movement. A 2D bubble model of

diffusion driven growth of a bubble in a wedge was introduced that included contact line resistance while omitting bulk viscous dissipation. It predicts continuous transport of a disperse phase in the absence of outside forces; all work is provided by the concentration gradient and subsequently dissipated at the contact line and in the creation of additional interface. By first exploring a bubble slug with a prescribed volume (per unit depth) $V \propto t^2$, it was shown that when contact line resistance is present, curvature evolution is non-monotonic. Additionally, it was found that when the volume is forced to increase in this way, as $t \to \infty$ the contact angles saturate to non-equilibrium values that permit constant velocity and growth rate. When mass transfer by diffusion is included and Henry's law used to determine the surface concentration, the model predicts growth rates orders of magnitude lower than the Epstein-Plesset theory for the same super-saturation conditions because the curvature *increases* initially, *reducing* mass transfer by diffusion. While the model demonstrates the strong impact of the contact line on growth and migration dynamics, it cannot answer more subtle questions about bubble geometry. Chapter 3 showed tear-drop shaped bubbles in addition to circular ones and the question remained whether the Blake-Haynes relationship alone could yield such geometries.

To answer this question, a quasi-3D model was developed and presented in Chapter 5. The method leveraged not only the zero Capillary and Bond number limits but also assumed small opening angles for the wedge geometry and only weakly non-circular contact lines. These assumptions allowed for a pseudo-spectral scheme to be implemented. Analogously to the 2D case, it was found that prescribing a volume $V \propto t^3$ allowed for self-similar growth in the long time limit. Qualitatively, the radial growth rate and velocities were similar to those found for the 2D model when mass

transfer driven growth was considered. Compellingly, when the contact line was partially immobilized, bubble geometries very reminiscent of the teardrop shaped bubbles described in Chapter 3 experiment were found. Further, it was not possible to achieve these same geometries without partial pinning. We can conclude that while confinement, small wedge angles, and the Blake-Haynes model are sufficient at explaining reduced growth compared to free floating bubbles, they are not enough to alone explain more exotic geometries. Further, the theory developed here shows that the amount to which the contact line of partially pinned bubbles and droplets depart from a circular geometry is determined by how rapidly they grow (Fig. 5.8); in other words their geometry is dynamically created because of contact line dissipation. This is in contrast to the teardrop geometries observed and predicted by Dangla *et al.*[83] that are always quasi-static; in the their experiments, the continuous phase completely wetted the substrate and they note that droplets depart at the same size regardless of the volumetric flow. Dynamically selected departure geometries could have important engineering applications.

However, there remain important questions regarding the physics governing bubble departure itself. The data demonstrates an apparent critical size after which the bubble undergoes a rapid change in geometry and velocity. The question is whether this departure happens because an instability (as demonstrated by Dangla *et al.*) develops or is the result of the rear contact line achieving a critical contact angle (i.e. contact angle hysteresis). In some cases, when bubbles depart they leave a small remnant, indicating that the instability may be the catalyst for detachment; in other cases, the departure appears to be complete, supporting a contact angle hysteresis hypothesis. It may be that both mechanisms facilitate departure at similar radii, making them difficult to

differentiate. In either case, experiments with controlled nucleation sites and/or pinning sites could facilitate a greater understanding of this phenomenon. Additional theoretical investigations to comparing departure size for the different mechanisms may also be in order.

More broadly, the theoretical framework developed in Chapter 5 to study bubbles is powerful, and may be used to model the movement of bubbles or droplets in channels with geometry that is more complex than a simple wedge, or is chemically patterned such that the equilibrium contact angle or contact line viscosity vary with position. In this thesis, it was assumed that radiolysis was the dominant contributor to bubble growth; applying the same framework to consider vapor bubbles growing due to phase change is also possible and may be relevant to those studying phase change at the nanoscale using liquid cells. The technique has utility because it explicitly tracks the contact angle distribution. However, many simplifications were made in order to implement the model as a system of differential equations. If a solution method other than the spectral method used here was applied to the problem, it would be possible to include additional physics such as contact angle hysteresis. One can also envision implementing higher order corrections to the Young-Laplace equation[7], [83] to achieve more realistic geometries as well.

Chapter 6 applies the techniques developed in Chapter 4 and 5 to a slightly simpler problem but technologically important one, the growth and dissolution of a sessile bubble. Interestingly, while contact line dissipation does impact contact angle, the overall impact on curvature is minimal during; growth the model predicts growth very similar to Epstein-Plesset theory. A greater departure from Epstein-Plesset theory is seen

when a dissolving bubble is considered; in this case contact line resistance is able to temporarily prevent the run-away dissolution of bubbles. The framework of the problem is simple enough that it would be straightforward to implement physical or chemical heterogeneities into the model to gain insights into how such patterns might be used to tailor boiling and catalytic processes.

This thesis focused on but one of many fluid dynamical phenomena that have been observed in the nanoaquarium liquid cell. The degree to which the imaging beam interacts with liquid samples is still being studied, but there are a few observations that deserve a closer look in the future. First, Fig. 7.1 shows a $\sim 10 \mu m$ bubble oscillating in the nanoaquarium observed in a SEM operating in transmission mode. While the slow scan rate of the SEM is typically undesirable, in this case it permits us to estimate the frequency of the bubble's oscillations to be about 150 Hz. The frequency is estimated by noting that it takes 300 milliseconds to scan the entire frame. At the image's original size, it was 900 pixels in height with each jump in the interface occurring every ~20 pixels or every 6.7 milliseconds. These oscillations are interesting because they are asymmetric in time (note saw-tooth pattern in Fig. 7.1) and are occurring at low Weber numbers, meaning that they are not inertial in nature. We hypothesize that the dry portion of the membrane is charging up because of an interaction with the beam. This creates a region of high electric field that draws the interface towards it, compressing the bubble. Alternatively (or additionally), the charging could be increasing the wettability of the membrane, drawing liquid in. In either case, once the liquid has wet the area, it provides a means of discharging the membrane. Developing a model that incorporates charging and

discharging rates and trying to match the experimental results could be a way of furthering our understanding of beam-liquid interactions.

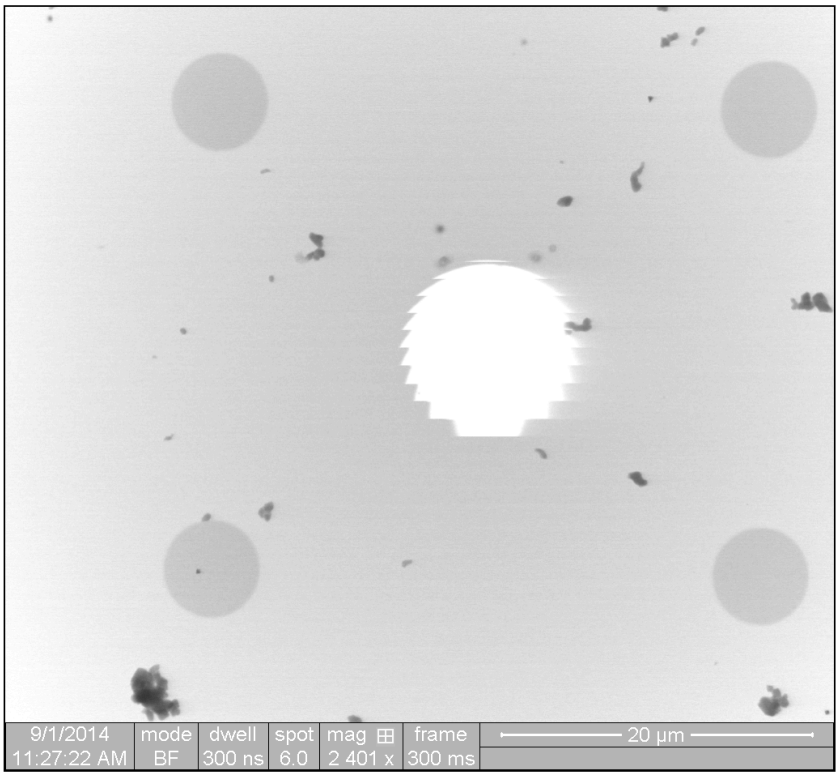

Fig. 7.1: An SEM micrograph of a large bubble oscillating in the nanoaquarium liquid cell. The bubble is oscillating at approximatley 100 Hz. Because of the slow scan speed of the microscope, the bubble oscillates several times while the image is captured.

When using the nanoaquarium, a common experimental situation that arises is the presence of a large bubble in the viewing window. Such bubbles are typically introduced in the nanoaquarium during filling but cannot be eliminated and expand to fill the viewing area when the vacuum chamber of the microscope is evacuated and the pressure drops. On several occasions it has been observed that when an area within such a bubble is interrogated at high magnification, spontaneous liquid build up occurs, Fig. 7.2. However, the liquid does not build up uniformly: at first “droplets” appear at a

characteristic spacing from each other, Fig. 7.2B, and eventually grow and merge to create a liquid area with extents that match the region view at high magnification, Fig. 7.2C. The non-uniform interface, Fig. 7.2B, that precedes the final rectangular-shaped film is highly reminiscent of those predicted by the stability analysis of Verma on thin liquid films subjected to high electric field [108]. The phenomenon suggests that a thin film persists along the silicon-nitride membranes and that the beam locally alters the substrate in such a way as to attract a thicker film. It is interesting to note that the instability does not appear to persist in the interrogated region (dashed line in Fig. 7.2) once the film becomes "thick," (perhaps thick enough to wet both membranes) but does remain outside of that region; note the droplets outside the rectangular region exposed to high magnification, Fig. 7.2C. This, perhaps, suggests that the instability only persists over a range of film thicknesses. Applying the theory of Verma could provide a means to estimate the film thickness and/or the amount of charging that takes place the membranes. Such a characterization would have applications in future liquid-cell experiments, particularly those in the nanoaquarium.

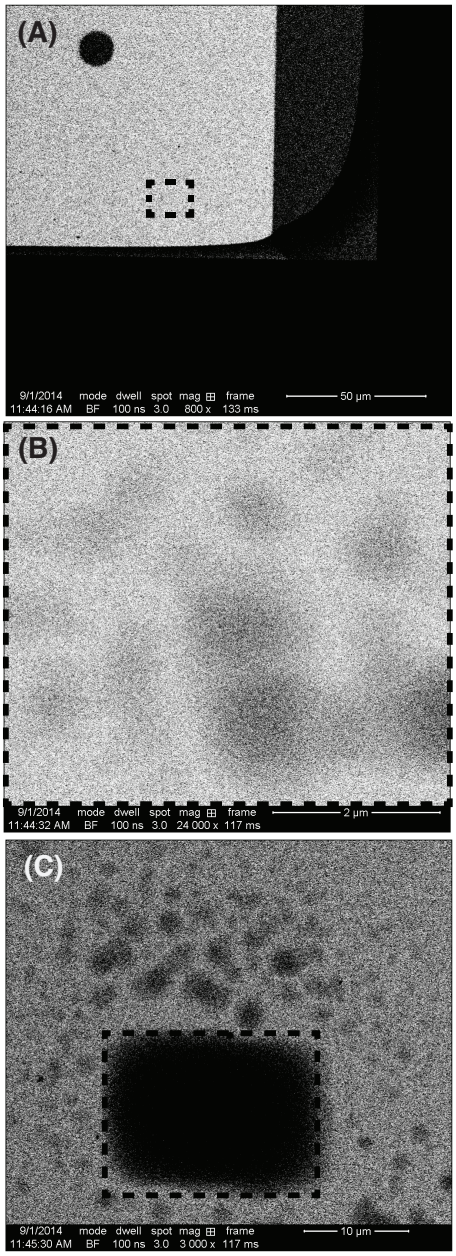

Fig. 7.2: A series of SEM images depicting how temporarily increases the magnification on an ostensibly dry region of the nanoaquarium can promote local film thickening. The liquid does not build up uniformly and undergoes some form of instability with a characteristic wavelength.

Chapter 8. Appendix

8.1. Drop Shape Calculation Using Numerical Energy Minimization

To enable the calculation of the drop shape under conditions of non-constant curvature (i.e., when one wishes to account for Van der Waals forces), we developed an algorithm based on the minimization of the free energy. In this section, we briefly describe the energy minimization algorithm and verify its performance by comparing its predictions with unduloid-based solutions.

We define the functional

$$F = E_{\alpha\beta} + E_{\alpha\sigma} + E_{\beta\sigma} + E_v \qquad [8.1]$$

where

$$E_{\alpha\beta} = \gamma_{\alpha\beta} 2\pi \int_{\phi_1}^{\frac{\pi}{2}} \rho_{\alpha\beta} \sqrt{\left(\frac{\mathrm{d}\rho_{\alpha\beta}}{\mathrm{d}\phi}\right)^2 + \rho_{\alpha\beta}^2}\, \sin\phi\, \mathrm{d}\phi \qquad [8.2]$$

is the surface energy of the droplet-continuous phase ($\alpha\beta$) interface;

$$E_{\alpha\sigma} = \gamma_{\alpha\sigma} 2\pi \int_{\phi_1}^{\frac{\pi}{2}} \rho_{\alpha\sigma} \sqrt{\left(\frac{\mathrm{d}\rho_{\alpha\sigma}}{\mathrm{d}\phi}\right)^2 + \rho_{\alpha\sigma}^2}\, \sin\phi\, \mathrm{d}\phi \qquad [8.3]$$

is the surface energy of the droplet-solid ($\alpha\sigma$) interface;

$$E_{\beta\sigma} = \gamma_{\beta\sigma} 2\pi \int_0^{\phi_1} \rho_{\beta\sigma} \sqrt{\left(\frac{\mathrm{d}\rho_{\beta\sigma}}{\mathrm{d}\phi}\right)^2 + \rho_{\beta\sigma}^2} \sin\phi \,\mathrm{d}\phi \qquad [8.4]$$

is the surface energy of the continuous phase-solid ($\beta\sigma$) interface; and

$$E_v = \lambda \left[\frac{2\pi}{3} \int_{\phi_1}^{\frac{\pi}{2}} (\rho_{\alpha\beta}^3 - \rho_{\alpha\sigma}^3) \sin\phi \,\mathrm{d}\phi - \frac{V}{2} \right] \qquad [8.5]$$

is the volume constraint. All are written in spherical coordinates defined in Fig. 3. The volume constraint is enforced through the Lagrange multiplier λ that corresponds to the static (Laplace) pressure in α. In all the above equations, integration about the azimuthal angle has already been carried out. The task is to determine the shape of the ($\alpha\beta$) interface $\rho_{\alpha\beta}(\phi)$ and the position of the contact line ϕ_1 that minimizes *F*.

Although the contact angle θ does not appear explicitly in equations S1-S5, the state that minimizes *F* satisfies Young's equation. To see this, we consider one of the essential conditions of the stationary state:

$$\frac{\partial F}{\partial \phi_1} = 0. \qquad [8.6]$$

Since $\partial E_V / \partial \phi_1 = 0$, we have

$$\frac{\partial E_{\alpha\beta}}{\partial \phi_1} + \frac{\partial E_{\alpha\sigma}}{\partial \phi_1} + \frac{\partial E_{\beta\sigma}}{\partial \phi_1} = 0. \qquad [8.7]$$

Further, since $\rho_e \equiv \rho_{\beta\sigma}(\phi_1) = \rho_{\alpha\sigma}(\phi_1) = \rho_{\alpha\beta}(\phi_1)$, we have:

$$\gamma_{\alpha\sigma} - \gamma_{\beta\sigma} + \frac{\left.\sqrt{\left(\frac{\mathrm{d}\rho_{\alpha\beta}}{\mathrm{d}\phi}\right)^2 + \rho_e^2}\right|_{\phi_1}}{\left.\sqrt{\left(\frac{\mathrm{d}\rho_e}{\mathrm{d}\phi}\right)^2 + \rho_e^2}\right|_{\phi_1}} \gamma_{\alpha\beta} = 0. \qquad [8.8]$$

The term in front of $\gamma_{\alpha\beta}$ is a ratio of arc-lengths and can be replaced with the cosine of the contact angle to retrieve the Young's equation:

$$\gamma_{\alpha\sigma} - \gamma_{\beta\sigma} + \gamma_{\alpha\beta}\cos\theta = 0. \qquad [8.9]$$

To minimize *F*, we resort to numerical techniques. The interface αβ is divided into *N* segments each having an arc length *l* (see Fig. 3). *l* is not known *a priori* and must be determined as part of the solution. The restriction of uniform segments is enforced with an additional pseudo-energy term:

$$E_l = \sum_{n=1}^{N-1} \eta_n \left[\left(\rho_{\alpha\beta;n+1} - \rho_{\alpha\beta;n} \right)^2 + \rho_{\alpha\beta;n} \left(\phi_{n+1} - \phi_n \right)^2 - l^2 \right]. \qquad [8.10]$$

The above constraint prevents the nodes from aggregating in a narrow region. In Fig. 2.3, nodes are labeled with hollow circles and the nth node is highlighted with a solid circle. Node *n*=1 corresponds with the contact line. At the contact line, ϕ_1 is to be determined while ρ_1 is available from the particle's geometry. The left-right symmetry is enforced by fixing $\phi_N = \pi/2$. The discretized equations are:

$$E_v = \lambda \left\{ \frac{\pi}{3} \sum_{n=1}^{N-1} \left[\begin{array}{l} \sin\phi_{n+1} \left(\rho_{\alpha\beta;n+1}^3 - \rho_{\alpha\sigma;n+1}^3 \right) \\ + \sin\phi_n \left(\rho_{\alpha\beta;n}^3 - \rho_{\alpha\sigma;n}^3 \right) \end{array} \right] \left(\phi_{n+1} - \phi_n \right) - \frac{V}{2} \right\} \qquad [8.11]$$

and

$$E_{\alpha\beta} = 2\pi\gamma_{\alpha\beta}\sum_{n=1}^{N-1} l\rho_{\alpha\beta;n}\sin\phi_n . \qquad [8.12]$$

We find the stationary state by setting the derivatives of the energy functional with respect to all degrees of freedom **x** to zero.

$$\frac{\partial F}{\partial \mathbf{x}} = 0 . \qquad [8.13]$$

In the above,

$$\mathbf{x} = \left[(\rho_2, \rho_3 \ldots \rho_N), (\phi_1, \phi_2 \ldots \phi_{N-1}), (\eta_1, \eta_2 \ldots \eta_{N-1}), \lambda, l\right]. \qquad [8.14]$$

We solve equation S13 with the Newton-Raphson method

$$\mathbf{x}^{(k+1)} = \mathbf{x}^{(k)} - \left[\left(\frac{\partial^2 F}{\partial \mathbf{x}\partial \mathbf{x}}\right)^{-1}\right]^{(k)} \frac{\partial F}{\partial \mathbf{x}}^{(k)} . \qquad [8.15]$$

In the above, the superscript denotes the k^{th} iterate. The first order derivatives and Jacobian matrix were determined analytically. The corresponding expressions are lengthy and therefore not reproduced here.

Typically $N \sim 100$ nodes were sufficient to achieve grid-independence. The energy minimization code was verified by reproducing known solutions for the cylindrical fiber wetting problem [S1]. Fig. S1A compares the energy-minimization solution (hollow circles) with the analytical solution (solid line) when $\theta = 45^{\circ}$. Fig. 8.1.B depicts the relative discrepancy between the analytical solution and the energy minimization solution for the position of the droplet apex (squares) and droplet pinning point (circles) as functions of the number of nodes (N). When N>80, the error is smaller than 1%.

Next, we applied the energy minimization algorithm to determine the shape of a drop partially engulfing an ellipsoidal particle. Fig. 8.2 A and B depict, respectively, z_1^* and r_2^* as functions of the volume as determined by the energy minimization method (solid circles) and the unduloid solution (solid lines). ε=5 and $\theta = 90^\circ$. Both solution methods produced nearly identical results. To illustrate the convexity of the energy functional, Fig. 8.3 depicts the free energy of a fixed volume drop as a function of the pinning line position ϕ_1 for various contact angles.

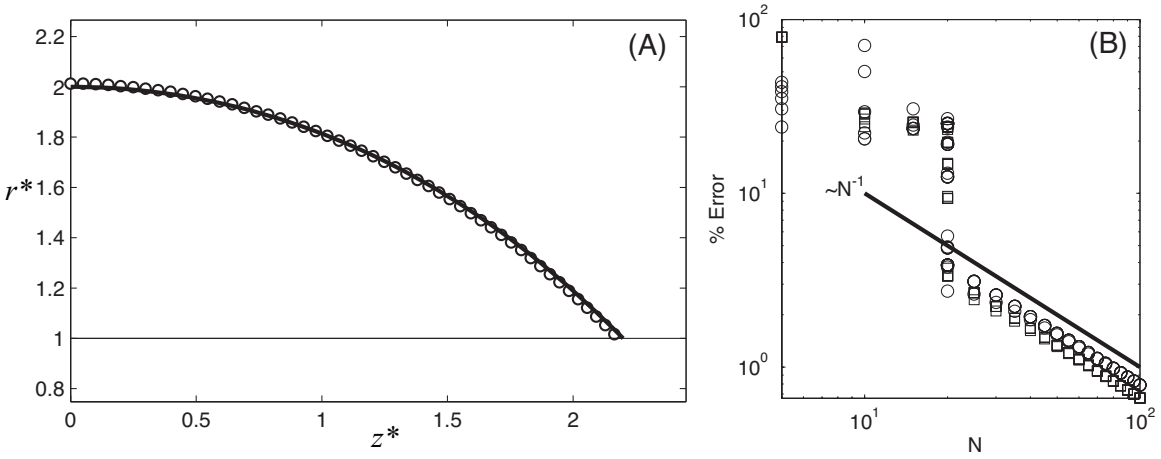

Fig. 8.1 (A) The shape of a drop wetting a cylindrical fiber as obtained with the unduloid method (solid line) and the energy minimization method (hollow circles, N=100, not all nodes are plotted). $\theta = 45^\circ$. (B) The relative discrepancy between the energy minimization and the unduloid predictions of the droplet apex (squares) and the axial position of the pinning point (circles) as a function of the number of nodes (N) used in the discretization of the drop surface; for large *N,* the error decreases as N^{-1}.

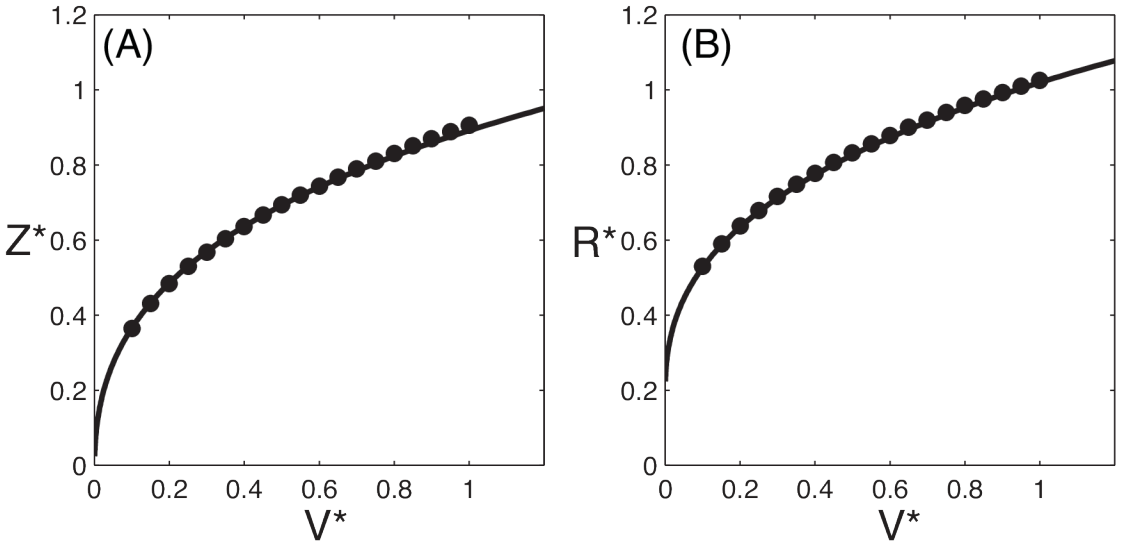

Fig. 8.2: The axial position of the pinning line (A) and the drop radius $r_2^* / \varepsilon = r_2 / a$ (B) as functions of the dimensionless volume V^*. The solid lines and the symbols denote, respectively, the unduloid solution and the energy minimization solution. ε=5 and $\theta = 90^\circ$.

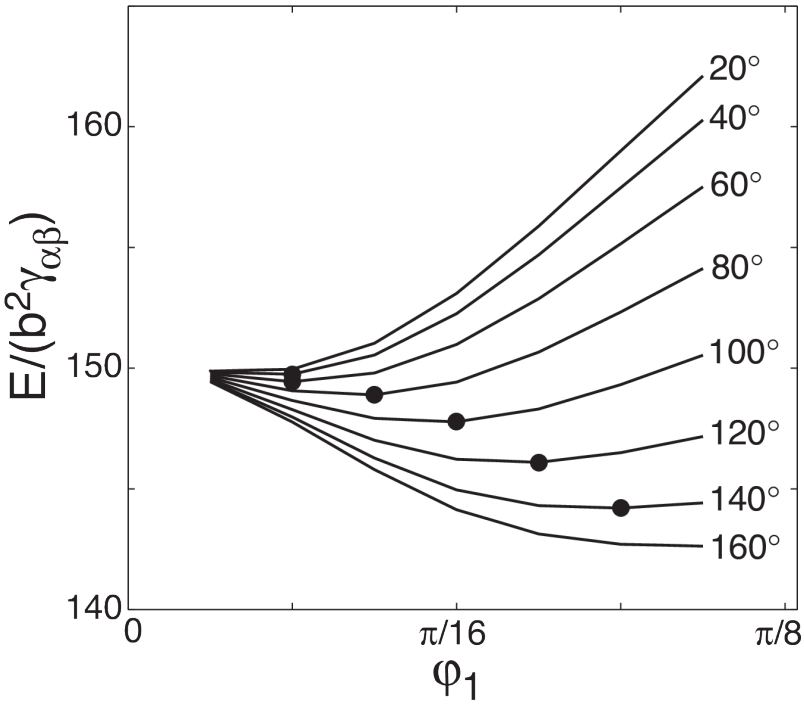

Fig. 8.3: The penalty function [8.1] as a function of the pinning line position ϕ_1 for various contact angles. e=3. The energy minima, when present, are denoted with solid circles.

8.2. Contact Angle Measurement

The three-phase contact angle was measured by an ex-situ experiment using a planar polystyrene film. A concentrated solution of polystyrene in toluene (20% w/v) was spin coated onto a glass slide with a commercial spin coater (Laurell Technologies Co., WS-400BZ-6NPP/Lite). The presence of PVA during the microfluidic generation of the polystyrene particles and the stretching of the particles into ellipsoids was simulated by spin coating 2% w/w PVA in water onto the PS film, followed by three subsequent spin coatings of water to rinse off any excess PVA. The composed film was heated to above the glass transition temperature (100^{o}C) of Polystyrene using a hot plate [46]. The film was rinsed with DI water and air dried before the contact angle measurement.

The three phase contact angle was measured with a goniometer (Theta Optical Tensiometer, Attension KSV instruments). The continuous phase consists of DI water and the dispersed phase of light mineral oil containing a 5% v/v surfactant ABIL EM 90 (Evonik Industries). The average contact angle obtained from four different samples prepared in a similar manner was $165.8 \pm 5.2^{\circ}$, which confirmed the hydrophilic character of the treated polystyrene. The contact angle of interest in our work is the supplementary angle $14.2 \pm 5.2^{\circ}$.

8.3. Dimensionless Groups

In the manuscript, we introduced several dimensionless groups to justify our assumptions. The various material properties used in these calculations are listed in Table 8.1. The relevant length and velocity scales are tabulated in Table 8.2 and the values for the dimensionless groups in Table 8.3. The smaller the magnitude of the dimensionless group , the more the interfacial tension forces dominate the system's behavior.

For the elastic modulus of *C.elegans,* we used the conservative value of 3.77 kPa [109]. Other sources indicate higher elastic moduli for nematodes such as 50 kPa [110] and 380 MPa [111] for the cuticle.

parameter	*value*
$\varrho_{\alpha,wtr}$	1.00e3 [kg/m^3]
$\varrho_{\beta,oil}$	8.3e2 [kg/m^3]
$\mu_{\alpha,wtr}$	1e-3 [Pa s]
$\mu_{\beta,oil}$	2.78e-2 [Pa s]
$\gamma_{\alpha\beta}$	1e-3 [N/m] [29], [49]
E_{CE}	3.77e-1[Pa] [109]
E_{PS}	3.6e9 [Pa] [112]

Table 8.1: The magnitudes of the various properties used in the calculation of Table 8.3.The light mineral oil's manufacturer provides the kinematic viscosity at 40^{o}C while the specific gravity is given at 15.6^{o}C. Subscripts *CE* and *PS,* respectively, denote properties of the *C.elegans* and polystyrene

parameter	*value*
$r_{2,D}$	5e-4 [m]
U	6e-3[m/s]
a_{CE}	4e-5 [m]
$2b_{CE}$	1.13e-3 [m]
a_{PS}	5e-5 [m]
$2b_{PS}$	7e-4 [m]

Table 8.2: Typical velocity and length scales. Subscripts D, CE, and PS denote properties belonging to a typical droplet, *C.elegans*, or polystyrene particle.

quantity	value
Bo	4.17e-1
Ca_{β}	1.67e-1
We_{α}	1.80e-2
Γ_{CE}	1.07e6
Γ_{PS}	2.21e-7

Table 8.3: Estimated magnitudes of the non-dimensional parameters relevant to our system

8.4. How Ellipsoidal are the Particles?

As a matter of convenience, in the manuscript, we assumed the particles have an ellipsoidal shape. To assess the accuracy of our assumption, we compare the profile of several particles to an analytical expression for ellipsoids. The profile is obtained by manually selecting $N\sim50$ points along the surface of an imaged particle in ImageJ. The major and minor axes for the analytical expression are acquired by circumscribing an ellipse around the particle in ImageJ and matching the narrowest and widest portions of the particle. We use polar coordinates to calculate the error metric:

$$\sqrt{\frac{1}{N}\sum_{i=1}^{N}\left(\frac{\rho_{\text{ellipse,i}}-\rho_{\text{exp.,i}}}{\varepsilon}\right)^2}, \qquad [8.16]$$

Five particles were measured; the maximum deviation between the ellipsoids and the actual particles was 3.8%.

References

[1] R. Seemann, M. Brinkmann, and T. Pfohl, “Droplet based microfluidics,” *Reports on progress …*, 2012.

[2] K. Choi, A. Ng, and R. Fobel, “Digital microfluidics,” *Annual Review of …*, 2012.

[3] T. Brugarolas, F. Tu, and D. Lee, “Directed assembly of particles using microfluidic droplets and bubbles,” *Soft Matter*, 2013.

[4] A. P. Kotula and S. L. Anna, “Probing timescales for colloidal particle adsorption using slug bubbles in rectangular microchannels,” *Soft Matter*, vol. 8, no. 41, p. 10759, 2012.

[5] L. Yao, N. Sharifi-Mood, I. B. Liu, and K. J. Stebe, “Capillary migration of microdisks on curved interfaces,” *Journal of Colloid and Interface Science*, Dec. 2014.

[6] D. Vella and L. Mahadevan, “The ‘cheerios effect’,” *American journal of physics*, 2005.

[7] C. W. Park and G. M. Homsy, “Two-phase displacement in Hele Shaw cells: theory,” *J. Fluid Mech.*, vol. 139, no. 1, pp. 291–308, Feb. 1984.

[8] F. P. Bretherton, “The motion of long bubbles in tubes,” pp. 1–23, Nov. 1960.

[9] P.-G. de Gennes, F. Brochard-Wyart, and D. Quere, *Capillarity and Wetting Phenomena*. Springer Science & Business Media, 2004.

[10] F. Brochard-Wyart and P. G. de Gennes, “Dynamics of partial wetting,” pp. 1–11, Oct. 2001.

[11] T. D. Blake, “The physics of moving wetting lines,” vol. 299, no. 1, pp. 1–13, Jul. 2006.

[12] T. D. Blake and J. M. Haynes, “Kinetics of liquidliquid displacement,” *Journal of Colloid and Interface Science*, vol. 30, no. 3, pp. 421–423, 1969.

[13] D. M. Kaz, R. McGorty, M. Mani, M. P. Brenner, and V. N. Manoharan, “Physical ageing of the contact line on colloidal particles at liquid interfaces,” *Nat Mater*, vol. 11, no. 2, pp. 138–142, Dec. 2011.

[14] P. G. Petrov, “Dynamics of deposition of Langmuir–Blodgett multilayers,” *Journal of the Chemical Society*, 1997.

[15] N. M. Schneider, M. M. Norton, and B. J. Mendel, “Electron–Water Interactions and Implications for Liquid Cell Electron Microscopy,” *The Journal of …*, 2014.

[16] B. Pastina and J. A. LaVerne, “Effect of molecular hydrogen on hydrogen peroxide in water radiolysis,” *The Journal of Physical Chemistry A*, 2001.

[17] J. M. Grogan, N. M. Schneider, F. M. Ross, and H. H. Bau, “The Nanoaquarium: A New Paradigm in Electron Microscopy
.”

[18] L. Rayleigh, “VIII. On the pressure developed in a liquid during the collapse of a spherical cavity,” *The London*, vol. 34, no. 200, pp. 94–98, 1917.
[19] M. S. Plesset, “The dynamics of cavitation bubbles,” *Journal of applied mechanics*, 1949.
[20] P. S. Epstein and M. S. Plesset, “On the Stability of Gas Bubbles in Liquid-Gas Solutions,” *J. Chem. Phys.*, vol. 18, no. 11, p. 1505, 1950.
[21] M. S. Plesset and A. Prosperetti, “Bubble Dynamics and Cavitation,” *Annu. Rev. Fluid Mech.*, vol. 9, no. 1, pp. 145–185, Jan. 1977.
[22] D. Lohse and X. Zhang, “Pinning and gas oversaturation imply stable single surface nanobubbles,” *Phys. Rev. E*, vol. 91, no. 3, p. 031003, Mar. 2015.
[23] A. K. Anal and H. Singh, “Recent advances in microencapsulation of probiotics for industrial applications and targeted delivery,” *Trends in Food Science & Technology*, vol. 18, no. 5, pp. 240–251, May 2007.
[24] T. Takei, K. Ikeda, H. Ijima, K. Kawakami, M. Yoshida, and Y. Hatate, “Preparation of polymeric microcapsules enclosing microbial cells by radical suspension polymerization via water-in-oil-in-water emulsion,” *Polym. Bull.*, vol. 65, no. 3, pp. 283–291, Jan. 2010.
[25] M. Chabert and J. L. Viovy, “Microfluidic high-throughput encapsulation and hydrodynamic self-sorting of single cells,” *PNAS*, vol. 105, no. 9, pp. 3191–3196, Mar. 2008.
[26] K. Khoshmanesh, J. Akagi, C. J. Hall, and K. E. Crosier, “New rationale for large metazoan embryo manipulations on chip-based devices,” ..., 2012.
[27] K. Chung, Y. Kim, J. S. Kanodia, E. Gong, and S. Y. Shvartsman, “A microfluidic array for large-scale ordering and orientation of embryos,” *Nature ...*, 2011.
[28] W. Shi, J. Qin, N. Ye, and B. Lin, “Droplet-based microfluidic system for individual Caenorhabditis elegans assay,” *Lab Chip*, 2008.
[29] A. S. Utada, A. Fernandez-Nieves, H. A. Stone, and D. A. Weitz, “Dripping to jetting transitions in coflowing liquid streams,” *Phys. Rev. Lett.*, 2007.
[30] X.-F. Wu, A. Bedarkar, and I. S. Akhatov, “Hydroelastic analysis of an axially loaded compliant fiber wetted with a droplet,” *J. Appl. Phys.*, vol. 108, no. 8, p. 083518, 2010.
[31] C. Delaunay, “Sur la surface de révolution dont la courbure moyenne est constante,” *Journal de Mathématiques Pures et Appliquées*, pp. 309–314.
[32] H. M. Princen, “Capillary phenomena in assemblies of parallel cylinders,” *Journal of Colloid and Interface Science*, vol. 30, no. 1, pp. 69–75, May 1969.
[33] R.-J. Roe, “Wetting of fine wires and fibers by a liquid film,” *Journal of Colloid and Interface Science*, vol. 50, no. 1, pp. 70–79, Jan. 1975.
[34] B. J. Carroll, “The accurate measurement of contact angle, phase contact areas, drop volume, and Laplace excess pressure in drop-on-fiber systems,” *Journal of Colloid and Interface Science*, vol. 57, no. 3, pp. 488–495, Dec. 1976.
[35] M. Brinkmann, J. Kierfeld, and R. Lipowsky, “A general stability criterion for droplets on structured substrates,” *J. Phys. A: Math. Gen.*, vol. 37, no. 48, pp. 11547–11573, Nov. 2004.

[36] H. B. Eral, J. de Ruiter, R. de Ruiter, J. M. Oh, and C. Semprebon, “Drops on functional fibers: from barrels to clamshells and back,” *Soft Matter*, 2011.
[37] W. C. Carter, “The forces and behavior of fluids constrained by solids,” *Acta Metallurgica*, vol. 36, no. 8, pp. 2283–2292, Aug. 1988.
[38] R. Finn, “Non uniqueness and uniqueness of capillary surfaces,” *Manuscripta Math*, vol. 61, no. 3, pp. 347–372, Sep. 1988.
[39] T. I. Vogel, “Stability of a liquid drop trapped between two parallel planes,” *SIAM J. Appl. Math.*, 1987.
[40] P. Kralchevsky and K. Nagayama, *Particles at Fluid Interfaces and Membranes*. Elsevier, 2001.
[41] R. Hanumanthu and K. J. Stebe, “Equilibrium shapes and locations of axisymmetric, liquid drops on conical, solid surfaces,” *Colloids and Surfaces A: Physicochemical and …*, 2006.
[42] S. Michielsen, J. Zhang, J. Du, and H. J. Lee, “Gibbs Free Energy of Liquid Drops on Conical Fibers,” *Langmuir*, vol. 27, no. 19, pp. 11867–11872, Oct. 2011.
[43] S. Wang and J. E. Mark, “Generation of glassy ellipsoidal particles within an elastomer by in situ polymerization, elongation at an elevated temperature, and finally cooling under strain,” *Macromolecules*, vol. 23, no. 19, pp. 4288–4291, Sep. 1990.
[44] C. C. Ho, R. H. Ottewill, A. Keller, and J. A. Odell, “Monodisperse ellipsoidal polystyrene latex particles: Preparation and characterisation,” *Polym. Int.*, vol. 30, no. 2, pp. 207–211, 1993.
[45] J. Loudet, A. Alsayed, J. Zhang, and A. Yodh, “Capillary Interactions Between Anisotropic Colloidal Particles,” *Phys. Rev. Lett.*, vol. 94, no. 1, p. 018301, Jan. 2005.
[46] J. Loudet, A. Yodh, and B. Pouligny, “Wetting and Contact Lines of Micrometer-Sized Ellipsoids,” *Phys. Rev. Lett.*, vol. 97, no. 1, p. 018304, Jul. 2006.
[47] Y. Han, A. M. Alsayed, M. Nobili, J. Zhang, T. C. Lubensky, and A. G. Yodh, “Brownian Motion of an Ellipsoid,” *Science*, vol. 314, no. 5799, pp. 626–630, Oct. 2006.
[48] Y. Han, A. Alsayed, M. Nobili, and A. Yodh, “Quasi-two-dimensional diffusion of single ellipsoids: Aspect ratio and confinement effects,” *Phys. Rev. E*, vol. 80, no. 1, p. 011403, Jul. 2009.
[49] A. S. Utada, É. Lorenceau, D. R. Link, and P. D. Kaplan, “Monodisperse double emulsions generated from a microcapillary device,” *Science*, 2005.
[50] J. C. Berg, *An Introduction to Interfaces & Colloids*. World Scientific, 2010.
[51] P. Attard, “Nanobubbles and the hydrophobic attraction,” *Advances in Colloid and Interface Science*, vol. 104, no. 1, pp. 75–91, Jul. 2003.
[52] P. Attard, M. P. Moody, and J. Tyrrell, “Nanobubbles: the big picture,” *PHYSICA A-STATISTICAL MECHANICS AND ITS APPLICATIONS*, vol. 314, no. 1, pp. {696–705}, {NOV 1} 2002.
[53] M. P. Brenner and D. Lohse, “Dynamic equilibrium mechanism for surface nanobubble stabilization,” *Phys. Rev. Lett.*, 2008.
[54] J. C. Eriksson and S. Ljunggren, “On the mechanically unstable free energy

minimum of a gas bubble which is submerged in water and adheres to a hydrophobic wall," *Colloids and Surfaces A: Physicochemical and …*, 1999.

[55] S. T. Lou, Z. Q. Ouyang, Y. Zhang, X. J. Li, and J. Hu, "Nanobubbles on solid surface imaged by atomic force microscopy," *Journal of Vacuum …*, 2000.

[56] A. Poynor, L. Hong, I. K. Robinson, S. Granick, and Z. Zhang, "How water meets a hydrophobic surface," *Physical review …*, 2006.

[57] J. Tyrrell and P. Attard, "Atomic force microscope images of nanobubbles on a hydrophobic surface and corresponding force-separation data," *Langmuir*, 2002.

[58] J. Tyrrell and P. Attard, "Images of nanobubbles on hydrophobic surfaces and their interactions," *Phys. Rev. Lett.*, 2001.

[59] L. Zhang, Y. Zhang, X. Zhang, Z. Li, G. Shen, M. Ye, and C. Fan, "Electrochemically controlled formation and growth of hydrogen nanobubbles," *Langmuir*, 2006.

[60] X. H. Zhang, N. Maeda, and V. Craig, "Physical properties of nanobubbles on hydrophobic surfaces in water and aqueous solutions," *Langmuir*, 2006.

[61] X. H. Zhang, G. Li, N. Maeda, and J. Hu, "Removal of induced nanobubbles from water/graphite interfaces by partial degassing," *Langmuir*, 2006.

[62] S. Yang, S. M. Dammer, N. Bremond, and H. Zandvliet, "Characterization of nanobubbles on hydrophobic surfaces in water," *Langmuir*, 2007.

[63] J. Yang, J. Duan, and D. Fornasiero, "Very small bubble formation at the solid-water interface," *The Journal of Physical …*, 2003.

[64] M. Mao, J. Zhang, R. H. Yoon, and W. A. Ducker, "Is there a thin film of air at the interface between water and smooth hydrophobic solids?," *Langmuir*, 2004.

[65] J. L. PARKER, P. M. CLAESSON, and P. Attard, "Bubbles, cavities, and the long-ranged attraction between hydrophobic surfaces.," *The Journal of Physical …*, 1994.

[66] G. Liu, Z. Wu, and V. S. J. Craig, "Cleaning of Protein-Coated Surfaces Using Nanobubbles: An Investigation Using a Quartz Crystal Microbalance," *J. Phys. Chem. C*, vol. 112, no. 43, pp. 16748–16753, Oct. 2008.

[67] G. Liu and V. S. J. Craig, "Improved Cleaning of Hydrophilic Protein-Coated Surfaces using the Combination of Nanobubbles and SDS," *ACS Appl. Mater. Interfaces*, vol. 1, no. 2, pp. 481–487, Feb. 2009.

[68] R. Cavicchi and C. Avedisian, "Bubble Nucleation and Growth Anomaly for a Hydrophilic Microheater Attributed to Metastable Nanobubbles," *Phys. Rev. Lett.*, vol. 98, no. 12, p. 124501, Mar. 2007.

[69] W. A. Ducker, "Contact Angle and Stability of Interfacial Nanobubbles," *Langmuir*, vol. 25, no. 16, pp. 8907–8910, Aug. 2009.

[70] J. M. Grogan, "The Nanoaquarium: A Nanofluidic Platform for In Situ Transmission Electron Microscopy in Liquid Media."

[71] J. M. Grogan, L. Rotkina, and H. H. Bau, "In situ liquid-cell electron microscopy of colloid aggregation and growth dynamics," *Phys. Rev. E*, vol. 83, no. 6, p. 061405, Jun. 2011.

[72] J. M. Grogan, N. M. Schneider, F. M. Ross, and H. H. Bau, “Bubble and Pattern Formation in Liquid Induced by an Electron Beam,” *Nano Lett.*, vol. 14, no. 1, pp. 359–364, Jan. 2014.
[73] N. M. Schneider, J. H. Park, J. M. Grogan, S. Kodambaka, D. A. Steingart, F. M. Ross, and H. H. Bau, “In-Situ Electron Microscopy of Electrochemical Deposition, Dendrite Growth, and Etching,” *J. Heat Transfer*, vol. 136, no. 8, p. 080910, Aug. 2014.
[74] M. Bresin, A. Chamberlain, E. U. Donev, C. B. Samantaray, G. S. Schardien, and J. T. Hastings, “Electron-Beam-Induced Deposition of Bimetallic Nanostructures from Bulk Liquids,” *Angew. Chem. Int. Ed.*, vol. 52, no. 31, pp. 8004–8007, Jun. 2013.
[75] T.-W. Huang, S.-Y. Liu, Y.-J. Chuang, H.-Y. Hsieh, C.-Y. Tsai, W.-J. Wu, C.-T. Tsai, U. Mirsaidov, P. Matsudaira, C.-S. Chang, F.-G. Tseng, and F.-R. Chen, “Dynamics of hydrogen nanobubbles in KLH protein solution studied with in situ wet-TEM,” *Soft Matter*, vol. 9, no. 37, p. 8856, 2013.
[76] D. Bhattacharya, M. Bosman, V. R. S. S. Mokkapati, F. Y. Leong, and U. Mirsaidov, “Nucleation Dynamics of Water Nanodroplets,” *Microsc Microanal*, vol. 20, no. 2, pp. 407–415, Mar. 2014.
[77] H. Zheng and U. M. Mirsaidov, “Direct observation of stick-slip movements of water nanodroplets induced by an electron beam,” presented at the Proceedings of the …, 2012.
[78] F. Y. Leong, U. M. Mirsaidov, P. Matsudaira, and L. Mahadevan, “Dynamics of a nanodroplet under a transmission electron microscope,” vol. 26, no. 1, p. 012003, Jan. 2014.
[79] D. Maier-Schneider, “A New Analytical Solution for the Load-Deflection of Square Membranes,” pp. 1–4, Mar. 2004.
[80] J. C. Crocker and E. R. Weeks, “Particle tracking using IDL.”
[81] D. Blair and E. Dufresne, “Matlab Particle Tracking.”
[82] D. W. Langbein, *Capillary Surfaces*. Springer Science & Business Media, 2002.
[83] R. Dangla, S. C. Kayi, and C. N. Baroud, “Droplet microfluidics driven by gradients of confinement,” *PNAS*, vol. 110, no. 3, pp. 853–858, Jan. 2013.
[84] G. TAYLOR and P. G. Saffman, “A NOTE ON THE MOTION OF BUBBLES IN A HELE-SHAW CELL AND POROUS MEDIUM,” *Q J Mechanics Appl Math*, vol. 12, no. 3, pp. 265–279, 1959.
[85] S. Tanveer and P. G. Saffman, “Stability of bubbles in a Hele–Shaw cell,” *Phys. Fluids*, vol. 30, no. 9, pp. 2624–2635, Sep. 1987.
[86] R. W. Style and E. R. Dufresne, “Static wetting on deformable substrates, from liquids to soft solids,” *Soft Matter*, 2012.
[87] M. K. Chaudhury and G. M. Whitesides, “How to Make Water Run Uphill,” *Science*, vol. 256, no. 5063, pp. 1539–1541, Jun. 1992.
[88] A. A. Darhuber and S. M. Troian, “PRINCIPLES OF MICROFLUIDIC ACTUATION BY MODULATION OF SURFACE STRESSES,” *Annu. Rev. Fluid Mech.*, vol. 37, no. 1, pp. 425–455, Jan. 2005.
[89] P. Renvoisé, J. W. M. Bush, M. Prakash, and D. Quéré, “Drop propulsion in tapered tubes,” *EPL*, vol. 86, no. 6, p. 64003, Jun. 2009.

[90] H. Bouasse, *Capillarite: phenomenes superficiels; Librairie Delgrave: Paris, 1924*.
[91] É. Lorenceau and D. Quéré, "Drops on a conical wire," *J. Fluid Mech.*, 2004.
[92] T. Metz, N. Paust, R. Zengerle, and P. Koltay, "Capillary driven movement of gas bubbles in tapered structures," *Microfluid Nanofluid*, vol. 9, no. 2, pp. 341–355, Dec. 2009.
[93] E. Reyssat, "Drops and bubbles in wedges," *J. Fluid Mech.*, vol. 748, pp. 641–662, May 2014.
[94] R. M. Jenson, A. P. Wollman, M. M. Weislogel, L. Sharp, R. Green, P. J. Canfield, J. Klatte, and M. E. Dreyer, "Passive phase separation of microgravity bubbly flows using conduit geometry," *International Journal of Multiphase Flow*, vol. 65, pp. 68–81, Oct. 2014.
[95] I. Cantat, "Liquid meniscus friction on a wet plate: Bubbles, lamellae, and foamsa)," *Physics of Fluids (1994-present)*, vol. 25, no. 3, p. 031303, 2013.
[96] P. Concus and R. Finn, "Discontinuous behavior of liquids between parallel and tilted plates," *Phys. Fluids*, vol. 10, no. 1, p. 39, 1998.
[97] J. Eggers and H. A. Stone, "Characteristic lengths at moving contact lines for a perfectly wetting fluid: the influence of speed on the dynamic contact angle ," pp. 1–13, Feb. 2008.
[98] J. H. Snoeijer and B. Andreotti, "Moving Contact Lines: Scales, Regimes, and Dynamical Transitions," *Annu. Rev. Fluid Mech.*, vol. 45, no. 1, pp. 269–292, Jan. 2013.
[99] D. M. Kaz, R. McGorty, M. Mani, and M. P. Brenner, "Physical ageing of the contact line on colloidal particles at liquid interfaces," *Nat Mater*, 2012.
[100] C. Huh and L. E. Scriven, "Hydrodynamic Model of Steady Movement of a Contact Line," pp. 1–17, Jun. 2014.
[101] A. Eri and K. Okumura, "Viscous drag friction acting on a fluid drop confined in between two plates," vol. 7, no. 12, p. 5648, 2011.
[102] B. Arkles, *Hydrophobicity, hydrophilicity and silanes*. Paint & Coatings Industry magazine, 2006.
[103] R. Sander, "Compilation of Henry's law constants (version 4.0) for water as solvent," *Atmos. Chem. Phys.*, vol. 15, no. 8, pp. 4399–4981, 2015.
[104] E. L. Cussler, *Diffusion: mass transfer in fluid systems*. 2009.
[105] J. Li, H. Chen, W. Zhou, B. Wu, S. D. Stoyanov, and E. G. Pelan, "Growth of Bubbles on a Solid Surface in Response to a Pressure Reduction," *Langmuir*, vol. 30, no. 15, pp. 4223–4228, Apr. 2014.
[106] E. W. Weisstein, "Spherical Cap," *MathWorld--A Wolfram Web Resource*. [Online]. Available: http://mathworld.wolfram.com/SphericalCap.html. [Accessed: 18-Jul-2015].
[107] J. M. Grogan, N. M. Schneider, F. M. Ross, and H. H. Bau, "Bubble and Pattern Formation in Liquid Induced by an Electron Beam," *Nano Lett.*, vol. 14, no. 1, pp. 359–364, Jan. 2014.
[108] R. Verma, A. Sharma, K. Kargupta, and J. Bhaumik, "Electric Field Induced Instability and Pattern Formation in Thin Liquid Films," *Langmuir*, vol. 21, no. 8, pp. 3710–3721, Apr. 2005.
[109] J. Sznitman, P. K. Purohit, P. Krajacic, T. Lamitina, and P. E. Arratia,

"Material Properties of Caenorhabditis elegans Swimming at Low Reynolds Number," *Biophysical Journal*, vol. 98, no. 4, pp. 617–626, Feb. 2010.

[110] Sung-Jin Park, M. B. Goodman, and B. L. Pruitt, "Measurement of Mechanical Properties of Caenorhabditis elegans with a Piezoresistive Microcantilever System," presented at the 2005 3rd IEEE/EMBS Special Topic Conference on Microtechnology in Medicine and Biology, pp. 400–403.

[111] S. J. Park, M. B. Goodman, and B. L. Pruitt, "Analysis of nematode mechanics by piezoresistive displacement clamp," *PNAS*, vol. 104, no. 44, pp. 17376–17381, Oct. 2007.

[112] C. M. Stafford, B. D. Vogt, C. Harrison, D. Julthongpiput, and R. Huang, "Elastic Moduli of Ultrathin Amorphous Polymer Films," *Macromolecules*, vol. 39, no. 15, pp. 5095–5099, Jul. 2006.